

REPORT DOCUMENTATION PAGE

Form Approved
OMB No. 0704-0188

Public reporting burden for this collection of information is estimated to average 1 hour per response, including the time for reviewing instructions, searching data sources, gathering and maintaining the data needed, and completing and reviewing the collection of information. Send comments regarding this burden estimate or any other aspect of this collection of information, including suggestions for reducing this burden to Washington Headquarters Service, Directorate for Information Operations and Reports, 1215 Jefferson Davis Highway, Suite 1204, Arlington, VA 22202-4302, and to the Office of Management and Budget, Paperwork Reduction Project (0704-0188) Washington, DC 20503.

PLEASE DO NOT RETURN YOUR FORM TO THE ABOVE ADDRESS.

1. REPORT DATE (DD-MM-YYYY) 07/27/99		2. REPORT DATE 07/27/99		3. DATES COVERED (From - To) 10/1/95 - 3/31/99	
4. TITLE AND SUBTITLE Nonlinear Dynamics of Coupled Laser Systems				5a. CONTRACT NUMBER N00014-96-1-0045	
				5b. GRANT NUMBER	
				5c. PROGRAM ELEMENT NUMBER	
6. AUTHOR(S) Rajarshi Roy				5d. PROJECT NUMBER	
				5e. TASK NUMBER	
				5f. WORK UNIT NUMBER	
7. PERFORMING ORGANIZATION NAME(S) AND ADDRESS(ES) Georgia Tech Research Corporation Centennial Research Building 400 Tenth Street NW Atlanta, GA 30332-0420				8. PERFORMING ORGANIZATION REPORT NUMBER	
9. SPONSORING/MONITORING AGENCY NAME(S) AND ADDRESS(ES) Office of Naval Research Michael F. Shlesinger ONR 331 800 N. Quincy Street Arlington, VA 22217-5660				10. SPONSOR/MONITOR'S ACRONYM(S) ONR	
				11. SPONSORING/MONITORING AGENCY REPORT NUMBER	
12. DISTRIBUTION AVAILABILITY STATEMENT DISTRIBUTION STATEMENT A Approved for Public Release Distribution Unlimited					
13. SUPPLEMENTARY NOTES					
14. ABSTRACT					
15. SUBJECT TERMS					
16. SECURITY CLASSIFICATION OF:			17. LIMITATION OF ABSTRACT	18. NUMBER OF PAGES	19a. NAME OF RESPONSIBLE PERSON
a. REPORT	b. ABSTRACT	c. THIS PAGE			19b. TELEPHONE NUMBER (Include area code)

NONLINEAR DYNAMICS OF COUPLED LASER SYSTEMS

ONR GRANT N00014-96-1-0045

Final Technical Report

by

Rajarshi Roy

School of Physics

Georgia Institute of Technology

Atlanta, GA 30332

July, 1999

DTIC QUALITY INSPECTED 2

19990804 186

This final technical report summarizes the results of research supported by the Office of Naval Research from October 1, 1995 to March 31, 1999, at the School of Physics, Georgia Institute of Technology.

The research has encompassed a broader range of topics than was originally in the original proposal. The topics investigated were as follows.

(a) Dynamics of coupled laser systems and arrays. The research focussed on experiments and numerical modeling to explore the dynamics of synchronization of two and more coupled lasers. A new amplitude instability of coupled lasers was predicted and then experimentally verified (Phys. Rev. E55, 3865 (1997)). This result is of significance to the design and fabrication of coupled laser arrays and describes the fundamental instabilities of amplitude and phase that may occur when lasers are coupled together through sharing of light between their cavities by evanescent leakage between waveguides. We showed that there can be phase coherence even in regimes of amplitude instability and chaos, a result that has been further investigated theoretical by Kurths and his group at Potsdam.

We also investigated the nature of synchronization and intermittency of the oscillations of coupled lasers in a collaboration with Peter Ashwin and his student John Terry, of the mathematics department of the University of Surrey (Phys. Rev. E 58, 7186 (1998)). This investigation of blowout bifurcations in the dynamics of coupled lasers was extended to studies of synchronization of a linear array of three coupled lasers (Phys. Rev. E 59, 4036 (1999)). This paper contained a first demonstration of generalized synchronization in this linear three laser system, where the two outer lasers were identically synchronized, but the middle laser was synchronized to the outer ones through a nonlinear functional relation. This paper also contains the first demonstration of subharmonic generalized

synchronization, where the oscillations of the central laser can occur at twice the average frequency of the outer ones.

(b) Wave propagation in nonlinear media and four wave mixing in optical fibers. A unique set of experiments was carried out to explore four wave mixing and its dynamical evolution in single mode optical fibers. These experiments revealed the importance and influence of spectral structure and phase fluctuations in the propagation of light at multiple frequencies through optical fiber. The results of these experiments were presented in a comprehensive paper (Phys. Rev. E57, 4757 (1998)). It was found that multiple wave interactions are significantly influenced by fine spectral structure of the lasers as well as by phase fluctuations of the light, and that these effects must be included in a model in order to make accurate predictions of the dynamical evolution of the waves along the length of fiber. The experiments consisted of hundreds of measurements at over fifty different lengths of fiber in order to obtain measurements of the spectral evolution of the waves. A specially built CCD camera developed for astronomical observations was used for these measurement, that provided a 14 bit dynamic range for detection of the sidebands generated by four wave mixing. The numerical investigations included integration of the nonlinear Schroedinger equation and of coupled mode equations with stochastic noise sources to simulate the phase fluctuations of the lasers.

(c) Transmission of polarized light through a single mode fiber with random fluctuations of birefringence. In the course of our work on propagation of light through fibers we discovered that it is possible to convey linearly polarized light through single mode optical fibers that possess random birefringence fluctuations along their length. The mathematical prediction of this possibility and its experimental demonstration were carried out (Applied Optics 38, 3888 (1999)), and are a very practical application of an earlier theory developed by us to describe the dynamics of a laser with nonlinear, birefringent

elements in its cavity. These results were quite surprising to many members of the nonlinear optics community.

(d) Nonlinear dynamics of erbium doped fiber lasers and application to synchronization and communication. A large part of our time was involved in the measurements of the fast dynamics of erbium doped fiber ring lasers (EDFRLs). These lasers had previously been examined by many different groups, but their focus had been on slow millisecond dynamics that originated in q-switching behavior due to the long decay time of the upper lasing level of erbium for the 1.55 micron transition. We showed that there was chaotic dynamics at the nanosecond and faster time scales that could be observed and that new models were required to describe these effects (Phys. Rev. A55, 2376 (1997)). The inclusion of stochastic effects was an important part of our model, and the equations involved were delay-differential equations of a type developed earlier by Ikeda to describe optical bistability. These equations provide a very good qualitative and often quantitative description of the waveforms measured for different values of parameters of operation of the laser system. The development of the Ikeda model to include stochastic noise was carried out by us (Phys. Lett. A224, 51 (1996) and Phys. Lett. A229, 362 (1997)). The influence of noise as a precursor to bifurcations in laser systems described by these equations, predicted by us in these papers, has been observed Mozdy and Pollock at Cornell on sodium chloride lasers (Phys. Lett. A249, 218 (1998)).

The application of EDFRLs to chaotic communication has been developed in a sequence of experiments, including the first demonstration of optical chaotic communication (Science 279, 1198 (1998)). The development of more sophisticated schemes has been given in later papers (Phys. Rev. Lett. 81, 3547 (1998)) and in a paper accepted for publication (Int. J. Bif. and Chaos, 1999) that is attached with this report. These papers report optical communication with chaotic waveforms at hundreds of Mbits/sec, demonstrate the possibility of multiplexing of channels at different wavelengths, and show

that messages can be transmitted over tens of kilometers of fiber. The role of polarization variations in the light due to the fiber channel, and the design of a receiver to recover the information suitable for different configurations of the transmitter system are all examined in detail. Addition of a digital message to chaotic light, as well as direct modulation of the chaotic light, are shown to be effective in these communication schemes. The influence of parameter mismatches between transmitter and receiver is investigated, and it is shown that mismatches from a few percent to as much as fifty percent are possible for different parameters, in order to receive and decode the message carried by chaotic waveforms.

Our most recent studies have been concerned with the use of polarization dynamics of EDFRLs for communication of information. As a first step, we developed a technique for the measurement of fast polarization fluctuations in these lasers. Conventional polarization analyzers operate at millisecond time scales or slower. We developed a high speed fiber optic polarization analyzer that can measure polarization dynamics on nanosecond time scales (Opt. Comm. 164, 107 (1999)). The polarization dynamics of a chaotic erbium laser is displayed on a Poincare sphere. We discovered that there are several modes of polarization switching that occur in EDFRLs, between both orthogonal and non-orthogonal polarization states. It is now possible to measure the changes in degree of polarization of the light as well as the time variation of the Stokes parameters.

The final set of measurements that are now being written up for submission involve experiments that utilize the polarization of light for communication of information. Previous methods that use polarization for communication use designated polarization states to correspond to given symbols. We have used a dynamical encoding method in which it is the *changes* in polarization state that are relevant, and that carry the information. We have demonstrated such communication at a hundred Mbits.

The research described here has initiated work on similar themes by researchers in U.K., Spain, Germany, Australia and Japan. Different schemes and variations of our methods are being developed by these researchers, and preliminary experiments of Gbit/sec communication with chaotic waveforms have been submitted. We have many ideas that we hope to investigate in the near future that concern the transmission and storage of images as spatio-temporal chaotic waveforms, as well as the possibility of data compression through optical implementations of iterated function systems. We believe that nonlinear dynamics has much to contribute to practical applications in information processing and communications, and regard the results reported here a first stage in the development and demonstration of fundamental scientific concepts.

Synchronization of chaos in an array of three lasers

John R. Terry,* K. Scott Thornburg, Jr., David J. DeShazer, Gregory D. VanWiggeren, Shiqun Zhu,[†] Peter Ashwin,* and Rajarshi Roy

School of Physics, Georgia Institute of Technology, Atlanta, Georgia 30332-0430

(Received 21 October 1998)

Synchronization of the chaotic intensity fluctuations of three modulated Nd:YAG lasers oriented in a linear array with either a modulated pump or loss is investigated experimentally, numerically, and analytically. Experimentally, synchronization is only seen between the two outer lasers, with little synchrony between outer and inner lasers. Using a false nearest-neighbors method, we numerically estimate the experimental system dynamics to be five dimensional, which is in good agreement with analytical results. Numerically, synchronization is only seen between the two outer lasers, which matches the experimental data well. Lack of synchrony between outer and inner lasers, is explained analytically and then we numerically investigate loss of synchronization of the outer two lasers, observing the occurrence of a blowout bifurcation. Finally, the effects of noise and symmetry breaking are examined and discussed. [S1063-651X(99)03604-1]

PACS number(s): 05.45.xt, 42.50.Lc, 42.65.Sf, 42.55.Ah

I. INTRODUCTION

Experimental and theoretical investigations of chaotic synchronization in coupled nonlinear systems have attracted much attention in recent years due to the possibility of practical applications of this fundamental phenomenon. Several papers have studied the synchronization of chaotic signals in the context of electronic circuits [1–3], secure communication [4–6], turbulence in fluids [7,8], chemical and biological systems [9], and laser dynamics [10–14]. Winful and Rahman have numerically investigated the possibility of synchronization of chaos in semiconductor laser arrays on a nanosecond time scale [10] and previously, we have also performed experimental measurements and demonstrated synchronization of two chaotic lasers [15]. To our knowledge, however, the experimental synchronization of chaos in laser arrays with more than two lasers has yet to be reported.

In this paper, the synchronization, both experimentally and numerically, of three coupled, chaotic, Nd:YAG (trivalent neodymium doped yttrium aluminum garnet) lasers in the separate cases of pump and loss modulation is reported. In a linear array of three lasers, a high degree of synchronization between the two outer lasers is seen, while little if any synchronization is observed between the outer and inner lasers. The experimental observations are in good agreement with analytical results, which clearly explain the lack of synchronization between outer and inner laser. Similar results were seen by Winful and Rahman [10] in a numerical model for three semiconductor lasers coupled in a linear array.

The numerical simulations show similar behavior in this coupled linear array of three lasers to that seen in a system of two coupled lasers [14] and we present numerical evidence to suggest that synchronization between the two outer lasers may be lost through a *blowout* bifurcation, where an attractor

contained within the synchronized submanifold loses its transverse stability [16]. This indicates that as in the two laser case, forced symmetry breaking is not necessary for desynchronization of the two outer lasers to occur.

The rest of this paper is arranged as follows. In Sec. II we describe the experimental setup for a system of three Nd:YAG lasers coupled in a linear array and explain the techniques that we used in obtaining the experimental data. Section III describes the equations we used to model the laser system and investigates the occurrence of synchronization between the two outer lasers and also the lack of synchronization between the outer and inner laser. In Sec. IV, we describe how the numerical simulations were performed in the case of loss modulation and finally, in Sec. V, we discuss our findings and consider the implications for coupling large systems of lasers in a linear array.

II. EXPERIMENTAL SETUP

To study the dynamics of a pump or loss modulated three laser array we use the experimental system as shown in Fig. 1. This setup consists of three equal intensity, parallel and laterally separated beams created by pumping a Nd:YAG rod, 5 mm in both length and diameter in a plane parallel cavity. Three Ar⁺ pump beams ($\lambda = 514.5$ nm) are formed by passing a single beam through a fan-out grating designed to produce equal intensities for the zeroth- and first-order beams, and negligible intensities elsewhere. The separation and relative orientation of the three beams of interest are controlled using a simple telescope. The pump beams, in the end, are parallel and symmetric with respect to the axis of the YAG crystal. The optical cavity consists of one high reflection coated end face of the rod and of an external planar output coupler with 2% transmittance. The pump power for the pump modulation case is approximately 5.8 W, and 5.0 W for the loss modulation case. For these parameters, the relaxation oscillation frequency, ν_R , is of the order of 100 kHz. A thick etalon ensures single longitudinal mode operation. This etalon doubles as an intracavity acousto-optical modulator (AOM) for the loss modulation case. Pump modu-

*Present address: Department of Mathematics and Statistics, University of Surrey, Guildford GU2 5XH, U.K.

[†]Present address: School of Physics and Technology, Suzhou University, Suzhou, Jiangsu 215006, P.R.O.C.

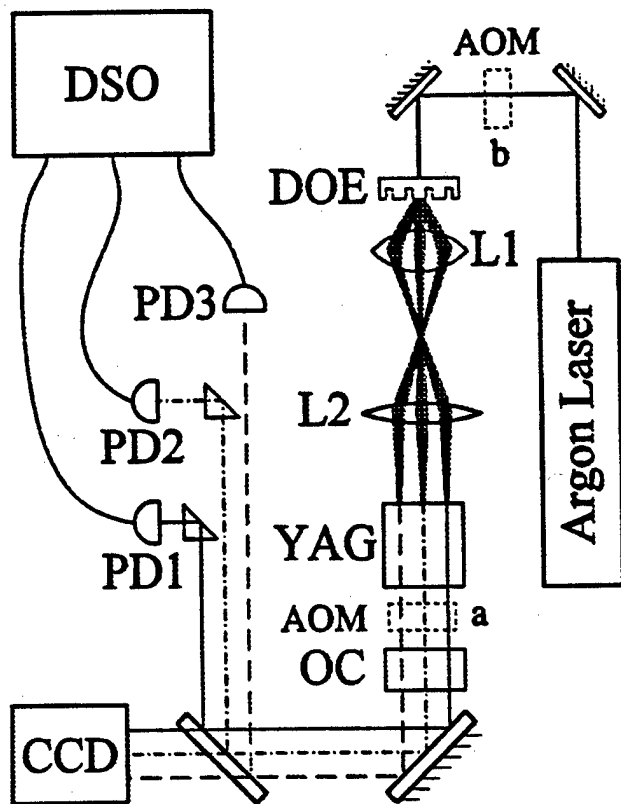


FIG. 1. Experimental system for generating three laterally coupled lasers in a Nd:YAG crystal and observing the synchronization of chaotic laser intensities. A diffractive optic is used to split the argon laser into three beams with almost equal intensities. The three beams are made parallel by a telescope; changing the magnification of the telescope changes the separation d between each laser. An Acousto-Optic Modulator (AOM) is placed in position (a) in the case of loss modulation and in position (b), in the case of pump modulation. The Nd:YAG crystal is coated for high reflectivity (HR) on one side and antireflection coated (AR) on the other. The output coupler (OC) is 2% transmissive; both mirrors are flat. A charge-coupled device camera is used to measure the far-field intensity pattern of the array, while the three photodiodes PD1, PD2, and PD3 simultaneously measure each laser's intensity dynamics, which are subsequently recorded on a digital sampling oscilloscope (DSO).

lation is attained using an AOM positioned before the fan-out grating.

Thermal lensing in the YAG rod, generated by Ar^+ pump beams with waist radii $\sim 20 \mu\text{m}$ allows the formation of three separate and stable cavities [11]. The TEM_{00} infrared laser beams generated in the YAG crystal have radii $\sim 200 \mu\text{m}$. Radii are measured at $1/e^2$ of the maximum intensity of the Gaussian profile. The coupling between the beams is determined by their nearest-neighbor separation, which can be shifted by adjusting the grating and the telescope lenses' positions. The pump beam separations and profiles are measured directly using a rotating slit method. The minimum value for nearest-neighbor separation used was 0.64 mm, for which there is no appreciable overlap of the pump beams and coupling is entirely due to the spatial overlap of the infrared laser fields. The couplings and detunings were chosen such that, in the absence of modulation, the lasers exhibit an instability caused by the resonance of the

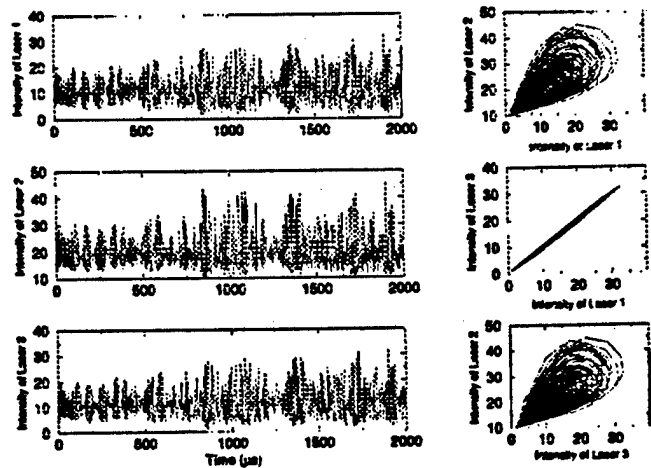


FIG. 2. Experimental measurements of the relative intensities of three coupled lasers for pump beam separations $d = 0.975 \text{ mm}$ and modulation depth $p_{1i} = 0.20$ (for $i = 1, 2, 3$). A high degree of intensity synchronization is seen only between lasers 1 and 3.

phase dynamics with the relaxation oscillations as described, for example, in [13].

The three infrared beams produced by the Nd:YAG laser are separated using a sequence of non-polarizing cube beam splitters and prisms. The intensity dynamics of the individual lasers are recorded simultaneously using fast photodiodes and a four-channel digital oscilloscope. A scanning Fabry-Pérot interferometer is utilized to ensure that the individual lasers have only a single longitudinal mode.

Experimental measurements for the pump modulated case are displayed in Fig. 2 for nearest-neighbor separations of approximately 0.975 mm. Chaotic synchronization between the two outer lasers is clearly seen, whereas there is no apparent synchronization between outer and inner lasers. In the case of loss modulation they are displayed in Fig. 3 for nearest-neighbor separations of approximately 0.64 mm. Despite additional noise present in the loss modulated experimental setup, chaotic synchronization between lasers 1 and 3 is readily apparent. Again, pairing intensities of lasers 1 and

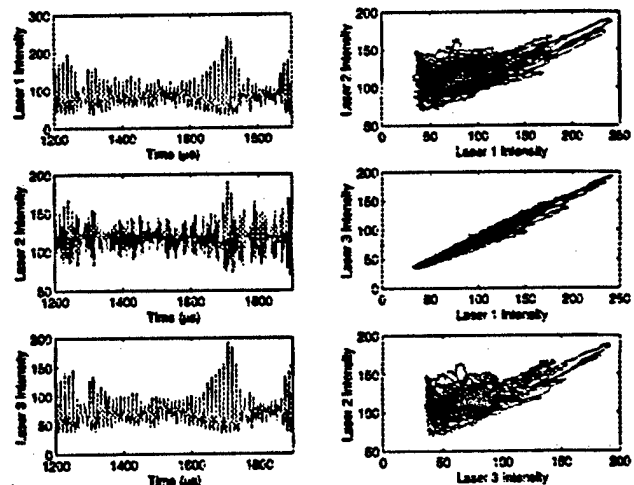


FIG. 3. Experimental measurements of the relative intensities of three coupled lasers with loss modulation. Here the nearest neighbor separation $d = 0.64 \text{ mm}$. Once again, a high degree of intensity synchronization is seen only between lasers 1 and 3.

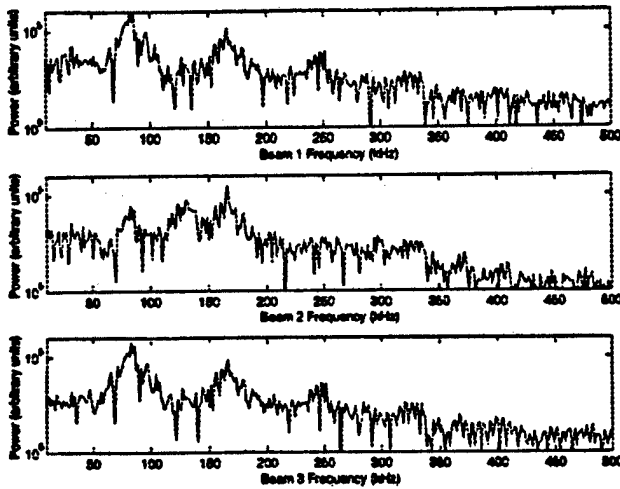


FIG. 4. Power spectrum of three linearly coupled lasers, in the case of loss modulation at a rate of 166 kHz. Here the nearest neighbor separations are again 0.64 mm. Notice the peak in the central beam close to 150 kHz, which is not present in the two outer beams. However, the side beams display a peak at approximately 80 kHz of a greater intensity than the corresponding peak in the central beam. The peak in all beams at 166 kHz corresponds to modulation at this rate.

2, as well as lasers 3 and 2, show little synchrony.

It is interesting to note the harmonic relationships between the side lasers, 1 and 3, and the center beam, laser 2. The intensity of laser 2 oscillates at a rate approaching twice the frequency of the side beam oscillations. Figure 4 compares the power spectrums of the individual beams. The dominant peak of the central beam approaches 150 kHz while the side beams display peaks at approximately 80 kHz. The sharp spike at 166 kHz is due to modulation at this frequency.

The intensity time series dynamics of all three lasers was numerically estimated to be five dimensional (Fig. 5), using a false nearest-neighbors method [17], with 25 000 time units considered. This result agrees with the dynamically invariant state labeled amplitude antisynchronized in Table I, corresponding to a system with amplitude synchronization and equal left and right detunings present.

III. EQUATIONS OF MOTION

The equations describing the time evolution of the slowly varying, complex electric field amplitude E_i and real gain G_i of laser i in an array of three spatially coupled, pump modulated single-mode Class B lasers are similar to those of the

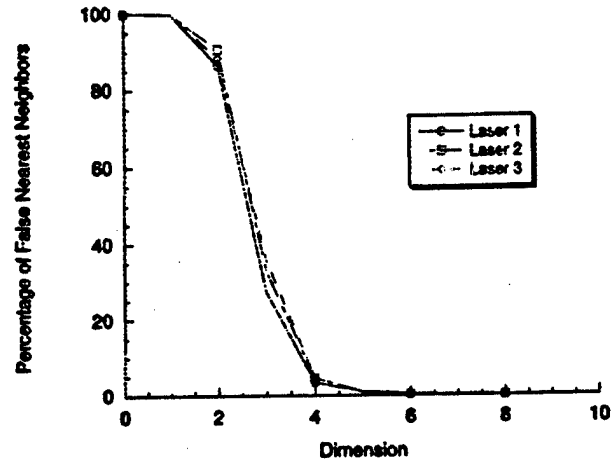


FIG. 5. Using the false nearest-neighbors method, we numerically estimate the dimensionality of the experimental system, using measured time series of the intensity fluctuations. The 1% mark suggests that the system is five dimensional, giving good agreement between the experiments and the dimension of the amplitude anti-synchronized subspace.

two-laser system [15] and are as follows:

$$\frac{dE_1}{dT} = \tau_c^{-1} [(G_1 - \epsilon_1(T))E_1 - \kappa E_2] + i\omega_1 E_1,$$

$$\frac{dG_1}{dT} = \tau_f^{-1} (p_1(T) - G_1 - G_1|E_1|^2),$$

$$\frac{dE_2}{dT} = \tau_c^{-1} [(G_2 - \epsilon_2(T))E_2 - \kappa(E_1 + E_3)] + i\omega_2 E_2, \quad (1)$$

$$\frac{dG_2}{dT} = \tau_f^{-1} (p_2(T) - G_2 - G_2|E_2|^2),$$

$$\frac{dE_3}{dT} = \tau_c^{-1} [(G_3 - \epsilon_3(T))E_3 - \kappa E_2] + i\omega_1 E_3,$$

$$\frac{dG_3}{dT} = \tau_f^{-1} (p_3(T) - G_3 - G_3|E_3|^2).$$

In these equations, τ_c is the cavity round-trip time, τ_f is the fluorescence time of the upper lasing level of the Nd^{3+} ion, and $p_i(T) = p_{0i} + p_{1i}\cos(\Omega T)$, $\epsilon_i(T) = \epsilon_{0i} + \epsilon_{1i}\cos(\Omega T)$, and ω_i are the modulated pump parameters, modulated losses, and detunings (from a common cavity mode), respectively,

TABLE I. Dynamically invariant subspaces in Eqs. (3). A list of symmetry forced invariant subspaces of the equations for a system of three linearly coupled lasers. We have listed only those states that contained an attractor in the numerical simulations. Note that other states exist but are not seen as attracting for the system.

Symmetry	Representative point	Dim.	Name
$Z_2(\xi) \times Z_2(\mu)^{00}$	$(X_+, F_+, X_2, F_2, 0, 0, 0, 0)$	4	synchronized
$Z_2(\xi) \times Z_2(\mu)^{\pi\pi}$	$(X_+, F_+, X_2, F_2, 0, 0, \pi, \pi)$	4	antisynchronized
$Z_2(\mu\xi)$	$(X_+, F_+, X_2, F_2, 0, 0, \phi, -\phi)$	5	amplitude antisynchronized
$Z_2(\mu)^{00}$	$(X_+, F_+, X_2, F_2, X_-, F_-, 0, 0)$	6	phase synchronized
$Z_2(\mu)^{\pi\pi}$	$(X_+, F_+, X_2, F_2, X_-, F_-, \pi, \pi)$	6	phase antisynchronized

of laser i . It is assumed that *not* both the pump and the loss are modulated at the same time. In the Nd:YAG lasers considered in the experiments, the round-trip time of light in the cavity τ_c is 0.40–0.50 ns, while the decay time of the upper lasing level τ_f is $\sim 240 \mu\text{s}$. Ω is the modulation frequency and is chosen to be near the relaxation frequency.

The lasers are coupled linearly to one another with strength κ_{ij} , assumed to be small. For laser beams of Gaussian intensity profile and $1/e^2$ beam radius w_0 the coupling strength, as determined from overlap integral of the two electric fields i and j is defined as

$$\kappa_{ij} = \exp\left(-\frac{(d_i - d_j)^2}{2w_0^2}\right). \quad (2)$$

The coupling strength is normalized such that $\kappa_{ij} = 1$ if $d_i - d_j = 0$. As the coupling between lasers 1 and 3 is assumed negligible, only nearest-neighbor coupling is considered in 1.

In the analysis that follows we only consider the case of loss modulation, i.e., $p_{11} = p_{12} = p_{13} = 0$, but note that the analysis is equally valid in the case of pump modulation [18].

We first let $E_i = X_i e^{i\phi_i}$ where X_i is the amplitude and ϕ_i the phase of laser i and rescale time, expressed in units of the round-trip time of light around the cavity τ_c . We subsequently introduce $\Phi_L = \phi_2 - \phi_1$ and $\Phi_R = \phi_2 - \phi_3$ (and similarly for Δ_L and Δ_R), so that we may rewrite Eqs. (1) as the following system of ordinary differential equations defined on \mathbb{R}^5 ,

$$\begin{aligned} \frac{dX_1}{dt} &= [F_1 - \epsilon_1(t)]X_1 - \kappa X_2 \cos(\Phi_L), \\ \frac{dF_1}{dt} &= \gamma(A - F_1 - F_1 X_1^2), \\ \frac{dX_2}{dt} &= [F_2 - \epsilon_2(t)]X_2 - \kappa(X_1 \cos(\Phi_L) + X_3 \cos(\Phi_R)), \\ \frac{dF_2}{dt} &= \gamma(A - F_2 - F_2 X_2^2), \\ \frac{dX_3}{dt} &= [F_3 - \epsilon_3(t)]X_3 - \kappa X_2 \cos(\Phi_R), \\ \frac{dF_3}{dt} &= \gamma(A - F_3 - F_3 X_3^2), \end{aligned} \quad (3)$$

$$\frac{d\Phi_L}{dt} = \Delta_L + \kappa \left(\left(\frac{X_2}{X_1} + \frac{X_1}{X_2} \right) \sin(\Phi_L) + \frac{X_3}{X_2} \sin(\Phi_R) \right),$$

$$\frac{d\Phi_R}{dt} = \Delta_R + \kappa \left(\left(\frac{X_3}{X_2} + \frac{X_2}{X_3} \right) \sin(\Phi_R) + \frac{X_1}{X_2} \sin(\Phi_L) \right).$$

The issue of synchronization between the two outer lasers may be addressed by introducing the sum and difference of these lasers and assuming that all three lasers are equally detuned, i.e., $\Delta_L = \Delta_R = 0$. Then, $X_{13+} = \frac{1}{2}(X_1 + X_3)$, X_{13-}

$= \frac{1}{2}(X_1 - X_3)$, $F_{13+} = \frac{1}{2}(F_1 + F_3)$, $F_{13-} = \frac{1}{2}(F_1 - F_3)$, and synchronization between the two outer lasers occurs when $X_{13-} = F_{13-} = 0$. The transformed system is equivariant under the action of the following symmetries:

$$\begin{aligned} \xi(X_+, F_+, X_2, F_2, X_-, F_-, \Phi_L, \Phi_R) \\ = (X_+, F_+, X_2, F_2, -X_-, -F_-, \Phi_L, \Phi_R), \end{aligned}$$

corresponding to interchanging the two outer lasers,

$$\begin{aligned} \mu(X_+, F_+, X_2, F_2, X_-, F_-, \Phi_L, \Phi_R) \\ = (X_+, F_+, X_2, F_2, X_-, F_-, -\Phi_L, -\Phi_R), \end{aligned}$$

corresponding to conjugating the phases of the electric fields of all three lasers.

There is also a parameter symmetry involving the coupling parameter κ that takes

$$(\kappa, \Phi_L, \Phi_R) \rightarrow (-\kappa, \Phi_L + \pi, \Phi_R + \pi),$$

which adds π onto the phase of the middle laser while reversing the sign of κ . It is interesting to note that all three lasers are phase synchronized when κ is negative, corresponding to $\Phi_L = \Phi_R = 0$. However, only the two outer lasers are phase synchronized when κ is positive and this is the physically relevant situation since κ is assumed positive in some sense.

Owing to these symmetries, the dynamically invariant subspaces illustrated in Table I exist. Notice, in particular, the five-dimensional subspace labeled amplitude antisynchronized, corresponding to the case where the μ symmetry has been broken, via equal detuning of the two outer beams from a common cavity mode. The dimensionality of the experimental system as calculated using the false nearest-neighbor method gives good agreement with this state and gives emphasis to our assumptions about the parameter regimes considered.

Note that although there are several invariant subspaces where the phases of all three lasers are locked, there are *no* invariant subspaces forced by symmetry such that all the amplitude and gains are equal, $X_+ = X_2$ and $F_+ = F_2$. We may examine this using two approaches; first by examining the set of such points in the phase space and showing that it is not invariant (cf. [19]) and second by reducing the system of three lasers to one of two lasers with unequal coupling.

To this end, we define the manifold

$$\mathcal{M}_{12} = \{(X_1, F_1, X_2, F_2, X_3, F_3, \Phi_L, \Phi_R) :$$

$$X_1 = X_2, F_1 = F_2 \text{ \& \; } \Phi_R = 0 \text{ or } \pi\}$$

corresponding to perfect (anti)synchronization between lasers 1 and 2 in terms of the original variables.

A. Noninvariance of \mathcal{M}_{12}

We demonstrate that if $\kappa \neq 0$, any nonzero trajectory can only be in \mathcal{M}_{12} instantaneously, by assuming that X_1 and X_2 are nonzero and examining the evolution of the difference $x_- = \frac{1}{2}(X_1 - X_2)$ and sum $x_+ = \frac{1}{2}(X_1 + X_2)$. Note that

$$\frac{dx_-}{dt} = \frac{F_1 + F_2}{2}x_- + \frac{F_1 - F_2}{2}x_+ - \epsilon(t)x_- + \kappa x_- \cos \Phi_L + \frac{1}{2}\kappa X_3 \cos \Phi_R.$$

If the system state lies on \mathcal{M}_{12} this means that $x_- = 0$ and $F_1 = F_2$; so the trajectory at this point will have

$$\frac{dx_-}{dt} = \frac{1}{2}\kappa X_3 \cos(\Phi_R).$$

Thus the trajectory must leave \mathcal{M}_{12} unless $\kappa = 0$, $X_3 = 0$ and/or $\Phi_R = (\pi/2) + k\pi$, $k \in \mathbb{Z}$. We eliminate the first possibility by assumption. If $X_3 = 0$ then we note that

$$\frac{dX_3}{dt} = -\kappa X_2 \cos(\Phi_R) \quad (4)$$

and so this will be nonzero as long as $\Phi_R \neq (\pi/2) + k\pi$ for some $k \in \mathbb{Z}$, but from our definition of \mathcal{M}_{12} , $\Phi_R = 0$ or π , so any trajectory satisfying Eq. (4) will not be contained in \mathcal{M}_{12} . For the same reason we rule out the case $\Phi_R = (\pi/2) + k\pi$ and this implies that a trajectory can only be in \mathcal{M}_{12} for an instant in time. As a result, \mathcal{M}_{12} is *only* an invariant subspace for the ordinary differential equation if $\kappa = 0$ and the only trajectories that remain within \mathcal{M}_{12} for all time have $X_1 = X_2 = X_3 = 0$.

B. Reduction to a system of two lasers with unequal coupling

If we assume that we lie on one of the amplitude synchronized subspaces, where $X_- = F_- = 0$, i.e., $X_1 = X_3$ and $F_1 = F_3$, then the system (3) simplifies to a two laser system with unequal coupling between the two lasers.

$$\frac{dX_1}{dt} = [F_1 - \epsilon(t)]X_1 - \kappa X_2 \cos(\Phi),$$

$$\frac{dF_1}{dt} = \gamma(A - F_1 - F_1 X_1^2),$$

$$\frac{dX_2}{dt} = [F_2 - \epsilon(t)]X_2 - 2\kappa X_1 \cos(\Phi), \quad (5)$$

$$\frac{dF_2}{dt} = \gamma(A - F_2 - F_2 X_2^2),$$

$$\frac{d\Phi}{dt} = \kappa(X_2 X_1^{-1} + 2X_1 X_2^{-1})\sin(\Phi).$$

Introducing sum and difference variables in this case gives us the transformed system,

$$\frac{dX_+}{dt} = X_+(F_+ - \epsilon(t)) + F_- X_- - \kappa \cos(\Phi)(3X_+ + X_-),$$

$$\frac{dF_+}{dt} = \gamma(A - F_+(1 + X_+^2 + X_-^2) - 2F_- X_- X_+),$$

$$\frac{dX_-}{dt} = X_-(F_+ - \epsilon(t)) + F_- X_+ + \kappa \cos(\Phi)(3X_- + X_+), \quad (6)$$

$$\frac{dF_-}{dt} = -\gamma(F_-(1 + X_+^2 + X_-^2) + 2F_+ X_- X_+),$$

$$\frac{d\Phi}{dt} = \kappa \left(\frac{3(X_+^2 + \frac{2}{3}X_+ X_- + X_-^2)}{(X_+^2 - X_-^2)} \right) \sin(\Phi)$$

If we assume that the two lasers X_1 and X_2 are synchronized then we find that

$$\frac{dX_-}{dt} = \kappa \cos(\Phi)X_+,$$

$$\frac{dF_-}{dt} = 0, \quad (7)$$

$$\frac{d\Phi}{dt} = 3\kappa \sin(\Phi),$$

assuming that $\kappa \neq 0$, $X_+ \neq 0$, then we see that $X_- = 0$ for at most an instant in time. Since if $\cos(\Phi) = 0$ then $\Phi = (\pi/2) + k\pi$ for some $k \in \mathbb{Z}$ and so

$$\frac{d\Phi}{dt} = 3\kappa, \quad (8)$$

which is nonzero and therefore Φ moves away from $(\pi/2) \pmod{\pi}$. Consequently dX_-/dt moves away from 0 and so X_- also moves from 0. Therefore synchronization is not achieved in the asymmetric two laser setup and thus not achieved in the original three laser system.

IV. NUMERICAL RESULTS

We carried out numerical simulations independently in both the loss modulation situation as well as modulation of the pump excitation. We concentrate on the loss modulated situation due to numerical considerations, but note that our results remain valid in the case of pump modulation [18].

A. Loss modulated case

For the loss modulated case, the simulations were performed using both Bulirsch-Stoer and Runge-Kutta integrators. Due to numerical considerations we were forced to consider more moderate values of the stiffness parameter γ , which was of the order 0.01 and 0.001. The parameter regimes considered were also altered in order that the difference in γ was taken into account. In both the cases $\gamma = 0.01$ and $\gamma = 0.001$ we saw similar results, and although

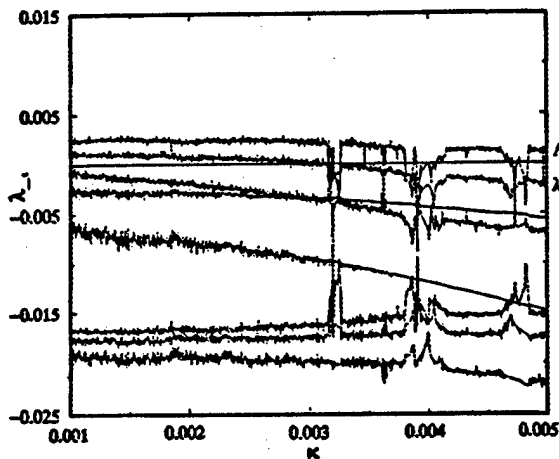


FIG. 6. Lyapunov exponent diagram in the case of modulated loss. The parameter values for the lasers were assumed identical and were $\alpha_{0i}=0.9, \alpha_{1i}=0.2, p_i=1.2$ (for $i=1,2,3$). We assumed the detunings of the lasers were such that $\Delta_L=\Delta_R=0$. We have labeled the largest tangential Lyapunov exponent λ_1 . Notice that this is positive for most values of the coupling strength κ . The non-normality of κ is apparent through the windows of stability that arise when varying κ . These correspond to the periods where λ_1 is negative. The blowout occurs when the normal Lyapunov exponent, λ_1 passes through 0. In this case this occurs for $\kappa \sim 0.003125$.

the experiments were carried out with $\gamma \sim 10^{-6}$, the use of longer resonators would give a value of the stiffness parameter somewhat closer to that considered numerically. We carried out simulations for many values of the pump coefficient and various modulation strengths for the loss.

As in the model for a two laser system, in the case $0 < \gamma \ll 1$, the system undergoes a period doubling cascade to chaos as the strength of loss modulation is increased. Typically we see that for small values of the coupling parameter κ , there is no amplitude synchronization and the amplitude behavior of all three lasers appears to be independent, although with antiphase synchronization between adjacent lasers. As the coupling strength is increased, a period of on-off intermittent type behavior [20], is observed in the amplitude fluctuations of the two outer lasers. During this period there are times when the two outer lasers appear to be synchronized in both amplitude and phase, before bursts away from amplitude synchronization, while remaining completely phase (anti)synchronized. Then as the coupling strength is increased still further, there is no more bursting away from synchrony and the two outer lasers remain amplitude synchronized for all time after an initial transient phase.

For the particular case where all losses are modulated equally at the rate, $0.9 + 0.2 \cos(0.045 t)$, the pump parameters were equal to 1.2 for each laser and $\Delta_L=\Delta_R=0$, the behavior of a typical trajectory is as follows. Upon varying the strength of coupling κ , we see that there exists a critical value $\kappa_c \sim 0.003125$ such that for values of $\kappa < \kappa_c$, trajectories evolve on to the phase antisynchronized state. For values of $\kappa > \kappa_c$ trajectories evolve on to the amplitude antisynchronized state. This transition at κ_c is strongly suggestive of a *blowout* bifurcation, as was the case in a system of two lasers [14].

A *blowout* bifurcation occurs when a *normal* Lyapunov exponent governing the exponential rate of change transverse

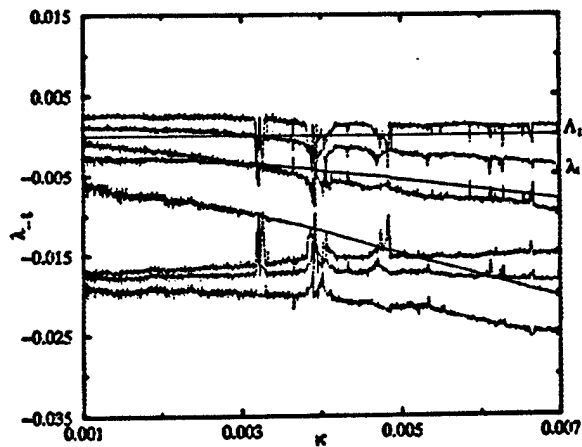


FIG. 7. Lyapunov exponent diagram in the case of modulated loss. Here the detunings were assumed equal with $\Delta_L=\Delta_R=0.001$ and the exponents were plotted upon varying the strength of coupling κ . The parameter values for the lasers were assumed identical and were once again $\alpha_{0i}=0.9, \alpha_{1i}=0.2, p_i=1.2$ (for $i=1,2,3$). We have labeled the largest tangential Lyapunov exponent λ_1 and the normal Lyapunov exponent λ_1 . Similar behavior to the case of no left and right detuning is seen. However, the point of blowout is altered, in this case $\kappa \sim 0.003175$.

to a submanifold of the total phase space passes through 0. In the case where there is more than one transverse Lyapunov exponent we need consider only the largest or *normal* Lyapunov exponent. If the normal exponent is negative, then on average nearby trajectories are attracted onto the submanifold and the attractor within the subspace is an attractor for the full system. If the exponent is positive then on average trajectories close to the submanifold are repelled away from it.

We have numerically computed the Lyapunov exponents of Eq. (3) by integrating the variational equations and examine the change that occurs in the exponents upon varying the coupling strength κ . These are illustrated in the case of no detunings in Fig 6.

For this system, the blowout bifurcation does not occur at an isolated parameter value because the bifurcation parameter κ varies the dynamics tangentially within the antisynchronized subspace as well as those in a transverse direction from it; it is not a *normal parameter* for the dynamics [21,22]. Because of this (and apparent fragility of the chaotic attractors) we do not expect the Lyapunov exponents to vary smoothly or even continuously with the parameter. Hence we observe a *blurred blowout* [22].

The tangential variation of the dynamics is clearly indicated in Figs. 6 and 7, where windows of stability arise as the coupling strength κ is increased. These windows of stability correspond to all Lyapunov exponents of system (3) being negative. In particular, there is a window of stability shortly after the bifurcation point.

In order to examine the branching behavior at blowout, we have simulated the behavior of typical trajectories that are not in any invariant subspace. Starting at κ_c , there appears to exist a chaotic attractor A within the antisynchronized subspace, since after an initial transient phase (which may be prolonged for some initial conditions), all trajectories eventually appear to converge to the antisynchronized sub-

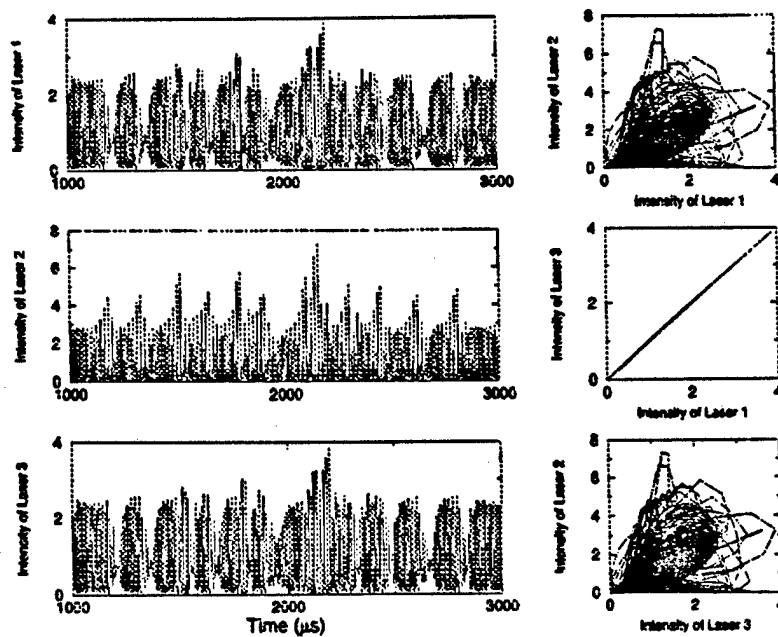


FIG. 8. Numerical simulated three laser model with pump modulation. The modulation rate was again chosen to be near the relaxation oscillation frequency of the lasers so as to induce chaotic fluctuations in the intensities.

space. Reducing κ towards κ_c we find regions of region of on-off intermittent type behavior, typical for a supercritical blowout.

After the blowout, we no longer observe any attractors in the antisynchronized subspace, but there is a new branch of attractors in the phase antisynchronized subspace are created at the bifurcation. Just after κ_c these attractors are apparently on-off intermittent and close to the antisynchronized subspace. The average position of the trajectory moves away as $\kappa \rightarrow 0$. This is a strong indicator that the blowout is of supercritical, soft or nonhysteretic type [16].

We also performed simulations of three loss modulated lasers in situations where the detunings were equal, i.e., $\Delta_L = \Delta_R = \Delta$. We calculated the Lyapunov spectrum in this case and saw similar results to that of the purely symmetric case, with the main difference being a bifurcation from the amplitude antisynchronized subspace, rather than the anti-synchronized subspace. Again the blowout appears to be soft with an extended period of on-off intermittent behavior.

For the particular case with parameters identical to those considered above and a value of the detuning, $\Delta = 0.001$, the Lyapunov spectrum upon varying κ is illustrated in Fig. 7. Again a blurred blowout is evident, and the normal Lyapunov exponent passes through zero at $\kappa_c \sim 0.003\,175$.

B. Pump modulation

The numerical simulations in the case of modulation of the pump excitation were carried out using a Runge-Kutta integrator with a variable time step. Frequency of the depth of modulation was chosen so that the dynamics of the system was in a region of chaotic behavior and in this case was chosen to be 100.53 kHz (in the case of loss modulation it was 139.62 kHz). As in the case of loss modulation, excellent agreement between the experimental results and the numerical simulations are seen. A high degree of synchronization between the two outer lasers and no apparent

synchronization between outer and inner laser. The transient behavior displayed similar characteristics when compared to the loss modulated simulations, such as bursts away from synchronization over short time scales, before settling on to the synchronized subspace after longer periods of time.

Some of the numerical simulations we performed are illustrated in Fig. 8. The bifurcation analysis is not performed here, since the simulations indicate similar bifurcation behavior to that of the loss modulated case, as would be expected [18].

V. DISCUSSION

Concluding this work, the synchronization of three class B Nd:YAG lasers, coupled in a straight line linear array, is investigated experimentally, analytically and numerically. We investigate the separate cases of pump modulation and loss modulation both experimentally and numerically. In the experiments, a high degree of synchronization is observed between the two outer lasers of the array, while no synchronization is observed between outer and inner lasers. This is in good agreement with the theory, which demonstrates this lack of synchronization between outer and inner laser. In the case of loss modulation we see numerically how the loss of synchronization between the two outer lasers is lost in both the fully symmetric case and in the case with equal left and right detunings, via an apparent supercritical blowout bifurcation. This is achieved by varying the strength of coupling between the three lasers.

For the experimental system, noise and symmetry breaking are both inherent, but even with quite high levels of noise, we have demonstrated a good degree of synchronization particularly in the loss modulated case. In the numerical simulations, noise and symmetry breaking have similar effects; in the region of on-off intermittency, it is unlikely that there will be a noticeable change if the perturbations are

small. Low levels of noise and imperfections can result in *bubbling* type effects [23], which can resemble on-off intermittency in numerical simulations. Consequently, the effect of bubbling on systems such as ours is similar to the effects of on-off intermittency, namely bursts away from a synchronized state. Such bubbling persists up to a point known as a *bubbling transition* [24] (see also the related riddling bifurcation [25]). This situation arises when an orbit embedded in a symmetric chaotic attractor loses its transverse stability. A more detailed description of this situation may be found in [26].

It is interesting to see the harmonic relationships between the central and the outer beams. Particularly for the loss modulated case with small nearest-neighbor separations, the central beam appeared to be at a rate approaching twice that of the two outer beams. We conjecture that this surprising phenomenon may be caused by the central beam communicating a greater quantity of information than the two outer beams. One area of future research is to investigate these dynamics and examine the effect of parameter variation on the harmonic relationship.

Although we have shown that there will be no synchronization between the outer and inner lasers in a three laser array, the question of generalized synchronization [27] arises. As we have shown, assuming that the two outer lasers are synchronized allows us to simplify the model to a system of two lasers with unequal coupling between the two lasers. This does not immediately fall into the category of general-

ized synchronization, since there is feedback from the "response" system into the "driving" system. However, it may still be possible to make similar conclusions to those of generalized synchronization in the case where the feedback from the one system is small compared to the input from the other.

Numerical simulations of the model suggests that for small symmetry breaking perturbations of the amplitude synchronized state, an instability should arise in the phase locking of the three lasers as predicted analytically and numerically in a system of two lasers coupled in a linear straight line array [19]. Another interesting area of future experimental work would be to heterodyne the outer beams, examine the beat frequencies over time to investigate the phase-locking instability. Such an instability may have an important bearing on maximizing power output and coherence in larger arrays of coupled lasers.

ACKNOWLEDGMENTS

J.T. and P.A. gratefully acknowledge the support of the EPSRC via Grant No. GR/K77365. J.T., K.S.T.J., D.J.D., G.D.V., R.R., and S.Z. gratefully acknowledge support from the U.S. Office of Naval Research. It is a pleasure to also thank the Georgia Institute of Technology and the China Scholarship Council for their financial support (S.Z.). Finally, we would like to thank Steve Strogatz and Henry Abarbanel for a helpful discussion concerning generalized synchronization.

-
- [1] L. M. Pecora and T. L. Carroll, *Phys. Rev. Lett.* **64**, 821 (1990).
 - [2] L. M. Pecora and T. L. Carroll, *Phys. Rev. A* **44**, 2374 (1991).
 - [3] K. M. Cuomo and A. V. Oppenheim, *Phys. Rev. Lett.* **71**, 65 (1993).
 - [4] L. Kocarev and U. Parlitz, *Phys. Rev. Lett.* **74**, 5028 (1995).
 - [5] G. D. VanWiggeren and R. Roy, *Science* **279**, 1198 (1998).
 - [6] G. D. VanWiggeren and R. Roy, *Int. J. Bif. Chaos* (to be published).
 - [7] A. V. Gaponov-Grekhov, M. I. Rabinovich, and I. M. Starobinets, *Pis'ma Zh. Éksp. Teor. Fiz.* **39**, 561 (1984) [*JETP Lett.* **39**, 688 (1984)].
 - [8] V. S. Afraimovich, N. N. Verichev, and M. I. Rabinovich, *Izv. Vyssh. Uchebn. Zaved. Radiofiz.* **29**, 1050 (1986) [*Sov. Radiophys.* **29**, 795 (1986)].
 - [9] S. K. Han, C. Kurrer, and Y. Kuramoto, *Phys. Rev. Lett.* **75**, 3190 (1995).
 - [10] H. G. Winful and L. Rahman, *Phys. Rev. Lett.* **65**, 1575 (1990).
 - [11] L. Fabiny, P. Colet, R. Roy, and D. Lenstra, *Phys. Rev. A* **47**, 4287 (1993).
 - [12] R. Roy and K. S. Thornburg, Jr., *Phys. Rev. Lett.* **75**, 3190 (1995).
 - [13] K. S. Thornburg, Jr., M. Möller, R. Roy, T. W. Carr, R.-D. Li, and T. Erneux, *Phys. Rev. E* **55**, 3865 (1997).
 - [14] P. Ashwin, J. R. Terry, K. S. Thornburg, Jr., and R. Roy, *Phys. Rev. E* **58**, 7186 (1998).
 - [15] R. Roy and K. S. Thornburg, Jr., *Phys. Rev. Lett.* **72**, 2009 (1994).
 - [16] E. Ott and J. C. Sommerer, *Phys. Lett. A* **188**, 39 (1994).
 - [17] H. D. I. Abarbanel, *Analysis of Observed Chaotic Data* (Springer, Berlin, 1996).
 - [18] J. R. Tredicce, N. B. Abraham, G. P. Puccioni, and F. T. Arecchi, *Opt. Commun.* **55**, 131 (1985).
 - [19] J. R. Terry, *J. Opt. B* (to be published).
 - [20] N. Platt, E. A. Spiegel, and C. Tresser, *Phys. Rev. Lett.* **70**, 279 (1993).
 - [21] P. Ashwin, J. Buescu, and I. N. Stewart, *Nonlinearity* **9**, 703 (1996).
 - [22] P. Ashwin, E. Covas, and R. Tavakol, University of Surrey Technical Report No. 98/3, 1998 (unpublished).
 - [23] P. Ashwin, J. Buescu, and I. Stewart, *Phys. Lett. A* **193**, 126 (1994).
 - [24] S. C. Venkataramani, B. R. Hunt, E. Ott, D. J. Gauthier, and J. C. Biefang, *Phys. Rev. Lett.* **77**, 5361 (1996).
 - [25] Yu. L. Maistrenko, V. L. Maistrenko, A. Popovich, and E. Mosekilde, *Phys. Rev. E* **57**, 2713 (1998).
 - [26] Y.-C. Lai, C. Grebogi, J. A. Yorke, and S. C. Venkataramani, *Phys. Rev. Lett.* **77**, 55 (1996).
 - [27] N. F. Rulkov, M. M. Sushchik, L. S. Tsimring, and H. D. I. Abarbanel, *Phys. Rev. E* **51**, 980 (1995).

Transmission of linearly polarized light through a single-mode fiber with random fluctuations of birefringence

Gregory D. VanWiggeren and Rajarshi Roy

A simple theoretical formalism is developed to describe the effect of transmission on linearly polarized light through a fiber with random fluctuations of birefringence. We conclude that, for any optical fiber that does not experience polarization-dependent gain or loss, there exist two orientations for linearly polarized light input into the optical fiber that will also exit the fiber linearly polarized. We report experimental results that verify this prediction and also investigate its practical implications and limitations; in particular we investigate the stability of these linearly polarized output states in laboratory conditions. © 1999 Optical Society of America

OCIS codes: 060.2310, 060.2400, 060.2430, 060.2420, 260.1440, 260.5430.

1. Introduction

When one works with fiber-optic systems in the laboratory, it is often desirable to couple linearly polarized light into a fiber and to obtain linearly polarized light at the output as well. One way to accomplish this is to use polarization-maintaining fibers. The high birefringence of these fibers allows for linearly polarized light launched along the proper axis to travel long distances without change of polarization state. In ordinary single-mode fiber, however, the polarization state evolves rapidly as the light propagates. The output polarization will appear uncorrelated to the input polarization after only a few meters of propagation. However, it can be shown that unperturbed single-mode fiber can perform the same function as polarization-maintaining fiber in certain situations. In this paper we predict theoretically and demonstrate experimentally that, for any ordinary single-mode optical fiber, two orientations of linearly polarized quasi-monochromatic input light will also exit the fiber linearly polarized. When the ordinary single-mode fiber is not perturbed by external stresses or temperature changes, these states are

reasonably stable for hours—especially for shorter fiber lengths (100 m or less).

Earlier researchers¹⁻⁴ have also observed linearly polarized input and output of light through a fiber. In Refs. 1 and 2 it is noted that linear light input into a fiber can be output linearly polarized as well, but no theoretical explanation is provided. In Refs. 3 and 4 the observations of linearly polarized input and output of light through a fiber were explained with a model that treats the birefringence of the optical fiber as constant in magnitude and orientation throughout the length of the fiber. This assumption is not, in general, correct. Much of the research into the propagation of polarized light in optical fiber has been in the context of polarization-mode dispersion,^{5,6} a subject that is not addressed in this paper.

Here the birefringence fluctuations along a fiber are treated as a concatenation of wave plates with each wave plate possessing an arbitrary birefringence. The simple Jones matrix formalism used to analyze such a concatenation provides a framework for understanding many polarization phenomena observed in optical fiber, including polarization-mode dispersion⁵ and four-wave mixing in single-mode fiber.⁷ The formalism can be used to show that the operation of randomly fluctuating birefringences in an optical fiber is the same as the operation of only one constant birefringence for the whole fiber, as was assumed in Refs. 3 and 4. The formalism provides a simple way of mathematically determining the particular orientation of linearly polarized input light that will also exit a fiber linearly polarized. It

The authors are with the School of Physics, Georgia Institute of Technology, Atlanta, Georgia 30332. The e-mail address for G. D. VanWiggeren is greg@socrates.physics.gatech.edu.

Received 23 October 1998; revised manuscript received 3 March 1999.

0003-6935/99/183888-05\$15.00/0

© 1999 Optical Society of America

clearly indicates that only two such orientations can exist, that they are orthogonal, and that in general they are not eigenpolarizations. In fact, this formalism shows that the polarization state of eigenpolarized light can evolve as it propagates through the fiber. Finally, the framework offers a way of understanding the effects of polarization-dependent gain or loss in an optical fiber. Experiments verifying these predictions and demonstrating their usefulness in a laboratory setting are performed and the results given in Sections 3 and 4.

2. Theory

At any point along a single-mode fiber the local birefringence is typically of the order of $10^{-7} < (n_1 - n_2)/\sqrt{n_1 n_2} < 10^{-5}$.⁸ Even such a small birefringence can lead to large changes in the polarization state of light over 1 m. In real fibers the magnitude of the birefringence is never constant throughout a length of fiber. Instead, it fluctuates according to whatever local stresses, internal or external, exist in the fiber. To complicate matters further, the orientation of the index ellipsoid rotates unpredictably from one point to the next in fiber and is sensitive to movement of the fiber or to changes in temperature. The birefringence in an optical fiber is also a function of wavelength, but this wavelength dependence is not accounted for in the analysis given. Consequently, the results from the analysis presented in this paper are valid only in situations in which this wavelength dependence can be neglected. This condition is often well satisfied in laboratory settings where the bandwidths of the optical sources are typically 1 nm or less and the lengths of fiber are less than a few kilometers.

As mentioned above, a length of single-mode optical fiber is modeled here as a concatenation of differential elements, each element a wave plate possessing a birefringence of arbitrary orientation and magnitude. After passing through one element, the light passes into a second element, and so on, until it reaches the end of the fiber. In a Jones matrix representation⁹ this process can be described a series of phase-shift and rotation matrices^{10,11}:

A phase shift of δ is described by the matrix

$$C(\delta) = \begin{bmatrix} \exp(i\delta/2) & 0 \\ 0 & \exp(-i\delta/2) \end{bmatrix}. \quad (1)$$

In the model the phase shift is given by $\delta = 2\pi L(n_1 - n_2)/\lambda$, where L is the length of the differential element and n_1 and n_2 are the indices of refraction along the fast and slow axes, respectively. A rotation of the index ellipsoid by an angle θ is represented by the matrix

$$R(\theta) = \begin{bmatrix} \cos \theta & -\sin \theta \\ \sin \theta & \cos \theta \end{bmatrix}. \quad (2)$$

The polarization properties of a length of fiber, then, can be represented as a product of many unknown phase-shift matrices and rotation matrices:

$$M = C(\delta)R(\theta)C(\epsilon)R(\phi) \dots \quad (3)$$

The product of a phase-shift matrix and a rotation matrix can produce any arbitrary unitary matrix. Consequently, the form of M is also the most general form of a unitary matrix:

$$M = \begin{bmatrix} a & b \\ -b^* & a^* \end{bmatrix}, \quad (4)$$

where $|a|^2 + |b|^2 = 1$. The unitary nature of the matrix M allows for it to be decomposed into only one appropriate phase-shift matrix C multiplied by one rotation matrix R . Interestingly, this suggests that any fiber's net effect on the polarization state of light is identical to the effect of one particular wave plate with a constant phase shift and orientation of its axes.

A proof for the form of M can be given quickly¹¹ with the Pauli matrix

$$\Sigma = \begin{bmatrix} 0 & 1 \\ -1 & 0 \end{bmatrix}.$$

Now Σ has the following properties:

$$\Sigma^2 = -I,$$

where I is the identity matrix,

$$\Sigma R(\theta)\Sigma = -R(\theta), \quad (5)$$

$$\Sigma C\Sigma = -\bar{C},$$

where the elements of \bar{C} are the complex conjugates of the elements of C . If a general matrix form for M is assumed, then

$$M = \begin{bmatrix} a & b \\ c & d \end{bmatrix},$$

where the elements are all complex. Performing the matrix multiplication gives

$$\Sigma M \Sigma = -\begin{bmatrix} d & -c \\ -b & a \end{bmatrix}. \quad (6)$$

From Eq. (3) it is also true that

$$\begin{aligned} \Sigma M \Sigma &= \Sigma C(\delta)R(\theta)C(\epsilon)R(\phi) \dots C(\gamma)R(\psi)\Sigma \\ &= -\Sigma C(\delta)\Sigma^2 R(\theta)\Sigma^2 \dots \Sigma^2 C(\gamma)\Sigma^2 R(\psi)\Sigma \\ &= -\bar{C}(\delta)R(\theta)\bar{C}(\epsilon)R(\phi) \dots \bar{C}(\gamma)R(\psi) \\ &= -\bar{C}(\delta)\bar{R}(\theta)\bar{C}(\epsilon)\bar{R}(\phi) \dots \bar{C}(\gamma)\bar{R}(\psi) \\ &= -\bar{M} = -\begin{bmatrix} a^* & b^* \\ c^* & d^* \end{bmatrix}. \end{aligned} \quad (7)$$

When we take the results from Eqs. (6) and (7), it is clear that $d = a^*$ and $c = -b^*$ and that the form of M given in Eq. (4) has been proved.

Light in a fiber has electric-field components along two orthogonal transverse axes. These axes are chosen arbitrarily and denoted here as x and y . In the Jones matrix representation these complex components are represented as a vector $\mathbf{j}_{\text{in}} = (E_x, E_y)$. The output fields are represented by $\mathbf{j}_{\text{out}} = (E'_x, E'_y)$. The transformation of light as it propagates through the length of the fiber is thus given by

$$\mathbf{j}_{\text{out}} = \mathbf{M} \cdot \mathbf{j}_{\text{in}} \quad (8)$$

To obtain linearly polarized output from the fiber, the ratio E'_x/E'_y must be real, though both components are in general complex. In other words, the input electric-field components E_x and E_y must satisfy the condition

$$\text{Im}\left(\frac{E'_x}{E'_y}\right) = 0 = \frac{aE_x + bE_y}{-b^*E_x + a^*E_y} - \text{c.c.}, \quad (9)$$

where c.c. is the complex conjugate.

The ratio of the input electric-field components E_x/E_y is also real, because the input light is linearly polarized. Rewriting Eq. (9) in terms of the ratio $r = E_x/E_y$ and rationalizing gives

$$r^2 - \frac{\text{Im}(a^2 - b^2)}{\text{Im}(ab)} r - 1 = 0. \quad (10)$$

The two solutions for r given by Eq. (10) correspond to orientations of linearly polarized input light that will also exit the fiber linearly polarized. By using these solutions for r to construct the vectors $\mathbf{j}_{\text{in}+}$ and $\mathbf{j}_{\text{in}-}$ and then taking the dot product, we can show that the two solutions, and thus their corresponding input orientations, are orthogonal. Finally, solving Eq. (8) for $\mathbf{j}_{\text{out}+}$ and $\mathbf{j}_{\text{out}-}$, we can show that the output orientations are also orthogonal. It should be noted that the polarization states of these solutions are not maintained as they propagate; instead, they evolve continuously. The evolution of these particular orientations, however, is precisely such that the light exits the fiber linearly polarized. It is also important to note that neither $\mathbf{j}_{\text{in}+}$ nor $\mathbf{j}_{\text{in}-}$ is an eigenvalue. Although both the input and the output are linearly polarized, the angular orientation is not necessarily the same.

A less idealized model for a length of optical fiber would have to include effects such as gain or loss. For long fibers, loss may be significant. Gain and loss can be incorporated into the description given above by simple inclusion of an appropriate Jones matrix for a polarization-dependent gain or loss,

$$\mathbf{G}(c, d) = \begin{bmatrix} c & 0 \\ 0 & d \end{bmatrix}, \quad (11)$$

where c and d are real.

The gain or loss need not be oriented along the same direction as the birefringence, but an extra ro-

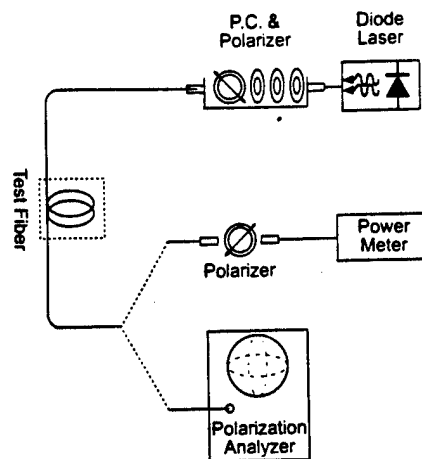


Fig. 1. Experimental setup for measuring polarization of a test fiber. The extinction ratio results were obtained with the second polarizer and the power meter. The results shown in Figs. 2-4 were obtained with the polarization analyzer after the test fiber. P.C., polarization controller.

tation matrix in each differential element would compensate for this. Thus

$$\mathbf{M} = \mathbf{C}(\delta)\mathbf{R}(\theta)\mathbf{G}(c, d)\mathbf{R}(\phi)\mathbf{C}(\epsilon)\mathbf{R}(\psi)\mathbf{G}(e, f)\mathbf{R}(\zeta) \dots \quad (12)$$

By applying \mathbf{G} to the framework developed above, we can show that if $c = d$ then the effect of such a loss or gain is simply to multiply \mathbf{M} by a constant value. In this case the discussion above is unaffected. However, if the elements of \mathbf{G} are not identical, $c \neq d$, in each differential element, the proof given above no longer holds. Stated another way, if a fiber has polarization-dependent gain or loss, \mathbf{M} will not have the same form as in Eq. (4), and the treatment given above will no longer apply.

3. Experiment

Birefringences in a fiber, and thus the matrix \mathbf{M} for that fiber, are highly sensitive to movement and to other environmental perturbations. It is important, therefore, to verify that the theory's predictions can be demonstrated experimentally and to investigate the conditions in which the theory applies.

Figure 1 shows the basic setup. A tunable diode laser is used to produce 4 mW of light with a wavelength of 1550 nm and a 150-kHz linewidth. The light propagates down a fiber and is coupled to free space with a graded-index (GRIN) lens where it passes through a sequence of three wave plates ($\lambda/2$, $\lambda/4$, $\lambda/2$). These three wave plates operate on the light from the tunable diode laser to ensure that the light is roughly circularly polarized when incident on the polarizer so that roughly equal power is transmitted through the polarizer as it is rotated. Another GRIN lens couples the light that passes through the polarizer into the test fiber.

In the first set of experiments the light transmitted by the first polarizer is launched into the test fiber

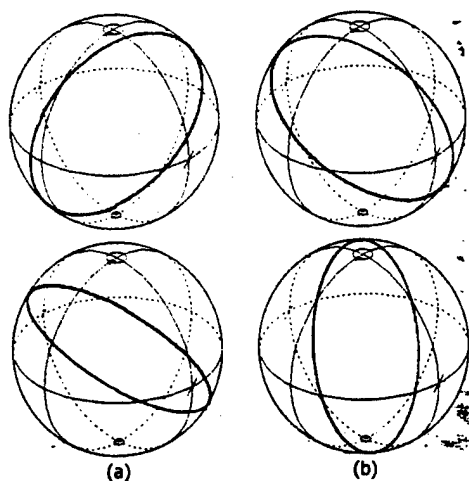


Fig. 2. Polarization state paths (thicker curves) traced at the output of the fiber as the polarizer at the input is rotated through 180° . (a) 8-m test fiber. (b) 35-km test fiber.

and propagates until it reaches a second polarizer. The light that passes through the second polarizer is then input into an optical power meter. The two polarizers are adjusted to achieve maximum extinction as measured by the power meter. Experimentally, two orientations of the first polarizer were found, which allowed for maximum extinction. Thus the experiment demonstrates that two orientations of linearly polarized input light gave linearly polarized light at the output of the test fiber. This was true for both the short, 8-m, and the long, 35-km, lengths of fiber that were tested. For both lengths it was also observed that the orientations of the two linearly polarized inputs were orthogonal to within a measurement error of $\pm 0.5^\circ$. The linearly polarized output, to within the same error, was also orthogonal. All of this is as predicted by the proof developed above. The extinction ratio for the short test fiber was >45 dB, whereas for the 35-km sample it had fallen to 35 dB. In all cases the ratio is large enough to accurately determine the location of the extinction maxima. The decrease in the extinction ratio is most probably due to scattering phenomena that depolarize the propagating light.

As a measure of the wavelength dependence of this result, amplified spontaneous emission light from an erbium-doped fiber amplifier (EDFA) was used as the source. The amplified spontaneous emission light is very broadband, possessing a 3-dB bandwidth of approximately 5 nm centered at 1532 nm. Even with such broadband light, a >15 -dB extinction ratio was obtained after propagation through an approximately 1.5-km optical fiber.

Another set of experiments was performed with a polarization analyzer. For the 8-m and the 35-km test fibers mentioned above, a series of measurements were made in which the input polarizer was rotated, and the resulting polarization states were tracked on the Poincaré sphere. As can be seen in Fig. 2, rotating the polarizer through 180° causes

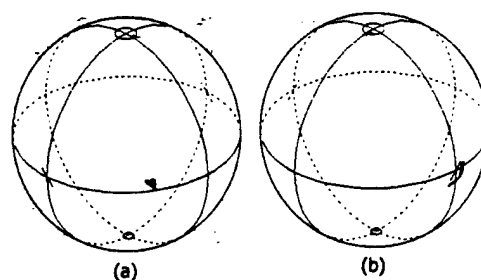


Fig. 3. Smear of points on the Poincaré sphere represent the evolution of the output polarization from an 8-m length of optical fiber during 32 h under typical laboratory conditions. (b) Same experiment showing the evolution of the output state of polarization of a 35-km length of fiber over only 4 h. Both experiments are intended to give some practical indication of the stability of the output polarization of a single-mode fiber when the input polarization is held constant.

great-circle paths to be traced out on the Poincaré sphere. The paths intersect the equator twice, and on opposite sides of the sphere. Because the equator of a Poincaré sphere represents linear polarization ($s_3 = 0$), these paths indicate that two orientations of the input polarizer will result in linearly polarized light output from the fiber. The fact that the intersections with the equator occur on opposite sides of the sphere demonstrates that the two linearly polarized output states are orthogonal, as predicted by the theory. The different paths traced around the Poincaré sphere shown in Fig. 2 for the same fiber are the result of simple rearrangement of the way the fiber lay on the experimental table. This is simply a manifestation of the fact that the polarization properties of fiber are sensitive to changes in external stresses.

For single-mode fiber to be useful in transmitting linearly polarized light from one place to another, the polarization state of the output light should be relatively stable under laboratory conditions. The polarization state of light output from a fiber was tracked over time by a polarization analyzer. As seen in Fig. 2, the polarization state of the output light is represented as a point on the Poincaré sphere. Figure 3 shows the wandering of that point with time. In Fig. 3(a), the 8-m case, the fiber was coiled and lay on an optical table. The data shown were obtained over the course of 32 h. The relatively small excursions show that the polarization state was fairly sta-

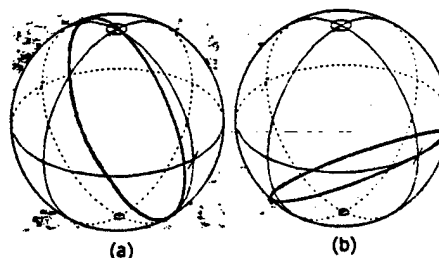


Fig. 4. (a) Polarization path traced by output light after experience of a small polarization-dependent gain in an EDFA. (b) Path traced by output light experiencing polarization-dependent loss.

ble over that entire time. Figure 3(b) was obtained over a period of 4 h with a 35-km length of fiber wrapped around a spool in the same laboratory setting. Not surprisingly, the length of the fiber seems to have an effect on the stability of the polarization state over time.

4. Effects of Loss and Gain

Two more experiments were performed to test the effect of polarization-dependent loss and gain on the polarization properties of a fiber. In the first experiment an EDFA was used as a source of polarization-dependent gain. The amplifier's specifications suggest a polarization-dependent gain of <0.3 dB, which is consistent with the very small (difficult to measure) ~ 0.1 dB of polarization-dependent gain observed in the laboratory for a small-signal gain of ~ 27 dB. Although the EDFA gives an almost polarization-independent amplification of signals, it seems plausible that the winding of the doped fiber and the polarization of the pump lasers would contribute to polarization-dependent gain within individual elements along the fiber. This would result in local differential element gain matrices, $G(c, d)$, which have $c \neq d$. Although the total output power might be almost polarization independent, the form of M would be different from Eq. (4). This polarization gain dependence results in the deviation from a great circle that is observed in Fig. 3(a).

Another experiment was conducted to investigate the effect of polarization-dependent loss. In the test fiber portion of the experiment the light was coupled to free space, again with a GRIN lens. From there it passed through a birefringent calcite crystal that acts as a polarizing beam splitter. When we controlled the angle of a glass plate behind the crystal, the amount of light from each polarization that was coupled through a GRIN lens and back into the test fiber could be controlled. Depending on the angle of the glass plate, one polarization or the other could be coupled preferentially back into the test fiber. This device acts as a polarization-dependent loss. When such a polarization-dependent loss is created, the path on the Poincaré sphere that results from rotation of the input polarizer is not a great circle, as is evident in Fig. 3(b).

5. Conclusion

Using the Jones matrix formalism, we have proved that two orthogonal orientations of linearly polarized light can be launched into any single-mode fiber such that linearly polarized light is output from the fiber. Experiments were performed that verified these predictions. They also revealed, in accordance with the model, that these same predictions cannot be ex-

tended to the case of fiber with polarization-dependent gain or loss.

Knowing that ordinary single-mode fiber can transmit linearly polarized light may have some practical applications in laboratory settings. As with polarization-maintaining fiber, the proper axes for input and output must be found before this property can be used. Unlike with polarization-maintaining fiber, when we obtain linearly polarized input and output light with ordinary single-mode fiber, precautions must be taken against perturbing the fiber once these axes have been found. Although the particular orientation of linearly polarized input and output light for an unperturbed length of fiber may drift on a time scale of minutes or hours, it seems plausible that a simple feedback algorithm could be developed for maintaining the proper axes indefinitely.

We acknowledge support from the Office of Naval Research. We thank P. O'Shea, J. Buck, and A. Judy for helpful discussions and C. Verber for essential instrumentation.

References

1. S. C. Rashleigh, W. K. Burns, R. P. Moeller, and R. Ulrich, "Polarization holding in birefringent single-mode fibers," *Opt. Lett.* **7**, 40-42 (1981).
2. H. G. Winful and A. Hu, "Intensity discrimination with twisted birefringent optical fibers," *Opt. Lett.* **11**, 668-670 (1986).
3. V. Ramaswamy, R. Standley, D. Sze, and W. G. French, "Polarization effects in short length single mode fibers," *Bell Syst. Tech. J.* **57**, 635-651 (1978).
4. K. Okamoto, Y. Sasaki, T. Miya, M. Kawachi, and T. Edauro, "Polarisation characteristics in long length V.A.D. single-mode fibres," *Electron. Lett.* **16**, 768-769 (1980).
5. B. L. Heffner, "PMD measurement techniques—a consistent comparison," in *Optical Fiber Communication Conference*, Vol. 2 of 1996 OSA Technical Digest Series (Optical Society of America, Washington, D.C., 1996), pp. 292-293.
6. C. D. Poole and R. E. Wagner, "Phenomenological approach to polarisation dispersion in long single-mode fibres," *Electron. Lett.* **19**, 1029-1030 (1986).
7. K. Inoue, "Polarization effect on four-wave mixing efficiency in a single-mode fiber," *IEEE J. Quantum. Electron.* **28**, 883-894 (1992).
8. S. C. Rashleigh, "Origins and control of polarization effects in single-mode fibers," *J. Lightwave Technol.* **LT-1**, 312-331 (1983).
9. E. Hecht, *Optics*, 2nd ed. (Addison-Wesley, Reading, Mass., 1990), Chap. 8.
10. R. Roy, C. Brackowski, and G. E. James, "Dynamics of a multimode laser with nonlinear birefringent intracavity elements," in *Recent Developments in Quantum Optics*, R. Inguva, ed. (Plenum, New York, 1993), pp. 309-328.
11. G. E. James, "Models of intracavity frequency-doubled lasers," Ph.D. dissertation (Georgia Institute of Technology, Atlanta, Ga., 1990).

Chaotic Communication using Time-Delayed Optical Systems

Gregory D. VanWiggeren and Rajarshi Roy

School of Physics

Georgia Institute of Technology

Atlanta, GA 30332

Email: rajarshi.roy@physics.gatech.edu

10-22-98

Abstract

We discuss experimental demonstrations of chaotic communication in several optical systems. In each, an erbium-doped fiber ring laser (EDFRL) produces chaotic fluctuations of light intensity onto which is modulated a message consisting of a sequence of pseudorandom digital bits. This combination of chaos and message propagates at a wavelength of ~ 1.5 microns through standard single-mode optical fiber from the transmitter to a receiver, where the message is recovered from the chaos. We present evidence of the high-dimensional nature of the chaotic waveforms and demonstrate chaotic communications through 35 km of single-mode optical fiber at up to 250 Mbit/s, a rate that is, at present, limited only by the speed of our detector electronics.

I. Introduction

A chaotic waveform that serves as a carrier of information represents a generalization of the more traditional sinusoidal carrier and offers the potential for enhanced privacy in communications. In ordinary radio communication, a specific frequency sine-wave carrier is modulated with a message and transmitted. A radio receiver must be tuned to the particular frequency of the carrier sine wave in order to recover the message. In conceptually the same way, the experiments presented here demonstrate that information can be recovered from an optical chaotic carrier using a receiver that is synchronized or "tuned" to the chaotic dynamics of the transmitter.

The synchronization of chaotic systems plays an important role in chaotic communications. The application of chaotic synchronization to secret communication systems was suggested in early work by Pecora and Carroll [1990; 1991]. They discovered that a chaotic transmitter could consist of an electronic circuit that simulated the dynamics, for example, of the Lorenz model [Ditto & Pecora, 1993]. The message to be concealed, assumed small in magnitude, was added to the chaotic fluctuations, assumed to be much larger, of one of the variables (let us choose the z variable for this purpose) and transmitted to the receiver, while another chaotic variable (let us choose x) was separately transmitted. The receiver consisted of a subsystem of the circuits in the transmitter that generated the dynamics of the y and z variables, and was driven by the signal from the x variable of the transmitter. The receiver synchronized to the chaos of the transmitter if the conditional Lyapunov exponents for the systems were negative for the given operating parameters.

One could then recover the message from the chaos through a subtraction at the receiver.

Cuomo and Oppenheim [1993; see also Strogatz, 1994] introduced an elegant variation of the method above that did not require the separate transmission of a driving signal to the receiver. They showed that the receiver could actually synchronize to the chaotic dynamics of the transmitter even when a message was added to the chaotic driving signal from the transmitter. The synchronized output from the receiver was then used to subtract out the information from the transmitted signal. The synchronization was not perfect, and the message, treated as a perturbation of the chaotic signal, had to be small compared to the chaos [Cuomo *et al.*, 1993]. Development of techniques in which the message actually drives the chaotic transmitter system, in addition to being transmitted, were made by Wu and Chua [1993], Volkovskii and Rulkov [1993], and by Parlitz *et al.* [1996]. The synchronization between receiver and transmitter can be exact, so message recovery can be very accurate in principle. The experiments reported in this paper are related in spirit to a method developed first in electronic systems by Volkovskii and Rulkov [1993], who suggested the use of an open-loop system in the receiver. A different, adaptive approach to synchronization and secure communications was introduced by Boccaletti, Farini and Arecchi [1997].

A proposal to use modulated unstable periodic orbits (UPOs) for secure communications and multiplexing was made by Abarbanel and Linsay [1993]. Multiplexing would be possible by using different UPOs to carry different messages. An alternate approach to chaotic communications with UPOs was developed by Hayes *et al.* [1993; 1994]. They symbolically encoded digital information into UPOs of a chaotic

system and used chaos control methods to switch between different orbits. This approach does not attempt to provide any privacy to the information being transmitted.

The issue of privacy, however, arises naturally in a discussion of chaotic communication and is an important motivation for chaotic communication research. In his pioneering paper, "Communication Theory of Secrecy Systems", Claude Shannon discussed three aspects of secret communications systems: concealment, privacy, and encryption [1949; see also Hellman, 1977; Welsh, 1988]. These aspects apply to systems that use chaotic waveforms for communication and can be interpreted in that context. Concealment of the information occurs because the chaotic carrier or masking waveform is irregular and aperiodic; it is not obvious to an eavesdropper that an encoded message is being transmitted at all. Privacy in chaotic communication systems results from the fact that an eavesdropper must have the proper hardware and parameter settings in order to decode and recover the message. In conventional encryption techniques, a key is used to alter the symbols used for conveying information. The transmitter and receiver share the key so that the information can be recovered. In a chaotic communication system, a transmitter that generates a time-evolving chaotic waveform acts as a "dynamical key" to transform the information symbols. The information can be recovered with a receiver possessing the same dynamical key, *i.e.*, its configuration and parameter settings are matched to those of the transmitter. It is interesting to note that using a chaotic carrier to dynamically encode information does not preclude the use of more traditional digital encryption schemes as well. Dynamical encoding with a chaotic waveform can thus be considered an additional layer of encryption.

Two factors that are important to privacy considerations in chaotic communication systems are the dimensionality of the chaos and the effort required to obtain the necessary parameters for a matched receiver. Earlier work has shown that for certain chaotic communication techniques, particularly those involving additive masking of a message by a chaotic carrier, the message can be recovered from the transmitted signal by mathematically reconstructing the transmitter's chaotic attractor if the chaos is low dimensional [Short, 1994(a); Short, 1994(b); Perez & Cerdeira, 1995]. Higher dimensional signals, especially those involving hyperchaotic dynamics, are likely to provide improved security. The number of parameters that have to be matched for information recovery and the precision with which they must be matched are important aspects of receiver design. We will show how the configuration and operation of the receiver may be designed to make it more suitable for private communications. At this point we would like to emphasize that the security of communication techniques is a complex and involved issue. In the work reported here, we do not make any claims of secure communications. Indeed, we do not know of any systematic cryptographic approach that has been taken to examine the security of different chaotic communication systems. We regard this as a very important open problem for future analysis.

Most realizations of chaotic communications have occurred in electronic circuits that simulate the dynamics of simple model systems (Lorenz, Rössler, double scroll or Chua system, etc.), even for the case of hyperchaotic systems. Peng et al. [1996] theoretically examined the question of synchronization of hyperchaotic Rössler systems and showed that synchronization is successfully achieved over a wide parameter range by using a transmitted signal that is a linear combination of the original phase space

variables. Mensour and Longtin [1998] have studied the synchronization of hyperchaotic systems described by Mackey-Glass delay-differential equations, with their use for private communications.

Optical systems present a somewhat different situation; one often does not know a priori what the equations are that should be used to model the system. Rather, insight into the formulation of appropriate models must be gained through experimental observations of the system dynamics. We follow this approach throughout this paper. Our research into chaotic communications using optical systems began when we experimentally achieved chaotic synchronization of two mutually coupled Nd:YAG (neodymium doped yttrium aluminum garnet) lasers that were operated side by side in a single YAG crystal [Roy & Thornburg, 1994; Sugawara *et al.*, 1994]. We then proposed a scheme for digital communication with a transmitter laser unidirectionally coupled to a distant laser used as a receiver [Colet & Roy, 1994]. The chaotic dynamics for these systems is not high-dimensional [Alsing *et al.*, 1997], and we showed that the message could be recovered fairly easily by time-delay embedding of the signals, unless one introduced complex modulations to increase the dimensionality of the dynamics. The dynamics present in such lasers is also rather slow, on the microsecond time scale at best.

Our next step was to examine a laser system that would provide not only a high-dimensional dynamics, but also a much greater bandwidth and high speed for signal transmission and recovery. This led us to the study of erbium doped fiber ring lasers (EDFRL); we developed a simplified model for the operation of an EDFRL in [Williams *et al.*, 1997]. These lasers emit at 1.53 - 1.55 microns, the wavelength regime of choice for optical communications in fibers, which have minimum loss in this range. The

emission is broadband (covering many nanometers), and we found the dynamics present in this system to be extremely fast. We estimate the bandwidth of the light intensity fluctuations to be in the range of many gigahertz, but the bandwidth of our electronic detection equipment prevents direct observation of the higher frequencies.

Ring cavity optical systems with nonlinear elements, as pointed out by Ikeda and coworkers many years ago [Ikeda *et al.*, 1980; Ikeda & Matsumoto, 1987], can possess very high-dimensional chaos resulting from the operation of the intra-cavity nonlinear elements and time-delayed feedback. Depending on the setting of the operating parameters of the erbium doped fiber ring laser system, one can observe both low- and high-dimensional dynamics [Ikeda *et al.*, 1980]. Simulations of Ikeda type ring systems by Abarbanel and Kennel reveal dimensions of order twenty five or higher [Abarbanel & Kennel, 1998]; they have also numerically demonstrated the synchronization of two ring cavities via unidirectional coupling. The dimensionality of the chaos in our experiments has been analyzed from the measured data using a false-nearest-neighbors (FNN) algorithm [Abarbanel, 1996] and found to be of order 10 or higher. Erbium doped fiber ring lasers therefore simultaneously offer the advantages of high-dimensional dynamics and high-speed communications.

Very recently, we reported the first experiments on all-optical chaotic communication of 10 MHz square waves using erbium doped fiber lasers and amplifiers [VanWiggeren & Roy, 1998]. A very interesting experiment on chaotic communications was reported simultaneously by Goedgebuer and colleagues [1998], who used a hybrid electro-optic system to encode a 2 kHz sine wave in the chaotic wavelength fluctuations of a tunable semiconductor laser and then decoded the information with an

open-loop receiver. They also used a time-delay system [Larger *et al.*, 1998] to generate high-dimensional chaotic dynamics.

The experiments described in this paper more fully take advantage of the large bandwidth available in an EDFRL, demonstrating communication of return-to-zero (RZ) pseudo-random digital bits at rates of 125 Mb/s. Results from an experiment showing communication of a non-return-to-zero (NRZ) digital message at 250 Mbit/s are also discussed. Currently, the bit rate is limited by the bandwidth of our detection equipment. Though the high-dimensional dynamics of an EDFRL system offer the potential for privacy, we note that many of the experiments and techniques discussed in this paper are unlikely to be useful for private communications; rather, descriptions of those experiments are included because they both established and furthered our understanding. The more recent experiments described in this paper, however, do seem to offer the possibility for enhanced privacy in communication. A discussion of the privacy aspects of each method is included.

All of the communication experiments described in this paper use an EDFRL to generate chaotic waveforms and employ unidirectional coupling of the transmitter to the receiver. Each technique described utilizes an open-ring receiver designed to mimic the dynamics of light propagating once through the transmitter ring. The message to be communicated modifies the chaotic dynamics of the transmitter, and by comparing the output dynamics from the transmitter to the open-ring receiver dynamics, the message can be recovered. The message itself drives the chaotic dynamics of the transmitter. Thus, the manner in which the message is dynamically encoded is at least partly dependent on earlier portions of the message.

We took two distinct approaches in developing chaotic communication in EDFRLs. The first approach involves coupling an optical message signal from an external laser directly into the EDFRL. In the second approach, an intensity modulator is inserted within the ring laser itself to encode the message directly onto the chaotic carrier. A development of this technique incorporates two time-delays into the dynamics of the transmitter, making the information transmission more private.

A feature of all of these communication systems is that there is no encoding of symbols into unstable periodic orbits of the chaotic system, as has been proposed and demonstrated recently [Hayes *et al.*, 1993; Hayes *et al.* 1994]. Thus there is no loss of speed in communication that could occur through the use of higher order orbits for symbolic coding or transients to synchronization in closed-loop communication systems.

This paper is organized as follows. Section II contains a description of the experimental system used for message injection from an external tunable semiconductor laser system and dynamical encoding with a chaotic EDFRL. The technique used to recover the digital information is outlined. The results of experiments that use polarization or wavelength filters in the EDFRL are given in Section III.1(A) - III.1(C). These experiments enabled us to reduce the interference between message and chaotic lightwaves and revealed many features of the wavelength and polarization dynamics of the laser system. In section III.2(A) and III.2(B) the results of message injection experiments performed without any wavelength or polarization filters are given. The possibility of dynamical encoding and wavelength multiplexing are examined. Section IV contains a discussion of the privacy and consistency of information recovery of the message injection techniques.

A different approach for dynamical encoding with an intra-cavity modulator is described in Section V, and the results of these experiments are given in Section VI. No external laser for message injection is needed for this technique, and the encoded information is recovered by a division of signals in the receiver. A modified intra-cavity modulation technique that adds a second fiber loop (and hence a second time-delay) to significantly enhance the privacy of the information is presented in Section VII and the results are given in Section VIII. We show that information is dynamically encoded and consistently and clearly recovered at 125 Mbits/s (return-to-zero, or RZ format) or 250 Mbits/s (non-return-to-zero, or NRZ format) and examine the result of mismatch of receiver configuration or parameters. A discussion of the bit-error rate ($< 10^{-5}$) and results for communication through more than 35 km of fiber (including an eye-diagram) is given. Section IX contains a discussion of the modified intra-ring modulator technique including results of a false nearest neighbors estimate of the dimensionality of the chaotic dynamics for this technique. Section X concludes the paper with a brief recapitulation of goals and results. We finally mention some open questions that must be addressed before practical implementation of these ideas.

II. Experimental Setup and Operation Using Message Injection:

Several variations of the message injection approach are described first, but their general form is shown in Fig. 1. To create the optical message, light produced by an external-cavity tunable diode laser is amplitude modulated by a lithium niobate Mach-Zehnder interferometer to form a sequence of pseudo-random bits. After modulation, the lightwave is amplified in a controllable fashion by an erbium-doped fiber amplifier

(EDFA) with a 13 dBm maximum output power. This step governs the amplitude of the message injected into the EDFRL. The amplified message then passes through a polarization controller consisting of a series of waveplates ($\lambda/4$, $\lambda/2$, $\lambda/4$) arranged to permit complete control over the polarization state of the message as it is coupled into the ring.

The message light is injected into the EDFRL through a 90/10 waveguide coupler, which allows 10 percent of the message light to be injected into the ring, while retaining 90 percent of the light already in the ring. The light propagates to a 50/50 output coupler that sends half the light in the ring to the receiver unit, while the other half passes through EDFA. This EDFA has 17 dBm maximum output power and 30 dB small signal gain. The active (doped) fiber in the EDFA is 17 m long and is pumped by diode lasers with a 980 nm wavelength. After passing through the EDFA, the light then travels through a filter consisting of a polarization controller, again a series of waveplates, and either a polarizer or bandpass filter depending on the variation of the method being used. The total length of the active and passive fiber in the ring totals approximately 40 m, which corresponds to a round trip time for light in the ring of about 200 ns. Isolators in the EDFA ensure that light propagates unidirectionally in the ring, as indicated by Fig. 1. Unless otherwise specified in the descriptions of subsequent experiments, the transmitter EDFRL is operated at pump powers more than 10 times threshold. Typical optical powers in the ring are between 10-40 mW depending on the losses in the ring.

Light exiting the ring through the 50/50 output coupler propagates in an optical fiber to the receiver unit. Light entering the receiver unit is split at the 90/10 coupler. Ten percent passes through a variable attenuator that prevents photodiode A (125 MHz

bandwidth) from saturating. The other 90 percent of the light passes through EDFA 2 and another filter. EDFA 2 and the receiver filter are intended to be replicas of EDFA 1 and the filter in the transmitter so that the receiver can synchronize to the dynamics of the transmitter. After passing through EDFA 2 and the receiver filter, the light passes through an attenuator and is measured by photodiode B (125 MHz bandwidth). The signals from photodiodes A and B are recorded by a digital oscilloscope with a 1 GS/s sampling rate and 8-bit resolution.

A model for the EDFRL without message injection is given in [Williams *et al.*, 1997]. It consists of two delay equations for the two polarizations of the electric field and one differential equation for the population inversion. The functional forms of these equations, including message injection, are

$$\mathbf{E}_T(t) = f[\mathbf{E}_T(t - \tau_R), N(t), \mathbf{m}(t - \tau_R)] \quad (1)$$

and

$$\dot{N}(t) = g[\mathbf{E}_T(t), N(t)]. \quad (2)$$

f and g are nonlinear functions of the population inversion, $N(t)$, and the complex slowly varying envelope of the chaotic electric field in the transmitter, $\mathbf{E}_T(t)$. The message is represented as $\mathbf{m}(t)$, and the time it takes light to make a round trip in the EDFRL is τ_R . Eq. 1 shows that the electric field $\mathbf{E}_T(t)$ at any point in the cavity is functionally dependent on the electric field and message, $\mathbf{E}_T(t - \tau_R)$ and $\mathbf{m}(t - \tau_R)$, at that point one round trip earlier.

Conceptually, the method we use is similar to one described by Volkovskii and Rulkov [1993], but it has been modified to incorporate time-delays, optical phase, and polarization effects. The light that is transmitted from the EDFRL to the receiver unit is $s(t) = E_T(t) + m(t)$. If the injected message power is not too large (typically on the order of a few milliwatts or less), the message is “masked” by the larger (10-40 mW unless otherwise specified) chaotic intensity fluctuations. For simplicity, imagine that photodiode A detects its fraction of $s(t)$ at the same moment that the remaining fraction of $s(t)$ is incident at EDFA 2. The amplifier and filter then operate on the remaining fraction (~90%) of $s(t)$ to produce the waveform $E_R(t + \tau_R)$, which arrives at photodiode B with a time-delay equal to one round trip time in the transmitter, τ_R . At precisely this moment, photodiode A is detecting $s(t + \tau_R) = E_T(t + \tau_R) + m(t + \tau_R)$. Note that $E_T(t + \tau_R)$ is produced when EDFA 1 and the filter (in the EDFRL) operate on $s(t) = E_T(t) + m(t)$. Because EDFA 1 and the filter in the transmitter operate on light in the same way as EDFA 2 and the receiver filter, $E_R(t + \tau_R) = E_T(t + \tau_R)$. Mathematically, this occurs because f and g are the same in both systems, the systems have negative conditional Lyapunov exponents, and they display synchronization in a global sense [Abarbanel & Kennel, 1998]. The two photodiodes, therefore, measure the intensities $|E_T(t + \tau_R) + m(t + \tau_R)|^2$ and $|E_R(t + \tau_R)|^2$ respectively. The difference of these two measurements at any time is $2 \operatorname{Re}\{E_T^*(t + \tau_R) \cdot m(t + \tau_R)\} + |m(t + \tau_R)|^2$.

When no message is transmitted, it is clear from the preceding discussion that the transmitter and receiver should be synchronized. In other words, the two photodiodes should measure the same intensities, $|E_R(t + \tau_R)|^2 = |E_T(t + \tau_R)|^2$. The results of an

experiment in which no message was transmitted are shown in Fig. 2. Fig. 2A shows the signal from the transmitter with the laser operated far above threshold (greater than 10 times the pump power required for threshold). A time-delay embedding of the data in Fig. 2A is given in Fig. 2B; it shows that the chaos is not low-dimensional. Fig. 2C shows the signal recorded by photodiode B. The straight line shown in Fig. 2D demonstrates the synchronization of the light intensities as measured by photodiodes A and B. We used a numerical false-nearest-neighbors (FNN) algorithm [Abarbanel, 1996] in an attempt to estimate the dimensionality of the signal. The results are presented in Fig. 2E. The dimensionality of a time-series can be estimated by observing the dimension at which the percentage of false-nearest-neighbors goes to zero. Interestingly, we observe that for analysis of 250,000 points acquired at 1 GS/s, the FNN algorithm gives a dimension of 8. The limited bandwidth of our photodiodes does not allow measurement of the much higher frequencies that may be present in the real signal. Consequently, there may be additional attractor dimensions that do not manifest themselves in the data we obtain. Fig. 2E shows that the natural dynamics of the ring laser are not low-dimensional for the operating parameters used, even without the presence of an injected message to influence the dynamics of the ring laser.

III. Results for experiments using message injection

Two basic techniques using an injected optical message have been investigated. The first technique follows from the description above, but a generalized "filter" is used in both the transmitter and receiver units. Several variations of this technique are presented. The second technique is conceptually similar to the first, but no generalized filter is necessary.

III. 1(A)

In our first variant of this method, $m(t)$ is injected into the EDFRL with a polarization orthogonal to $E_T(t)$ but with the same wavelength. The polarization of the injected $m(t)$ is determined using the polarization controller in the message modulation unit. The filter in the EDFRL transmitter is a polarizer. The polarization controller and polarizer in the EDFRL are aligned such that the $m(t)$ in the EDFRL is "blocked" upon reaching the filter, while still allowing an orthogonally polarized $E_T(t)$ to pass through relatively unchanged. In this manner, $m(t)$ is prevented from circulating in the EDFRL and mixing with $E_T(t)$ on more than one pass through the EDFA, though it is transmitted to the receiver unit. The filter in the receiver unit is also aligned to prevent light polarized in the same direction as $m(t)$ from reaching photodiode B. Subtracting the signals at the photodiodes, as mentioned earlier, gives $2 \operatorname{Re}\{E_T^*(t) \cdot m(t)\} + |m(t)|^2$. The cross term is eliminated in this technique because $E_T(t)$ and $m(t)$ are orthogonally polarized. This leaves just $|m(t)|^2$ after subtraction.

Fig. 3 shows the results of an experiment using this technique. Fig. 3A is a time-trace of the transmitted signal, $s(t)$, as measured by photodiode A, and Fig. 3B is its power spectrum. No hint of the message can be discerned in the time-trace of the signal. The broadband nature of the transmitted signal is evident from the power spectrum. The spectrum's gradual decline with increasing frequency matches the spectral response of our photodiodes (125 MHz bandwidth) and results from this limitation. Fig 3C is a time trace of the signal measured by photodiode B, and its power spectrum is shown in Fig 3D. The power spectrum of the received signal lacks the smaller, fine peaks of the

transmitted signal. As can be seen in our next figure, those fine peaks are just the power spectrum of our repeating sequence of bits. Fig. 3E results from a subtraction of the waveform data in Fig. 3C from the data in Fig. 3A. The “random” bits are clear and match the 125 Mbit/s pattern used for this experiment:

11001101110110100100101111101010. Fig. 3F is the optical spectrum of the transmitted signal $s(t)$ showing that both $m(t)$ and $E_T(t)$ have the same wavelength, $\sim 1.532 \mu\text{m}$.

Fig. 4 is included as a measure of the accuracy of this technique. For comparison, Fig. 4A shows a segment of the message sequence as detected by photodiode A in the absence of chaos (EDFA 1 is turned off and $E_T(t) = 0$). Fig. 4B is simply the power spectrum of the entire recorded message sequence. Fig. 4C shows a portion of the message obtained through the chaotic subtraction. Clearly, the recovered message is degraded somewhat, probably due to imprecision in matching the polarization-based filters in both the transmitter and receiver. The power spectrum of the recovered message, a segment of which is shown in Fig. 4C, is shown in Fig. 4D. The peak corresponding to the 125 MHz bit-rate is evident in Fig. 4B.

III. 1(B)

In the preceding technique, the wavelengths of $m(t)$ and $E_T(t)$ were the same, but their polarizations were orthogonal. In this method, however, the wavelengths are different, but their polarizations are the same. The filter in the EDFRL again consists of the polarization controller followed by a polarizer. The polarization controller in the message modulation unit is adjusted so that the polarizations of $m(t)$ and $E_T(t)$ are parallel as they are transmitted from the EDFRL to the receiver unit. Again, the filter's

purpose in the EDFRL is to "block" light associated with $m(t)$ from continuing to circulate in the ring. A moment of explanation will be useful here.

$m(t)$ and $E_T(t)$ have the same polarization at the coupler where the message is injected. As the light propagates around the ring, the difference in wavelength, typically ~20 nm, results in a different output polarization state for light at the two wavelengths. We observe that this phenomenon of polarization dispersion occurs primarily in the erbium-doped fiber in the EDFA. At the filter, $m(t)$ is almost completely orthogonal to $E_T(t)$. Thus, $m(t)$ can be "blocked" by the polarizer while $E_T(t)$ continues to circulate. The method works as described above, but this time the cross-term averages to zero because $m(t)$ and $E_T(t)$ have different optical frequencies; once again, only $|m(t)|^2$ remains after subtraction of the two photodiode signals.

Fig 5A shows the signal transmitted from the EDFRL to the receiver unit as detected by photodiode A. Its power spectrum is shown in Fig 5B, and again, the spectrum is quite broadband. The signal recorded by photodiode B is shown in Fig 5C, and its corresponding power spectrum is given in Fig. 5D. Subtracting the two time-traces results in the trace displayed in Fig. 5E and shows excellent reproduction of the bits. Finally, Fig. 5F shows the optical spectrum of the transmitted signal, revealing a narrow peak corresponding to $m(t)$ at 1.532 μm and a broader peak corresponding to $E_T(t)$ at 1.555 μm .

III. 1(C)

Another method investigated was the use of bandpass filters rather than polarizers as filters. Once again, the purpose of the filters was to prevent light associated with $m(t)$ from continuing to circulate around the ring. The wavelength of the message light could

be adjusted to ~ 1 nm of the central wavelength of the filter and still be successfully "blocked". The filter in the receiver was tuned to match the filter in the transmitter. The electric field polarization, because no polarizer was in the ring, fluctuates very rapidly and effectively has no polarization, and consequently, the polarization state of the message is not important. Because the wavelengths of the message, $m(t)$, and the chaotic electric field, $E_T(t)$, are still substantially different, the cross-term in the subtraction of the photodiode signals averages to zero. Again, only $|m(t)|^2$ remains.

Fig. 6A shows the transmitted signal, $|s(t)|^2$, recorded at photodiode A. Its power spectrum is shown in Fig. 6B. The signal detected at photodiode B is shown in Fig. 6C, and its power spectrum is shown in Fig. 6D. Because the chaotic output has become almost periodic in this example, a comparison of Fig. 6A and Fig. 6C clearly shows the effect of the bits on the transmitted signal. However, it is still not at all obvious from observing just the transmitted signal that a message is included. A subtraction of the two signals is shown in Fig. 6E. The optical spectrum of the transmitted signal is supplied in Fig. 6F. The wavelength separation in this case is much smaller than in the previous case, and is approximately 1 nm.

III. 2(A)

The techniques discussed in section III. 1 all required the use of a filter and required that a distinction of polarization or wavelength be made between the chaotic electric field, $E_T(t)$, and the message signal, $m(t)$. The techniques presented in this section will demonstrate message communication without the use of filters and with the same wavelength for the message and chaotic electric field.

Time-traces from such an experiment are shown in Fig. 7A. In this example, both EDFA 1 and EDFA 2 are pumped by their diode pump lasers at 10 mW, a level slightly less than twice the threshold pump power for the ring laser. This pumping results in ~ -1 dBm optical power circulating in the ring when no message is being injected. The injected message has a power of ~ -4.5 dBm and a 1553.01 nm wavelength. The first panel, Fig. 7A, shows data taken from photodiode A (the thin line) and from photodiode B (the thick line). As explained earlier, a subtraction of the two signals is equal to $2 \operatorname{Re}\{E_T^*(t) \cdot m(t)\} + |m(t)|^2$. Fig. 7B shows that subtraction (thin line). For comparison, the thicker line in Fig. 7B is the message signal measured by photodiode A when the EDFRL is turned off to remove the chaotic masking. This is equivalent to measuring just $|m(t)|^2$. The greater amplitude of the “decoded” message is simply the result of the cross term $2 \operatorname{Re}\{E_T^*(t) \cdot m(t)\}$; in this case, the polarizations and phases of $E_T(t)$ and $m(t)$ (relevant in the cross term) have combined to improve the message reception. The fidelity is quite good. An optical spectrum of the transmitted light is shown in Fig. 7C. The message injection is strong enough that its optical frequency forces the EDFRL to have the same lasing frequency--1553.01 nm.

Fig. 8 provides power spectra for the transmitted signal (Fig. 8A) and for the signal at photodiode B (Fig. 8B); they have a very close resemblance. The narrowly spaced discrete spikes result from the repetitive 32-bit pattern used. The bit-rate was 125 Mbit/s; the corresponding spike is evident in both power spectra.

III. 2(B)

We also performed experiments with message injection at wavelengths which were not resonant with the lasing wavelength of the EDFRL. Fig 9A shows signals

measured by photodiodes A and B when the wavelength of the injected message is 1533.01 nm . In this case the EDFAs were pumped at about 85 mW, many times threshold. This resulted in an optical power in the ring of ~ 9.1 dBm without any message injection. The injected message power was ~ -3.1 dBm. The subtraction of the traces in Fig. 9A is seen in Fig. 9B. Once again, the same pattern of bits is obtained. The optical spectrum (Fig. 9C) shows two distinct peaks. The first of these peaks (1533 nm) corresponds to the message injection, whereas the second peak (1558 nm) corresponds to the natural lasing wavelength of the EDFRL. The very broad linewidth is characteristic of the EDFRL. The message light at 1533 nm stimulates the EDFRL to emit at the same wavelength and the fraction of the light that remains in the ring continues to circulate stimulating additional emission. Consequently, the light detected at 1533 nm consists of a combination of the message itself plus chaotic light produced by the EDFRL.

It was important to determine whether it would be possible simply to isolate the message wavelength (1533.01 nm) using a bandpass filter and observe the message directly. We performed that experiment and observed that the message was well obscured by the chaotic laser light. Fig. 10 shows one of these measurements. The sequence of bits is not visible even after isolating just the message wavelength. This experiment indicates that wavelength division multiplexing may be possible, while still using chaos to hide the information. In summary, the message wavelength can be varied around the natural lasing wavelength of the EDFRL and chaotic communication can still occur.

IV. Discussion of message injection approach

All of the variations demonstrated in section III. 1 were able to consistently recover a 125 Mbit/s digital message. Each variation uses a matched chaotic receiver to extract the message but the variations all have limitations in their ability to mask information. In section II. 1(A), the polarizations of $E_T(t)$ and $m(t)$ are orthogonal. At any point in the transmission channel they are both, in general, elliptically polarized. But by using a polarization controller, it is possible to change their polarization from elliptical to linear. Once that is accomplished, a properly oriented polarizer could remove the masking $E_T(t)$ leaving only $m(t)$. Varying the polarizations of $E_T(t)$ and $m(t)$ in time could make this unmasking more difficult.

In the experiment described in section III. 1(B), the wavelengths of the message and chaotic field are different, though they are polarized identically. Many optical devices exist to isolate particular wavelengths. Those devices could be used obtain the message without the masking. The technique described in III. 1(C) has the limitation that $m(t)$ and $E_T(t)$ are separated by ~ 1 nm in wavelength. The same wavelength dependent filters could possibly remove $E_T(t)$ without distorting $m(t)$ when III. 1(C) is used. This might be more difficult in III. 1(C) than in III. 1(B) as the wavelength separation is much smaller. To make isolating just the message wavelength more difficult, one could imagine a filter in the EDFRL itself which allows many wavelengths of $E_T(t)$ to be transmitted, thereby making it difficult to remove all of them without removing $m(t)$ as well. One could also imagine varying the wavelength of $m(t)$ or transmitting $m(t)$ as two or more wavelengths.

As stated earlier, chaotic communication does lend itself naturally to issues of encryption and privacy. From that perspective, the techniques of section III. 2 are probably to be preferred. But this method, too, has some limitations. Principally, we were unable to control the phase relationship of the electric field and the message field. Consequently, the cross-term, $2 \operatorname{Re}\{\mathbf{E}_T^*(t) \cdot \mathbf{m}(t)\}$, had to be minimized for more consistent message recovery. Without a filter, this meant that $\mathbf{E}_T(t)$ had to be kept as small as possible. The low pump powers used in section III. 2(A) were chosen for that reason. Even so, the message recovery was not consistent. This inconsistency became a greater problem as the pump power in EDFA 1 was increased or as the wavelength of the injected message light came closer to the resonant lasing wavelength of the EDFRL. In section III. 2(B), the message wavelength was separated from the EDFRL's natural lasing line. In this regime, larger pump powers in EDFA 1 could be used before the interference term mentioned earlier becomes too large for reasonably consistent message recovery.

V. Experimental Setup and Operation Using an Intra-ring Intensity Modulator

In the experiments described earlier, consistent message recovery is difficult to achieve because of interference effects between the chaotic light in the ring and the injected optical message. Without a filter, the interference term, $2 \operatorname{Re}\{\mathbf{E}_T^*(t) \cdot \mathbf{m}(t)\}$, fluctuates due to changing relative phase and polarization between $\mathbf{E}_T(t)$ and $\mathbf{m}(t)$. A new approach is taken to overcome this difficulty. In this approach, the message is applied directly to the chaotic light in the EDFRL using an electro-optic modulator located within the EDFRL. The message, in this approach, is a modulation rather than an

injected lightwave; consequently, the message does not interfere with the chaotic electric field in the EDFRL.

Fig. 11 shows a transmitter consisting of an EDFRL and a LiNbO_3 intensity modulator. The erbium-doped fiber amplifier (EDFA) has a small signal gain of ~ 30 dB and a maximum output power of 17 dBm. Its erbium-doped fiber is the active medium for the ring laser. As before, the intensity modulator uses a waveguide Mach-Zehnder interferometer as the basis for its operation. The modulator also acts as a polarizer because its waveguides are polarizing. A 90/10 output coupler directs 10 percent of the light out of the ring and into the communication channel. The remaining 90 percent of the light continues to circulate around the ring.

In the receiver, the light is split again. The transmitted signal is directly measured at photodiode A. The remaining light passes through a variable time-delay device. A precision time-delay is achieved using a GRIN (graded index) lens to couple light from a fiber into free-space. The light traverses a distance, the source of the variable time-delay, before it is incident on another GRIN lens coupler which couples the light from free-space into fiber. By controlling the separation between the two GRIN lens couplers, the time-delay between photodiodes A and B can be precisely controlled. For this experiment, photodiode B measures the same signal as photodiode A, but with a time-delay matched to within 0.1 ns of the round trip time of the EDFRL, τ_R .

The slowly varying envelope of the chaotic lightwave after the EDFA in the receiver can be represented as E . The lightwave propagates through the ring and is amplitude modulated as it passes through the modulator to create $m(t)E$, where $m(t)$ is the message signal. Note that in this case, the message, $m(t)$ is a scalar modulation rather

than a vector lightwave as in the previous experiments. Ninety percent of this light continues until it is amplified in the EDFA to create $E' \equiv m(t)E$, while the remaining fraction is output to the receiver. The lightwave exiting the amplifier has a significantly greater intensity, but its waveform is very similar to the input wave. For simplicity, we write for the lightwave after the amplifier $E' \equiv m(t)E$ because the relative amplitudes of E' and $m(t)E$ are not as important to the operation as is the shape of the waveform. The shape of the waveform is only slightly distorted in passing through the amplifier due to noise and nonlinearities in the amplification. E' also circulates through the ring and is modulated to produce $m(t + \tau_R)E'$, and a fraction is output to the receiver.

In the receiver, photodiode B is delayed relative to photodiode A by one round trip time, τ_R , to within an accuracy of ~ 0.1 ns. Consequently, when photodiode A is measuring $m(t + \tau_R)E'$, photodiode B is measuring $m(t)E$. Since $E' \equiv m(t)E$, a division of the signal recorded at photodiode A by the signal recorded at photodiode B should give $m(t + \tau)$, thereby recovering the message from the chaotic carrier.

VI. Results of Intra-Ring approach

Fig. 12 gives results of such an experiment. A repeating digital message with a 32 bit length was applied to the modulator in the ring. The message had the pattern: 01111101010110011011101101001001. The recovered message shown in Fig. 12E replicates this pattern. Figs. 12A and 12C, however, show no sign of the message. The power-spectra of the two measured signals (Figs. 12B and 12D respectively) show many peaks; the peak at 125 MHz corresponds to the bit-rate. That peak is also visible in the power spectrum of the recovered message bits, Fig. 12F.

Only a small message modulation was used to obtain Fig. 12; the depth of message modulation that could be used is limited by the dynamics of the ring laser. If the message modulation is too small, bit recovery is impaired because the noise may be larger in amplitude than the communicated message. If the message modulation amplitude is too large, it drives the laser into an unstable spiking regime. In that spiking regime, the transmitted intensities are near zero much of the time. Because our message is recovered through a division process, any noise present in the signal detected by photodiode B when the signal is near zero has very detrimental effects. Longer sequences of pseudorandom bits tended to require even smaller modulation amplitudes to prevent the spiking behavior than employed in Fig. 12.

Once an appropriate adjustment has been made, the message recovery is very consistent because, unlike in the earlier experiments, no interference term exists to distort message recovery. The intra-ring modulator method also has additional privacy benefits when compared with the techniques described in section III 1. In this method, the message is incorporated as a part of the chaotic carrier lightwave, $m(t)E$. Consequently, the message cannot be separated from the chaotic electric field using optical devices such as polarizers or bandpass filters.

As mentioned earlier, two additional factors that are important to privacy considerations are the dimensionality of the transmitted chaotic lightwave, and the effort required to obtain the necessary parameters for message recovery. The signal from the transmitter EDFRL has been analyzed using a false nearest neighbors algorithm [Abarbanel 1996]. Using 100,000 data points, the analysis indicates that the dimensionality is high, of order 10 or greater.

We have observed that only one parameter must be known in order to construct a receiver capable of recovering the message. Precise knowledge of the round-trip time, τ_R , of the EDFRL is sufficient for message recovery. Though the nonlinear dynamics of the coupled light field and population inversion in the EDFA of the transmitter result in chaotic fluctuations of light intensity, the EDFA does not significantly alter a waveform's shape after just one pass through the amplifier. Consequently, an EDFA in the receiver matched to the EDFA in the transmitter is not actually necessary to recover the message. Having only one parameter, τ_R , to be matched limits the potential privacy of the communication method. The same reasoning can be applied to the methods described in section III. There, too, the matched EDFA is unnecessary, though it was included in the experiments.

VII. Modified Intra-ring Method

A new configuration that requires multiple matched parameters in the receiver and allows consistent and clear message communication is shown in Fig. 13. An additional outer-loop is added to the solitary EDFRL in the previous system. The outer-loop extracts a portion of the light in the inner-ring, delays it relative to the light in the inner ring, and reinjects it. With just a small amount of reinjected light, the spiking behavior observed with larger modulation amplitudes in the previous experiment is eliminated. The transmitter also becomes more stable. Unlike the consistently chaotic output of the previous experiment, the transmitter is now only intermittently chaotic without message modulation.

The outer loop in the transmitter consists of a variable time delay, another EDFA, and a polarization controller. It is approximately 34 m in length, while the inner-ring is approximately 42 m long. The variable time delay is created using a pair of Graded Index (GRIN) collimating lenses separated by an adjustable free-space distance. One GRIN lens couples light from the optical fiber into air, and the other GRIN lens couples the light back into the fiber. The EDFA in the outer loop is used to control the relative amplitude of the light that is sent back into the inner ring. The polarization controller is used to change the relative polarization and phase between light in the outer-loop and light in the inner-ring.

The outer loop in the receiver system has the same length as the outer loop in the transmitter system. Its EDFA and polarization controller have the same function as their counterparts in the transmitter. An additional variable time delay has been introduced into the receiver's main-line to match the time delay between photodiodes A and B to the round trip time of the inner ring of the transmitter.

The slowly varying envelope of the chaotic lightwave in the transmitter, just after EDFA 1, can be represented as E_T . The lightwave is split upon reaching the 90/10 coupler with ten percent sent into the outer loop and ninety percent remaining in the inner ring. At the 50/50 coupler, the light in outer loop is added to the light in the inner ring giving $E_{Tin} + E_{Tout}$. The sum passes through the modulator and exits as $m(t)(E_{Tin} + E_{Tout})$. Ten percent of this signal is output to the communication channel. The remaining ninety percent continues to circulate in the transmitter. It passes through EDFA 1 and is amplified to produce $E'_T \equiv m(t)(E_{Tin} + E_{Tout})$ --again, we disregard the amplification for simplicity, and instead focus on the shape of the envelope. E'_T

propagates as above through the transmitter, ultimately sending $m(t + \tau)(\mathbf{E}'_{Tin} + \mathbf{E}'_{Tout})$ to the communication channel, where τ is the round trip time for light in the inner ring.

In the receiver, the transmitted signal is divided as before between photodiode A and photodiode B. Photodiode A measures the transmitted signal directly. Light sent toward photodiode B is split and recombined in such a way as to recreate the dynamics of the transmitter. The length of the outer loop in the receiver has been matched in length to the outer loop of the transmitter. The transmitted lightwave $\mathbf{E}'_R = m(t)(\mathbf{E}_{Tin} + \mathbf{E}_{Tout})$ is split and recombined to become $\mathbf{E}'_{Rin} + \mathbf{E}'_{Rout}$. Experimentally, the length of the outer loop in the receiver is matched to an accuracy of ± 3 cm. Thus,

$|\mathbf{E}_{Rin}| \equiv |\mathbf{E}_{Tin}|$ and $|\mathbf{E}_{Rout}| \equiv |\mathbf{E}_{Tout}|$, but the relative optical phase between \mathbf{E}_{Rin} and \mathbf{E}_{Rout} is uncorrelated to the relative phase of \mathbf{E}_{Tin} and \mathbf{E}_{Tout} . The time delay between photodiode A and photodiode B has also been matched to an accuracy of 0.1 ns.

Recovering the message is accomplished by dividing the signal measured at photodiode A by the signal measured at photodiode B. The time-delay between photodiode A and photodiode B has been adjusted to ensure that photodiode A measures the intensity

$$\begin{aligned} |m(t + \tau_R)(\mathbf{E}_{Tin} + \mathbf{E}_{Tout})|^2 = \\ |m(t + \tau_R)|^2 (|\mathbf{E}_{Tin}|^2 + |\mathbf{E}_{Tout}|^2 + 2|\mathbf{E}_{Tin}||\mathbf{E}_{Tout}|\cos\theta_T\cos\phi_T), \end{aligned} \quad (3)$$

while at the same time, photodiode B measures

$$|(\mathbf{E}_{Rin} + \mathbf{E}_{Rout})|^2 = (|\mathbf{E}_{Rin}|^2 + |\mathbf{E}_{Rout}|^2 + 2|\mathbf{E}_{Rin}||\mathbf{E}_{Rout}|\cos\theta_R\cos\phi_R). \quad (4)$$

$\theta_{R,T}$ and $\phi_{R,T}$ are the relative polarization angle and relative phase angle between $\mathbf{E}_{R,Tin}$ and $\mathbf{E}_{R,Tout}$ respectively. If $\cos\theta_T\cos\phi_T = \cos\theta_R\cos\phi_R$, a simple division obviously gives $|m(t + \tau_R)|^2$. However, we have already explained that the relative phase in the receiver, ϕ_R , is not correlated with the relative phase in the transmitter, ϕ_T . An inherent property of the transmitter allows this problem to be overcome.

The transmitter consists of two coupled erbium doped fiber ring lasers. One of the ring lasers is the inner ring. The second ring laser is formed by the perimeter of the transmitter including the outer loop. The two lasers have limited flexibility to adjust their lasing modes to maximize the intensity that passes through the modulator. The optimized laser modes possess a fixed value for $\cos\theta_T\cos\phi_T$ when they are recombined. Although $\cos\theta_T\cos\phi_T = 1$ maximizes the intensity when the lightwaves from the inner ring and outer loop are recombined, that particular polarization and phase relationship may not be optimal for passing through the modulator, which also acts as a polarizer. The fixed value $\cos\theta_T\cos\phi_T$ that results from optimization can be altered by adjustment of the polarization controller in the outer loop. Using the polarization controller in this way, initial observations suggest rough values for $\cos\theta_T\cos\phi_T$ as low as ~ 0.3 , or as high as 1.

Although the value of $\cos\theta_T\cos\phi_T$ is relatively stable, the transmitter's lasing wavelength fluctuates on a time scale of ~ 5 ms. In the receiver unit, the wavelength fluctuation ensures that $\cos\theta_R\cos\phi_R$ also fluctuates. The polarization controller in the outer loop can fix the value of $\cos\theta_R$ to any value, but the relative phase angle, ϕ_R , is

free to fluctuate as the wavelength changes. Unlike the transmitter, the receiver has no feedback mechanism to fix ϕ_R . Figure 14 shows two 100 ms time traces of signals detected by photodiode A and photodiode B. The transmitter was unmodulated during this experiment. The transmitted signal, because $\cos \theta_T \cos \phi_T$ is fairly constant, shows very little variation in amplitude. In contrast, the receiver signal makes significant jumps corresponding to fluctuations of ϕ_R due to changing wavelength in the transmitted signal. The relative phase angle between lightwaves in the main-line and outer loop of the receiver changes if the wavelength of those lightwaves changes. A close examination of the figure shows that the amplitude of the transmitted signal also changes slightly at each of these wavelength changes.

If $\cos \theta_R$ is set to 0 using the polarization controller, the fluctuations of ϕ_R do not affect the intensity. With this setting for $\cos \theta_R$, message recovery is consistent even when $\cos \theta_T \cos \phi_T \neq 0$. This somewhat surprising result can be understood by observing that $|\mathbf{E}_{Tin}| |\mathbf{E}_{Tout}|$ as a function of time very closely resembles the function $|\mathbf{E}_{Tin}|^2 + |\mathbf{E}_{Tout}|^2$. To observe this using experimental data, light from the main-line and outer loop in the receiver were directed into photodiodes rather than combined in a coupler. The relative lengths of the arms was the same as for the experiment (again ± 3 cm). One photodiode (main-line) measured $|\mathbf{E}'_{Rin}|^2$ while the other photodiode (outer-loop) measured $|\mathbf{E}'_{Rout}|^2$. This data allows us to calculate $|\mathbf{E}_{Rin}|^2 + |\mathbf{E}_{Rout}|^2 + 2|\mathbf{E}_{Rin}| |\mathbf{E}_{Rout}|$ and present its time-series in Fig. 15A. Fig. 15B shows a time-series corresponding to $2[|\mathbf{E}_{Rin}|^2 + |\mathbf{E}_{Rout}|^2]$.

To obtain an estimate for the magnitude of the message recovery errors produced by having $\cos \theta_R = 0$, we divide the time-series $|\mathbf{E}_{Rin}|^2 + |\mathbf{E}_{Rout}|^2 + 2|\mathbf{E}_{Rin}| |\mathbf{E}_{Rout}|$

(maximizing the cross-term in (3), setting $m(t + \tau) = 1$, and using the approximation $|E_{Rin,out}| \approx |E_{Tin,out}|$) by the time-series corresponding to $2[|E_{Rin}|^2 + |E_{Rout}|^2]$ (proportional to (4) when $\cos \theta_R = 0$). The result is shown in Fig. 15C. Any deviation from a value of 1 is a message recovery error resulting from the zero cross-term in the denominator. A comparison of the magnitude of these errors to the amplitude of a typical digital message (as shown in Figs. 16-19) shows that they are small enough that message reception is not impaired even when the cross-term is maximized in (3), as in this case.

VIII. Results of the Modified Intra-ring Method

Results from this technique, using a communication channel ~ 4 m in length, are shown in Fig. 16. A message consisting of pseudorandom sequence of 100,000 bits at 125 Mbit/s was communicated in this experiment. Fig. 16A shows 400 ns of the signal transmitted through the communication to the receiver and detected at photodiode A. Fig. 16C shows the signal simultaneously detected by photodiode B. Fig. 16E shows the division of the signal shown in Fig. 16A by the signal in Fig. 16B. The recovered bits are clear in Fig. 16E, but they are indiscernible in Figs. 16A and 16C. The power spectra of the signals are shown in the panels on the right. Fig. 16B shows the power spectra of the signal shown in Fig. 16A. The 125 MHz frequency peak, corresponding to the bit-rate, appears as just one of many small peaks in the spectrum. The same is true for the power spectra of the signal recorded by photodiode B, shown in Fig. 16D. Finally, Fig. 16F shows the power spectra of the recovered bits. Only one peak, at 125 MHz, is significant.

Initial tests show very consistent recovery of the data. Bit-error-rates of $<10^{-5}$ are routinely achieved. The BER may be significantly lower, but memory limitations on

our digital oscilloscope limit the number of message bits that can be acquired for analysis. Occasionally, however, the transmitter "bursts" into an unstable, high frequency chaos. The amplitude and frequency of these bursts can be greatly diminished by limiting back-reflection from the open leads of the waveguide couplers. Environmental vibrations such as tapping on the table seem to induce bursting as well. During these intermittent bursts, the BER can be much higher, though in most instances, the error produced is small enough that message recovery is not impaired at all.

In order to recover the communicated message, the receiver must be "tuned" to the dynamics of the transmitter. This requires matching certain transmitter parameters in the receiver. In this system, the configuration, time-delays, and relative amplitudes for the lightwaves in the main-line and outer loop must be properly matched in order to recover the message. Fig. 17 shows the effect of various parameter mismatches.

Fig. 17A shows successful recovery of a repeating pseudorandom 40-bit message sequence at 125 Mbit/s using the same experimental parameters as used to obtain the data for Fig. 16. The proper sequence is clearly recovered. The other panels represent attempted recovery of this message with just one parameter mismatched. Fig 17B shows an attempted recovery of the same message, but without using the outer loop in the receiver. The message is very distorted. Fig. 17C shows recovery without the main-line part of the receiver. Again, the message is greatly distorted. Fig. 17D shows recovery of the message with an outer loop that is one meter too long. When the time-delay between photodiode A and photodiode B is incorrect by just 1 ns (8 inches of optical fiber) the message is also severely distorted, as shown in Fig. 17E. Fig. 17F demonstrates that the relative power levels of E_{Rin} and E_{Rout} must be properly set in order to accurately recover

the message. For Fig. 17F, the pump power on EDFA 3 was adjusted from its optimal setting of 21 mW (used to produce the data shown in Fig. 16) to 100 mW.

To determine this method's viability as a communication scheme, it is also important to investigate the effect of long communication channels on the technique. With this in mind, an experiment was performed using a communication channel consisting of another EDFA (to compensate for channel losses) followed by 35 km of ordinary single mode fiber. As in Fig. 16, a repeating message consisting of a sequence of 100,000 pseudorandom bits at 125 Mbit/s are communicated. Fig. 18A shows the transmitted signal as recorded at photodiode A after passage through the longer channel. Its power-spectrum is shown in Fig. 18B. Fig. 18C shows the signal measured by photodiode B. Its power-spectrum is shown in Fig. 18D. The power spectra of the signals measured by the photodiodes show peaks at 125 MHz corresponding to the 125 Mbit/s bit-rate, but these peaks are not obviously conspicuous. Fig. 18E shows the recovered message. The message does not reveal any significant distortion caused by the long communication channel. Fig. 18F gives the power-spectrum of the message.

The bit-rate in all of these experiments is limited by the bandwidth of the photodiodes (125 MHz 3-dB roll-off), but a doubled bit-rate can be obtained without introducing higher frequencies components by using a non-return-to-zero (NRZ) communication scheme rather than the return-to-zero (RZ) communication used thus far. Fig. 19 shows results for communication of an NRZ 100,000 bit pseudorandom sequence at a rate of 250 Mbit/s. The communication channel for this experiment consisted of an EDFA and 38 km of dispersion-shifted (dispersion zero at 1550 nm) fiber. Fig. 19A shows the transmitted signal measured by photodiode A. Fig. 19B shows its power-

spectrum. Fig. 19C shows the signal measured by photodiode B, and Fig. 19D shows its power-spectrum. Fig. 19E shows recovery of the 250 Mbit/s NRZ message. The message's power spectrum is shown in Fig. 19F.

An eye-diagram illustrating the quality of this communication is shown in Fig. 20. The eye is open indicating accurate recovery of the 250 Mbit/s signal. The slope of the lines around the eye result from the slew-rate of the photodiodes.

IX. Discussion of the Modified Intra-ring Method

We have demonstrated consistent and clear optical chaotic communication using a modulator in the transmitter to encode the message. Bit-rates of 125 Mbit/s and 250 Mbit/s were demonstrated. Taking full advantage of the large bandwidth available in the optical system would permit even faster rates, but these experiments were limited by the bandwidth of our photodiodes (125 MHz 3-dB roll-off) and oscilloscope (1 GS/s). The method works well even over long communication channels (~35 km), and in both ordinary and dispersion-shifted fibers.

It also offers enhanced privacy compared to the other methods discussed in this paper. As shown in Fig. 17, accurate recovery of the message requires multiple matched parameters in the receiver. The geometrical configuration of the receiver must be the same as in the transmitter. The lengths of the fiber in the outer loop and the time-delay between photodiode A and B must be matched fairly precisely. Finally, the relative power levels of E_{Rin} and E_{Rout} must be properly matched to the power levels in the transmitter. This method suggests that more complicated geometries and systems requiring additional parameters for message recovery may also be possible to construct using an EDFRL as a basic element.

Another privacy consideration is dimensionality. As mentioned earlier in this paper, it has proved possible to recover a message from certain lower-dimensional (3 dimensional) chaotic communication systems [Short, 1994(a); Short, 1994(b); Perez & Cerdeira, 1995]. A communication method utilizing higher dimensional chaos is likely to provide enhanced privacy. The transmitted signals produced in this experiment, as seen in Fig. 16, have also been analyzed using a false-nearest-neighbors algorithm [Abarbanel, 1996]. Using 100,000 points acquired at 1 GS/s, the algorithm indicated that the dimensionality of the attractor is of order 10 or higher, as seen in Fig. 21. This figure can be compared to the false nearest neighbors data (Fig. 2) for the transmitted light from an unmodulated EDFRL. The increase in the dimensionality can probably be attributed to the fact that the pseudorandom message modulation drives the chaotic dynamics of the transmitter in this experiment. The nonlinear operation of the transmitter transforms the digital message into a high-dimensional chaotic waveform. The shape of the chaotic carrier waveform at any time is a nonlinear time-delayed function of the previous digital message bits.

X. Conclusion

The experiments described in this paper trace the development of several techniques for dynamical coding and cryptography using time-delayed optical systems. Our goal has been to introduce the use of time-delayed systems for all-optical chaotic communication at high speeds through standard single-mode optical fiber, using erbium doped fiber ring lasers at 1.5 microns. Our demonstrations include communication at up to 250 Mbits/s through 35 km of single-mode fiber. These results are limited at present only by the speed of the detection electronics and not by the bandwidths or dynamics of

the optical systems. We hope to stimulate theoretical and experimental studies of dynamical encoding and decoding with time-delayed systems.

There remain many open questions to be answered regarding the information theoretic aspects of the dynamical encoding and cryptographic processes outlined here. Estimates of channel capacity and bit-error rates, robustness of the methods against noise and the development of error control and correction methods are all topics that need to be addressed before such systems find practical applications in the real world. Finally, as we have mentioned earlier, the question of security of chaotic communication techniques is an important one that needs to be addressed by the proper cryptographic methods of analysis. We hope our paper will stimulate research in these new and fertile areas.

Acknowledgements: We thank Henry Abarbanel, Matt Kennel, Steve Strogatz, N. Johnson and all others (at UCSD, Cornell, and Georgia Tech) involved in our collaboration, through National Science Foundation grant NCR961225, for helpful discussions. We gratefully acknowledge support from the Office of Naval Research, and thank C. Verber, P. Juodawlkis, M. Gross, and Q. Williams for providing essential instrumentation and encouragement.

References

- Abarbanel, H.D.I. & Linsay, P.S. [1993] "Secure communications and unstable periodic orbits of strange attractors," *IEEE Trans. on Circuits and Systems II: Analog and Digital Signal Processing* 40, 643-645.
- Abarbanel, H.D. I. [1996] Analysis of observed chaotic data (New York, Springer-Verlag).
- Abarbanel, H.D.I. & Kennel, M.B. [1998] "Synchronizing high-dimensional chaotic optical ring dynamics *Phys. Rev. Lett.* 80, 3153 - 3156.
- Alsing, P.M., Gavrielides, A., Kovanis, V., Roy, R. & Thornburg Jr., K.S. [1997] "Encoding and decoding messages with chaotic lasers," *Phys. Rev. E* 56, 6302 - 6310.
- Boccaletti, S., Farini, A. & Arecchi, F.T. [1997] "Adaptive synchronization of chaos for secure communication," *Phys. Rev. E* 55, 4979 - 4981.
- Colet, P. & Roy, R. [1994] "Digital communications with synchronized chaotic lasers," *Opt. Lett.* 19, 2056 - 2058.
- Cuomo, K.M. & Oppenheim, A.V. [1993] "Circuit Implementation of Synchronized Chaos with applications to communications," *Phys. Rev. Lett.* 71, 65 - 68.
- Cuomo, K.M., Oppenheim, A.V. & Strogatz, S.H. [1993] "Robustness and signal recovery in synchronized chaotic system," *Int. Jour. Bif. and Chaos* 3, 1629-1638.
- Ditto, W.L. & Pecora, L.M. [1993] "Mastering Chaos," *Sci. Am.* 269, 62 -68.
- Goedgebuer, J-P., Larger, L. & Porte, H. [1998] "Optical cryptosystem based on synchronization of hyperchaos generated by a delayed feedback tunable laser diode," *Phys. Rev. Lett.* 80, 2249 - 2252.

- Hayes, S., Grebogi, C. & Ott, E. [1993] "Communicating with Chaos," *Phys. Rev. Lett.* **70**, 3031 - 3034.
- Hayes, S., Grebogi, C., Ott, E. & Mark, A. [1994] "Experimental control of chaos for communication," *Phys. Rev. Lett.* **73**, 1781 - 1784.
- Hellman, M.E. [1977] "An extension of the Shannon theory approach to cryptography," *IEEE Trans. Inf. Theory* **IT-23**, 289 - 294.
- Ikeda, K. & Matsumoto, K. [1987] "High-Dimensional chaotic behavior of systems with time-delayed feedback," *Physica D* **29**, 223 - 235.
- Ikeda, K., Daido, H. & Akimoto, O. [1980] "Optical turbulence: chaotic behavior of transmitted light from a ring cavity," *Phys. Rev. Lett.* **45**, 709 - 712.
- Larger, L., Goedgebuer, J-P. & Delorme, F. [1998] "Optical encryption system using hyperchaos generated by an optoelectronic wavelength oscillator," *Phys. Rev. E* **57**, 6618 - 6624.
- Mensour, B. & Longtin, A. [1998] "Synchronization of delay-differential equations with application to private communication," *Phys. Lett. A* **244**, 59 - 70.
- Mirasso, C.R., Colet, P. & Garcia-Fernandez, P. [1996] "Synchronization of chaotic semiconductor lasers: application to encoded communications," *IEEE Phot. Tech. Lett.* **8**, 299 - 301.
- Parlitz, U., Kocarev, L., Stojanovski, T. & Preckel, H. [1996] "Encoding messages using chaotic synchronization," *Phys. Rev. E* **53**, 4351 - 4361.
- Pecora, L.M. & Carroll, T.L. [1990] "Synchronization in chaotic systems," *Phys. Rev. Lett.* **64**, 821-823.

- Pecora, L.M. & Carroll, T.L. [1991] "Driving Systems with Chaotic Signals," Phys. Rev. A **44**, 2374 - 2383.
- Peng, J.H., Ding, E.J., Ding, M. & Yang, W. [1996] "Synchronizing hyperchaos with a scalar transmitted signal," Phys. Rev. Lett. **76**, 904 - 907.
- Perez, G. & Cerdeira, H. A. [1995] "Extracting messages masked by chaos," Phys. Rev. Lett. **74**, 1970 - 1973.
- Roy, R. & Thornburg Jr., K.S. [1994] "Experimental synchronization of chaotic lasers," Phys. Rev. Lett. **72**, 2009 - 2011.
- Shannon, C.E. [1949] "Communication theory of secrecy systems," Bell. Sys. Tech. Jour. **28**, 657 - 715.
- Short, K.M. [1994] "Steps towards unmasking chaotic communication," Int. Jour. Bif. and Chaos **4**, 959 - 977.
- Short, K.M. [1994] "Unmasking a chaotic communication scheme," Int. Jour. Bif. and Chaos **6**, 367 - 375.
- Strogatz, S.H. [1994] Nonlinear dynamics and chaos (Reading, Massachusetts, Addison-Wesley).
- Sugawara, T., Tachikawa, M., Tsukamoto, T., Shimizu, T. [1994] "Observation of synchronization in laser chaos," Phys. Rev. Lett, **72**, 3502 - 3505.
- VanWiggeren, G.D. & Roy, R. [1998] "Communicating with chaotic lasers," Science **279**, 1198 - 1200.
- Volkovskii, A.R. & Rulkov, N. [1993] "Synchronous chaotic response of a nonlinear oscillator system as a principle for the detection of the information component of chaos," Tech. Phys. Lett. **19**, 97 - 99.

Welsh, D. [1988] Codes and Cryptography (Oxford, Oxford).

Williams, Q.L., Garcia-Ojalvo, J. & Roy, R. [1997] "Fast intracavity polarization dynamics of an erbium-doped fiber ring laser: inclusion of stochastic effects," Phys. Rev. A **55**, 2376 - 2386.

Wu, C.W. & Chua, L.O. [1993] "A simple way to synchronize chaotic systems with applications to secure communication systems," Int. Jour. Bif. & Chaos **3**, 1619 - 1627.

Figure Captions

Figure 1: Experimental system for optical chaotic communication consisting of three parts. In the message modulation unit, cw laser light is intensity modulated to produce a message signal consisting of a series of digital bits. The message signal is injected into the transmitter where it is mixed with the chaotic lightwaves produced by the erbium-doped fiber ring laser. The message, now masked by the chaotic light, propagates through the communication channel to the receiver where the message is recovered from the chaos.

Figure 2: Fig. 2A shows the transmitted signal measured by photodiode A when no message is injected into the transmitter. Fig. 2B shows a time-delay-embedding plot of the data in Fig. 2A; the lack of structure indicates that the data is not low-dimensional. Fig. 2C shows the signal simultaneously detected by photodiode B. The signals recorded by the photodiodes are clearly synchronized, as shown in Fig. 2D. Fig. 2E gives the results of a false-nearest-neighbors analysis. It indicates a dimension of ~ 8 for the dynamics of the transmitted signal.

Figure 3: Fig. 3A shows the transmitted signal measured by photodiode A when a message is injected into the transmitter. Its power-spectrum can be seen in Fig. 3B. Fig. 3C shows the detected signal at photodiode B, and its power spectrum is also given by Fig. 3D. Subtracting the signals shown in Fig. 3A and Fig. 3C results in the recovered message shown in Fig. 3E. An optical spectrum is shown in Fig. 3F revealing a single

peak. Fig. 3F demonstrates that both the message and chaotic light share the same wavelength.

Figure 4: A comparison showing the quality of the message recovery. Fig. 4A shows a portion of the message directly detected at photodiode A when the ring laser is turned off, *i.e.* $E_T(t) = 0$. No chaotic encryption is used. The power-spectrum of the directly detected message is shown in Fig. 4B. The same message recovered from the chaotic transmitted signal, *i.e.* $E_T(t) \neq 0$, is shown in Fig. 4C. Fig. 4D shows the power spectrum of the recovered signal. The recovered message is somewhat degraded but still decipherable.

Figure 5: Fig. 5A shows the transmitted signal measure by photodiode A, while Fig 5C shows the signal measured simultaneously by photodiode B. Their power-spectra are given in Figs. 5B and 5D respectively. Again, subtraction of the two time-traces reveals the message, shown in Fig. 5E. An optical spectrum, Fig. 5F, shows that the message light and chaos have different wavelengths.

Figure 6: Figure 6A and 6C show simultaneous signals measured by photodiodes A and B respectively. Fig. 6A's power-spectrum is shown in Fig. 6B, and Fig. 6C's power-spectrum is given in Fig. 6D. Subtracting the signal shown in Fig. 6C from the signal shown in Fig. 6A gives the recovered message shown in Fig. 6E. In Fig. 6F, an optical spectrum shows that the wavelengths are not the same, but are much closer than they had been in the experiments performed for Fig. 5.

Figure 7: Fig. 7A shows both the transmitted signal measured by photodiode A (thin-line) and the signal measured by photodiode B (thick-line). The thick-line in Fig. 7B is the message signal directly detected by photodiode A when the transmitter ring-laser is turned off, and is included to verify that the message recovered from the chaos (thin-line) is indeed correct. An optical spectrum of the transmitted signal is shown in Fig. 7C to show that both the message and chaotic light have the same wavelength.

Figure 8: Power spectra corresponding to the signals measured in Fig. 7A. Fig. 8A is the power spectrum for the transmitted signal recorded at photodiode A. Fig. 8B shows the power spectrum for the signal measured by photodiode B.

Figure 9: Fig. 9A once again shows both the transmitted signal measured by photodiode A (thin-line) and the signal measured by photodiode B (thick-line). Fig. 9B shows the results of subtracting the thickline from the thin-line. Fig. 9C gives an optical spectrum showing the lasing wavelengths of the EDFRL. The message injection is occurring at a wavelength of $\sim 1.533 \mu\text{m}$.

Figure 10: The transmitted signal after passing through a 1 nm bandpass filter at $1.533 \mu\text{m}$. The chaotic light at this wavelength still masks the message.

Figure 11: Experimental setup for the intra-ring modulator approach. An intensity modulator is used to encode a digital message onto chaotic lightwaves produced by the erbium-doped fiber ring laser. Chaotic light from the ring travels to a receiver where a

precise time-delay between the photodiodes allows for the message to be recovered from the chaos..

Figure 12: Fig. 12A shows the signal from the transmitter as recorded by photodiode A. Fig. 12 C is the signal recorded by photodiode B in the receiver. A division of the two signals recovers the message as shown in Fig. 12E. Panels B, D, and F show the power spectra of the signals shown in A, C, and E respectively. Note that the 125 MHz peak in Figs. B and D is not the most prominent peak. In Fig. 12F, a peak at the bit-rate of 125 MHz is clearly visible.

Figure 13: Experimental setup of the improved intra-ring modulator approach. An erbium-doped fiber ring laser with an additional outer loop is used as a transmitter. Again, an intensity modulator is used to encode a digital message onto the chaotic optical carrier. The carrier and message propagate to a receiver constructed to reproduce the dynamics of the transmitter. Proper configuration, time-delays, and power levels in the receiver allow recovery of the message.

Figure 14: The more level signal is the transmitted signal detected by photodiode A when there is no intensity modulation in the transmitter. The fluctuating signal was detected by photodiode B. The fluctuations illustrate the very large effect that the fluctuating phase angle ϕ_R has on the signal measured at photodiode B. In the experiments, however, the polarization angle θ_R was adjusted to eliminate the effect of the ϕ_R fluctuations.

Figure 15: The error resulting from setting $\theta_R = 0$ in (4) when the crossterm in (3) is not equal to zero is shown to be small enough that it does not interfere with message recovery. Fig. 15A shows the time-series corresponding to $|E_{Rin}|^2 + |E_{Rout}|^2 + 2|E_{Rin}||E_{Rout}|$. Fig. 15B shows time-series data corresponding to $2(|E_{Rin}|^2 + |E_{Rout}|^2)$. Dividing the data in Fig. 15A by the data in Fig. 15B gives an estimate for the size of the error that results from eliminating the cross-term in (4) by setting $\theta_R = 0$. The result of that division is shown in Fig. 15C. Comparing Fig. 15C with Fig. 16E shows that such small errors will not hinder message recovery.

Figure 16: This figure shows successful recovery of a message signal from its chaotic carrier. The message signal consisted of a sequence of 100,000 pseudorandom bits transmitted at a rate of 125 Mbit/s. Fig. 16A shows the transmitted signal detected at photodiode A. Its power spectrum is shown in Fig. 16B. Note that a small peak is visible at 125 MHz corresponding to the bit-rate. The signal detected at photodiode B is shown in Fig. 16C. Its power spectrum is shown in Fig. 16D. Again, a small peak is visible at 125 MHz. the recovered message (formed by a division of the signals at photodiodes A and B) is shown in Fig. 16E. Fig. 16F shows the power spectrum of the recovered bit sequence, with a clear peak at 125 MHz. The message itself is not discernible in either of the signals shown in Figs. 16A and 16C, but the recovered message is very clear.

Figure 17: Recovery of the message requires that certain parameters in the transmitter be matched in the receiver. Fig. 17A shows recovery of the message with all appropriate parameters matched. The other panels show attempted recovery with just one mismatched parameter. Fig 17B shows attempted recovery with a geometrical configuration in the receiver that lacks the outer loop. In Fig. 17C, recovery is attempted without the main-line part of the receiver. An extra meter of optical fiber is used in the outer loop for the attempted recovery shown in Fig. 17D. Fig. 17E shows attempted recovery when the time-delay between photodiode A and B is mismatched by just 1 ns (± 20 cm of optical fiber). Fig. 17F shows recovery when the amplitude of E_{Rout} is too large when it is recombined with E_{Rin} .

Figure 18: Successful recovery of a message after propagation through 35 km of ordinary single-mode optical fiber. Fig. 18A shows the transmitted signal detected at photodiode A. The signals power spectrum is shown in Fig. 18B. A small peak at 125 MHz corresponding to the 125 Mbit/s bit-rate is visible. Fig. 18C shows the signal measured by photodiode B, and its power spectrum is seen in Fig. 18D. Fig. 18E shows the clearly recovered message. Its power spectrum is shown in Fig 18F.

Figure 19: Successful recovery of a non-return-to-zero (NRZ) message at 250 Mbit/s after propagation through a 38 km dispersion-shifted (1550 nm dispersion zero) fiber. the transmitted signal detected by photodiode A is shown in Fig. 19A. Fig. 19B shows the power-spectrum of the transmitted signal. No peaks are visible corresponding to the bit-rate of the message. Fig. 19C shows the signal recorded by photodiode B after passing

through the receiver. Its power spectrum is shown in Fig. 19D. The recovered message bits are shown in Fig. 19E. Their power spectrum is shown in Fig. 19F.

Figure 20: An eye-diagram showing the quality of the recovery of NRZ digital bits after propagation through 38 km of dispersion-shifted fiber. The eye-diagram is open, indicating good message recovery. The slew-rate of the photodiodes is evident in the slope of the intersecting lines. Clearly, the bit-rate is limited by the detection equipment.

Figure 21: False-nearest neighbors data showing the transmitted signal to be high-dimensional, of order 10 or greater. The high-dimensional nature of the chaos can be attributed to the fact that the pseudorandom message modulation signal drives the chaotic dynamics of the transmitter.

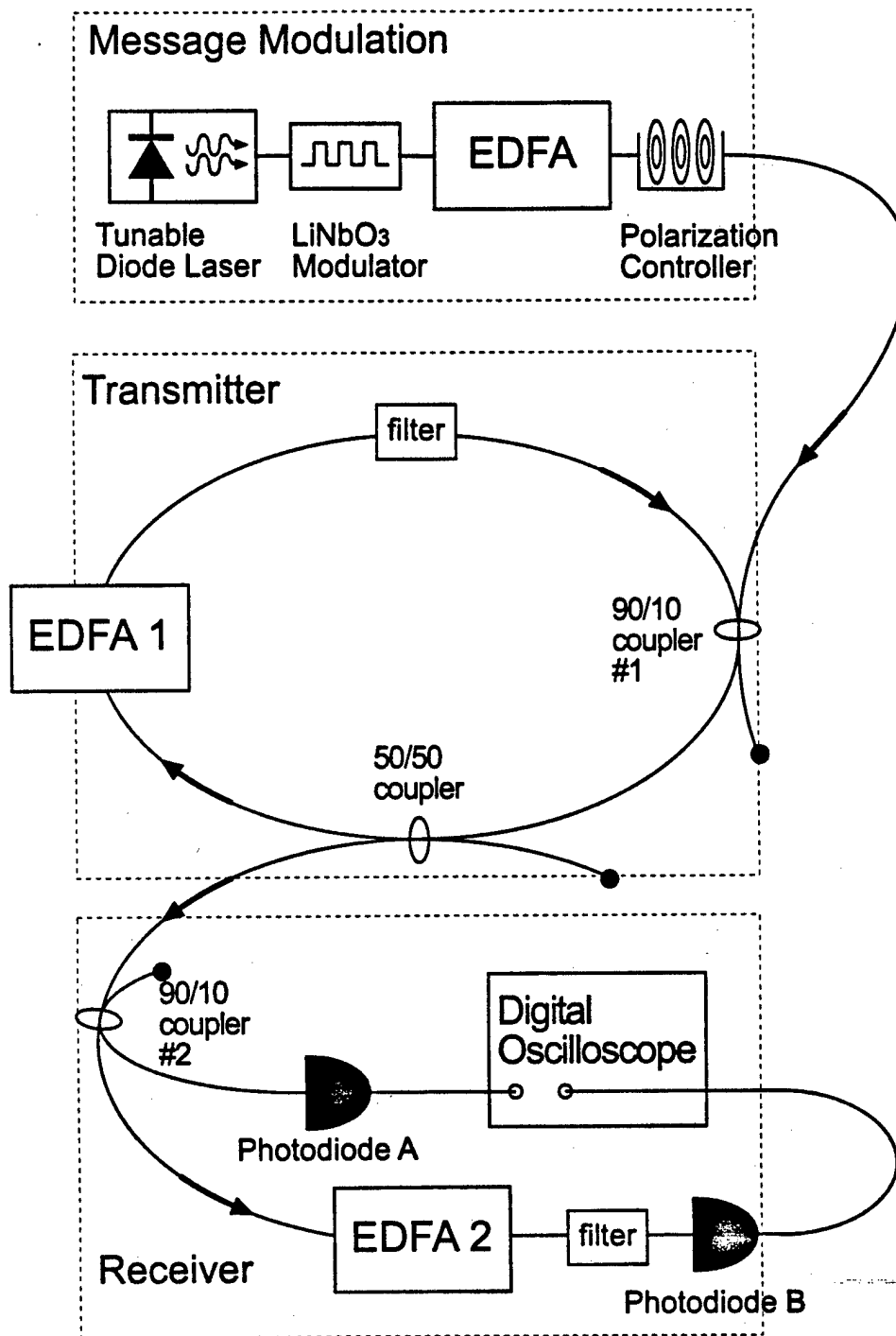
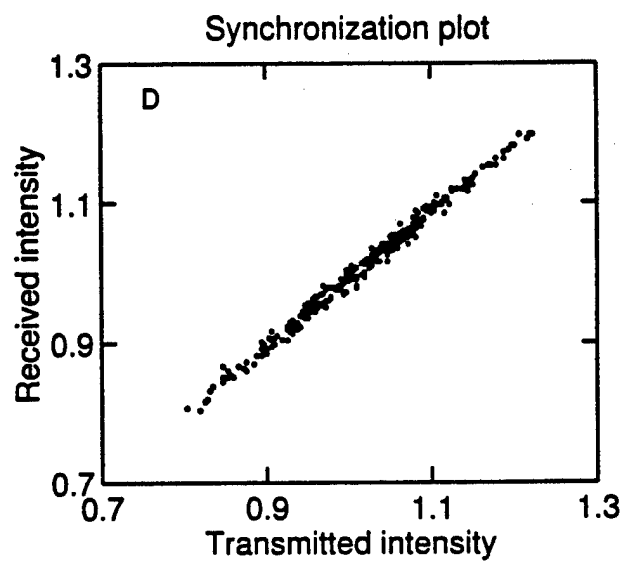
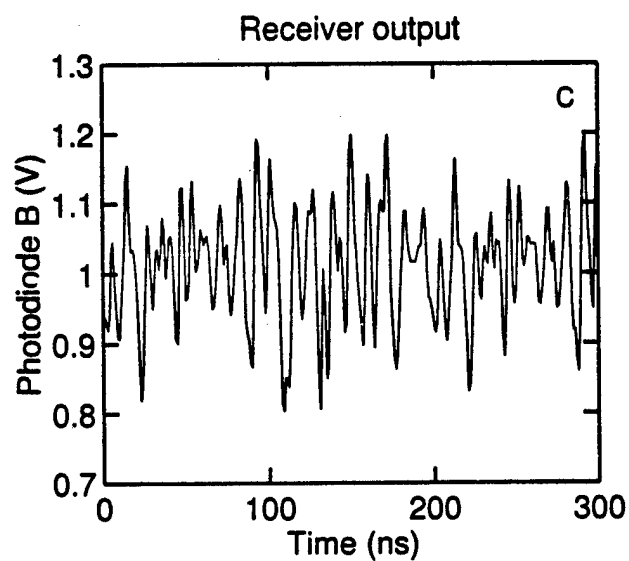
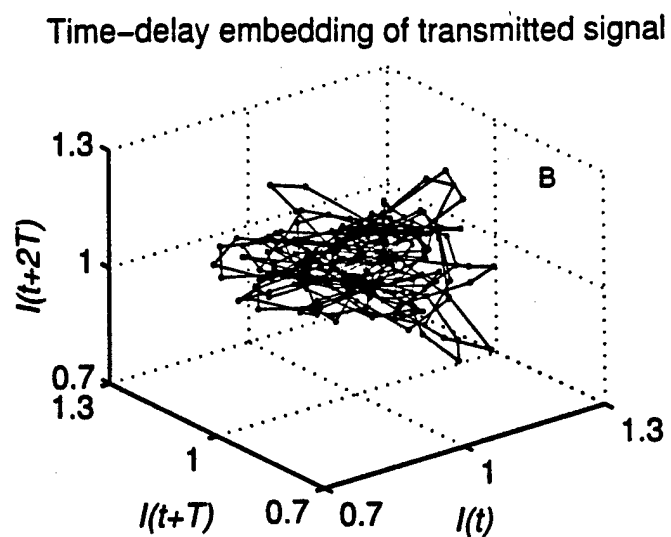
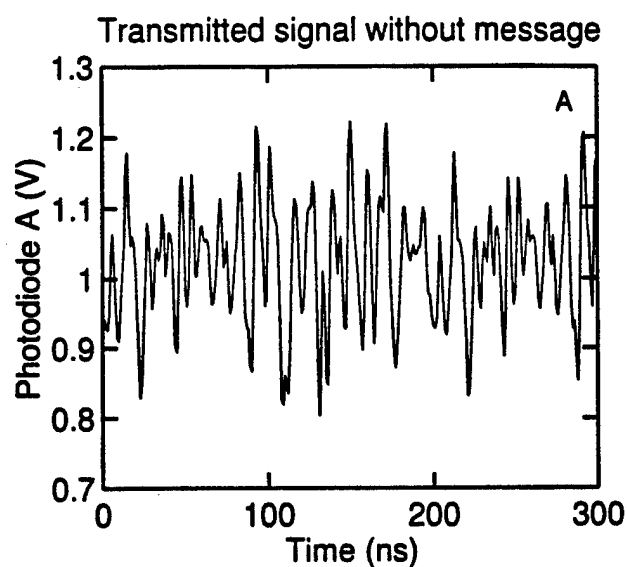


Fig. 1



False-nearest-neighbor analysis of attractor dimension

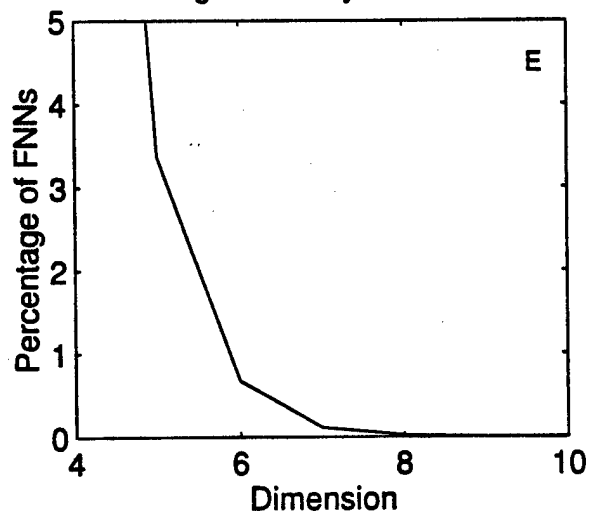


Fig. 2

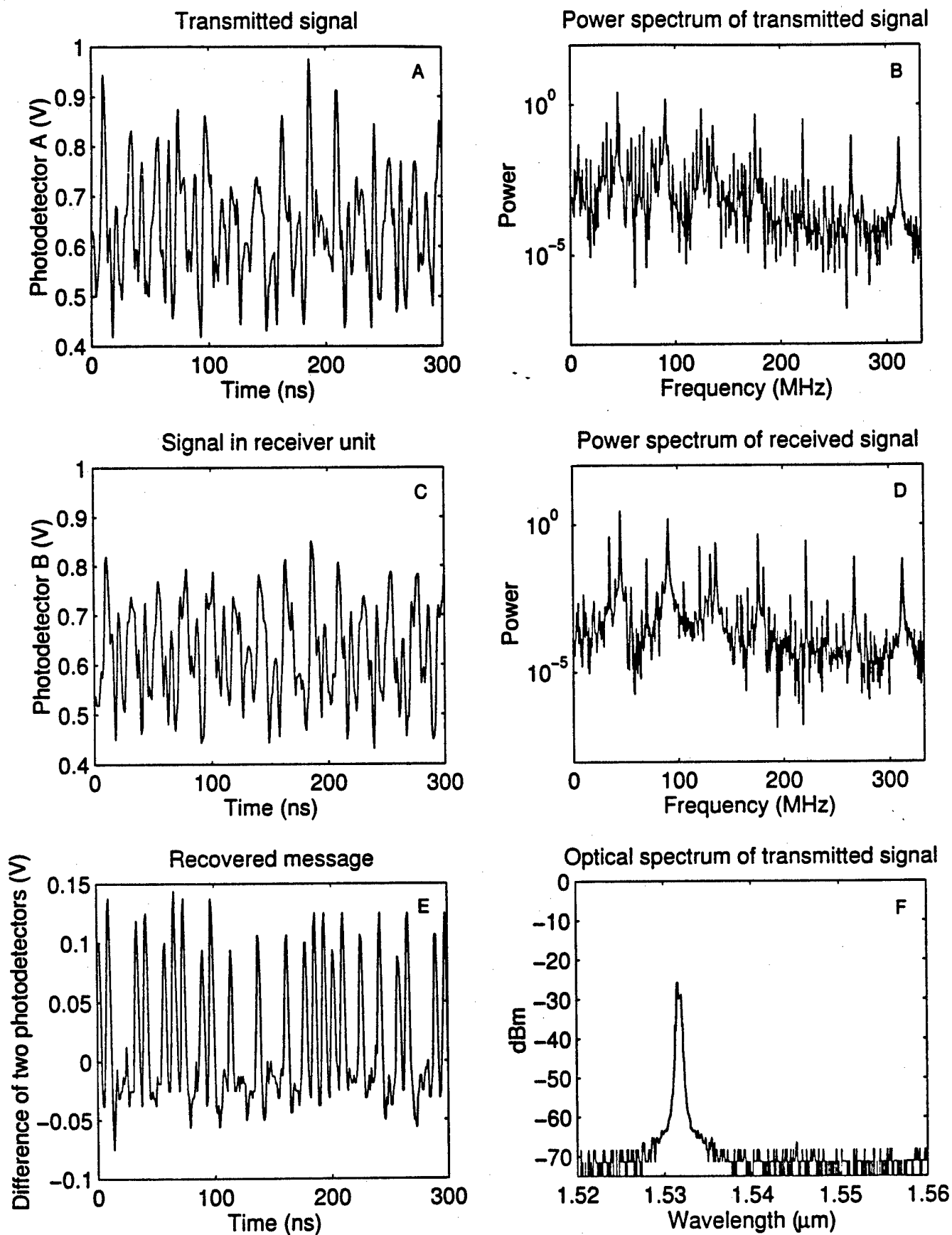


Fig. 3

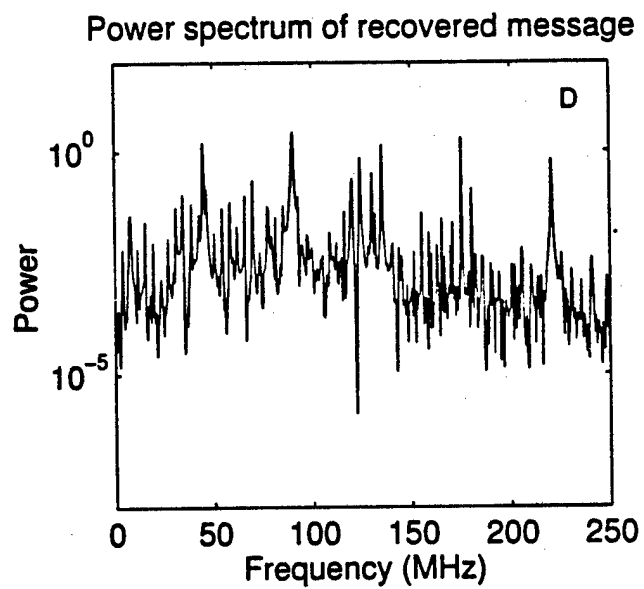
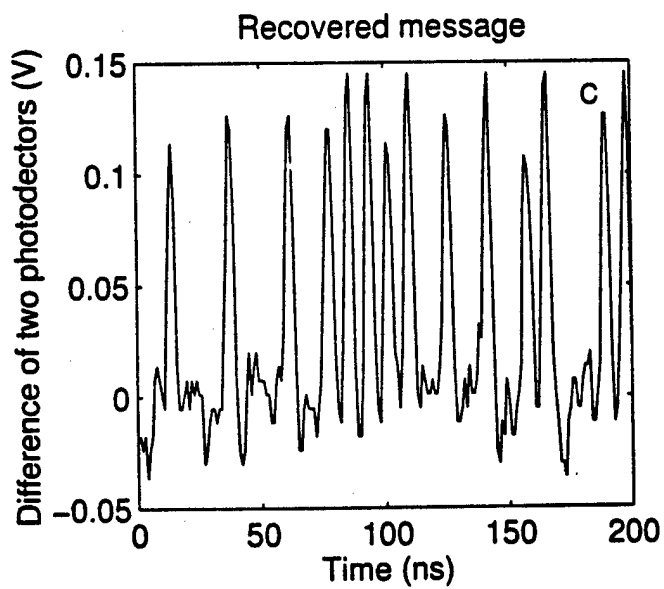
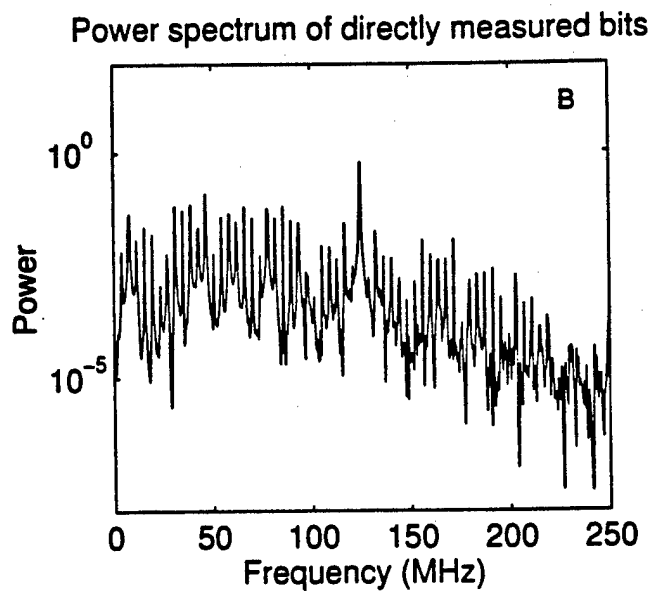
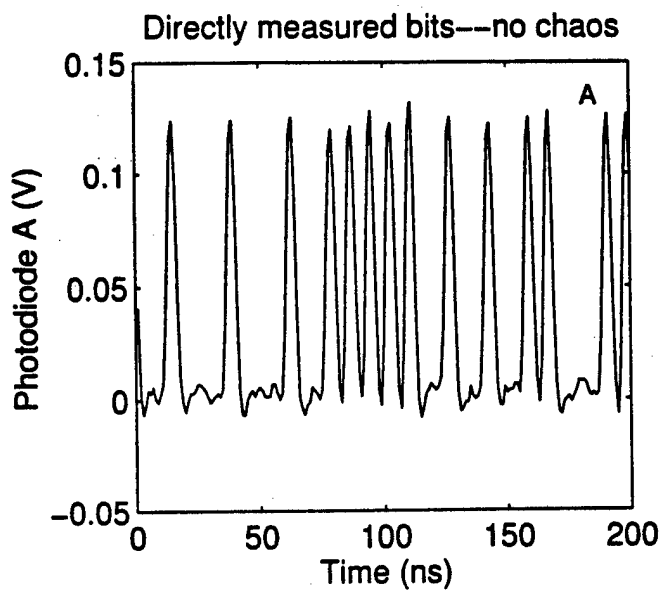


Fig. 4

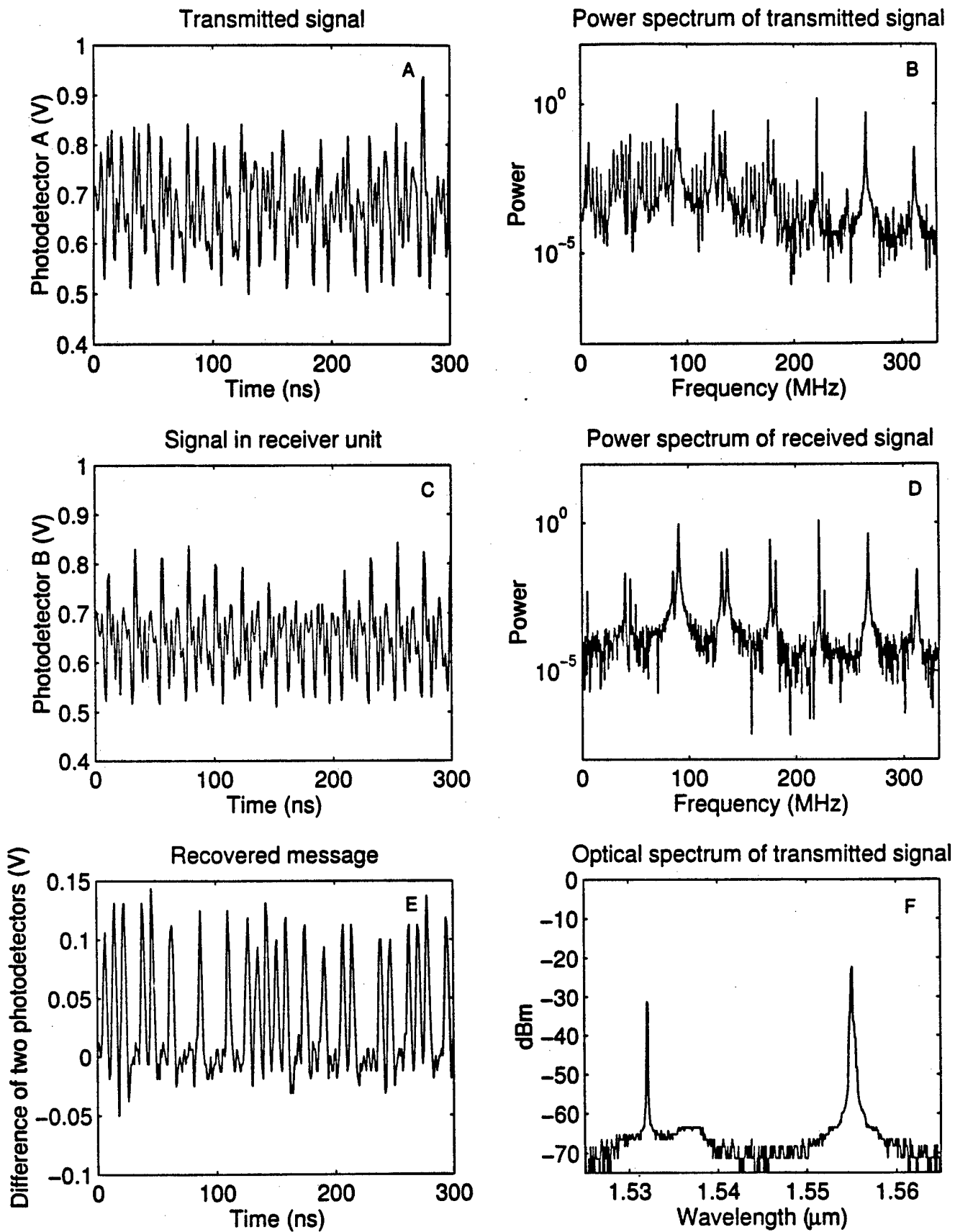


Fig. 5

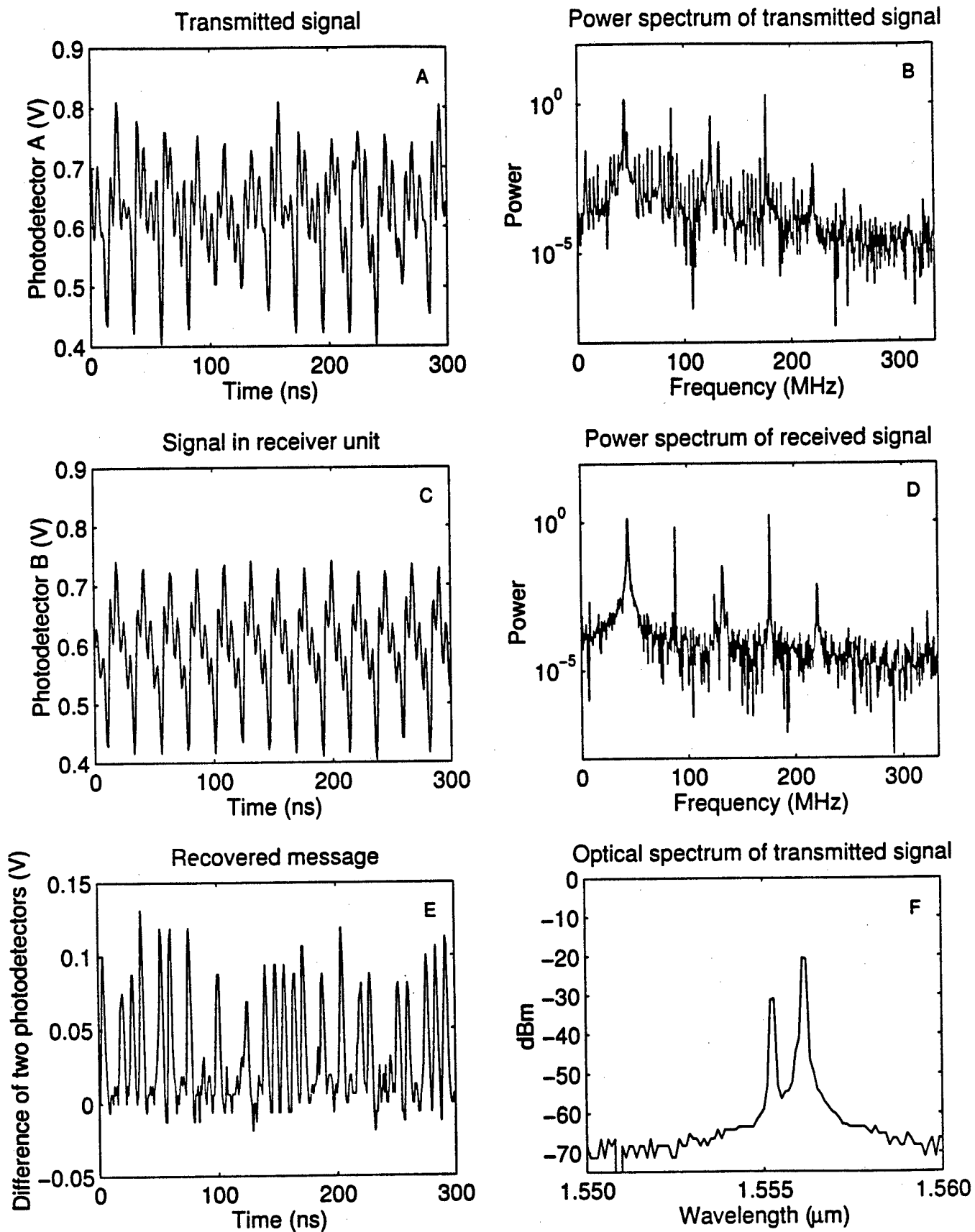


Fig. 6

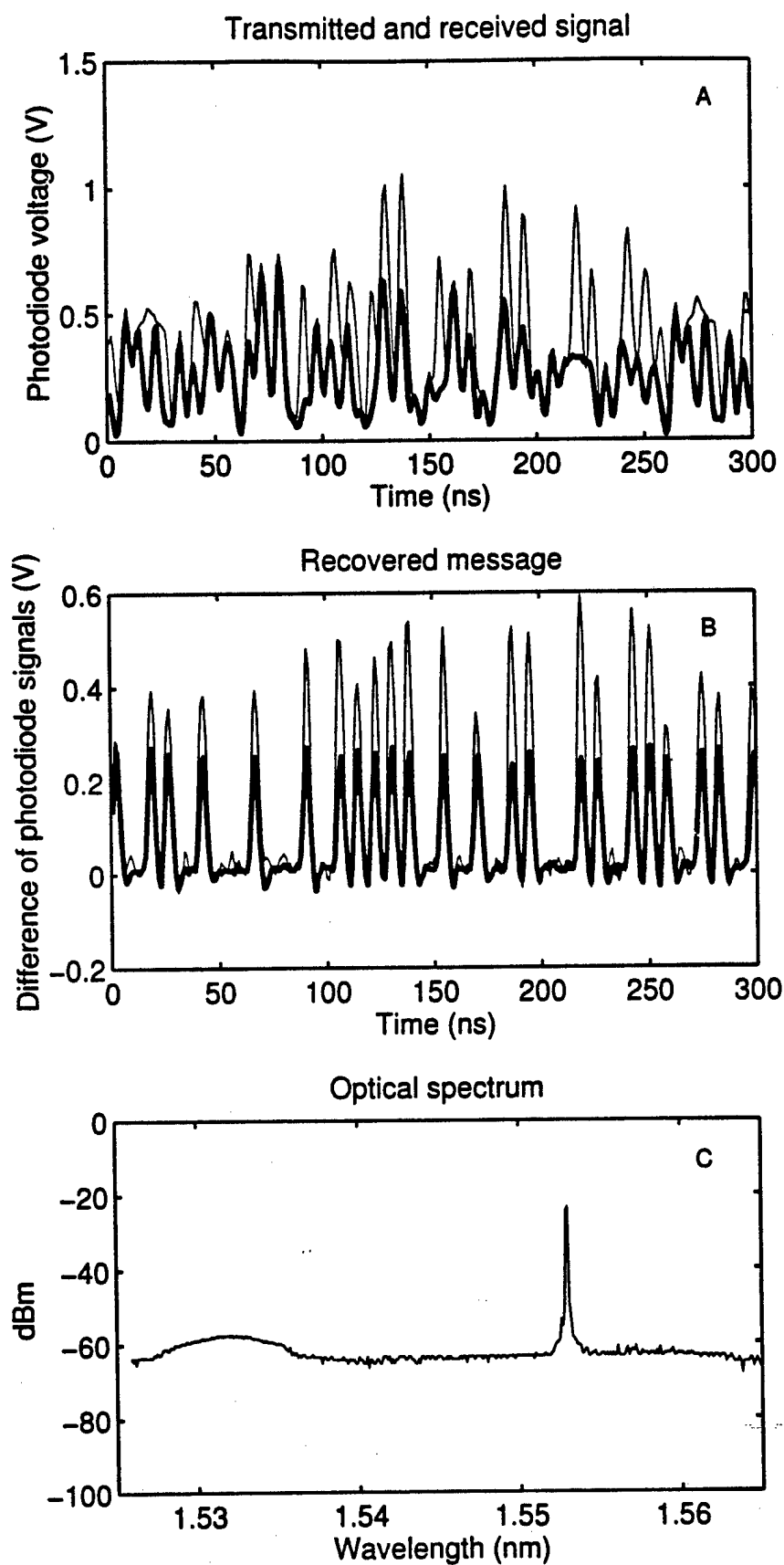


Fig. 7

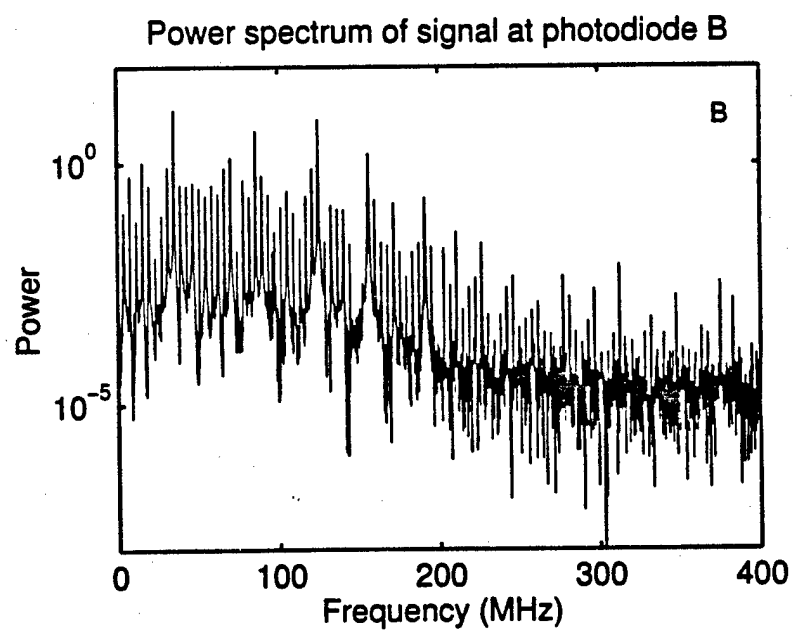
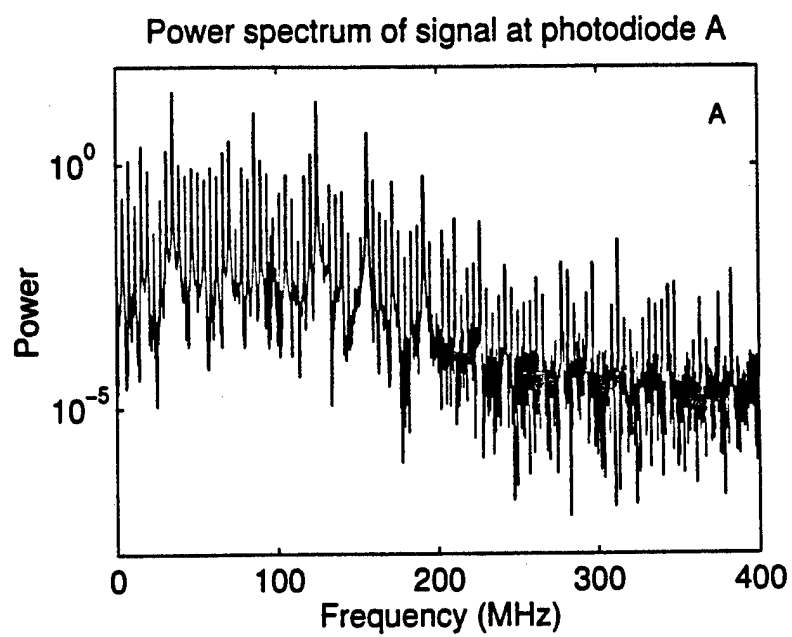


Fig. 8

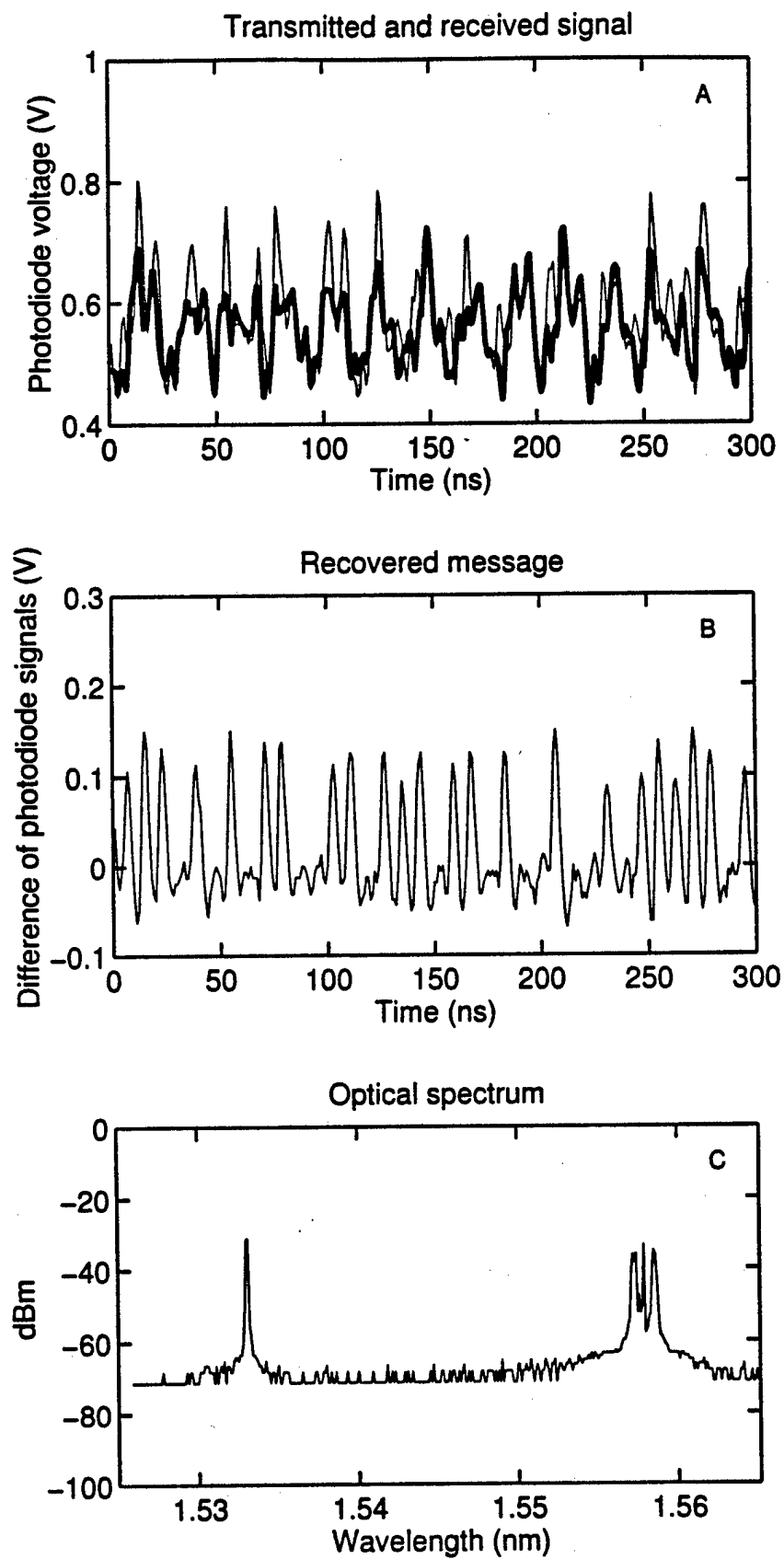


Fig. 9

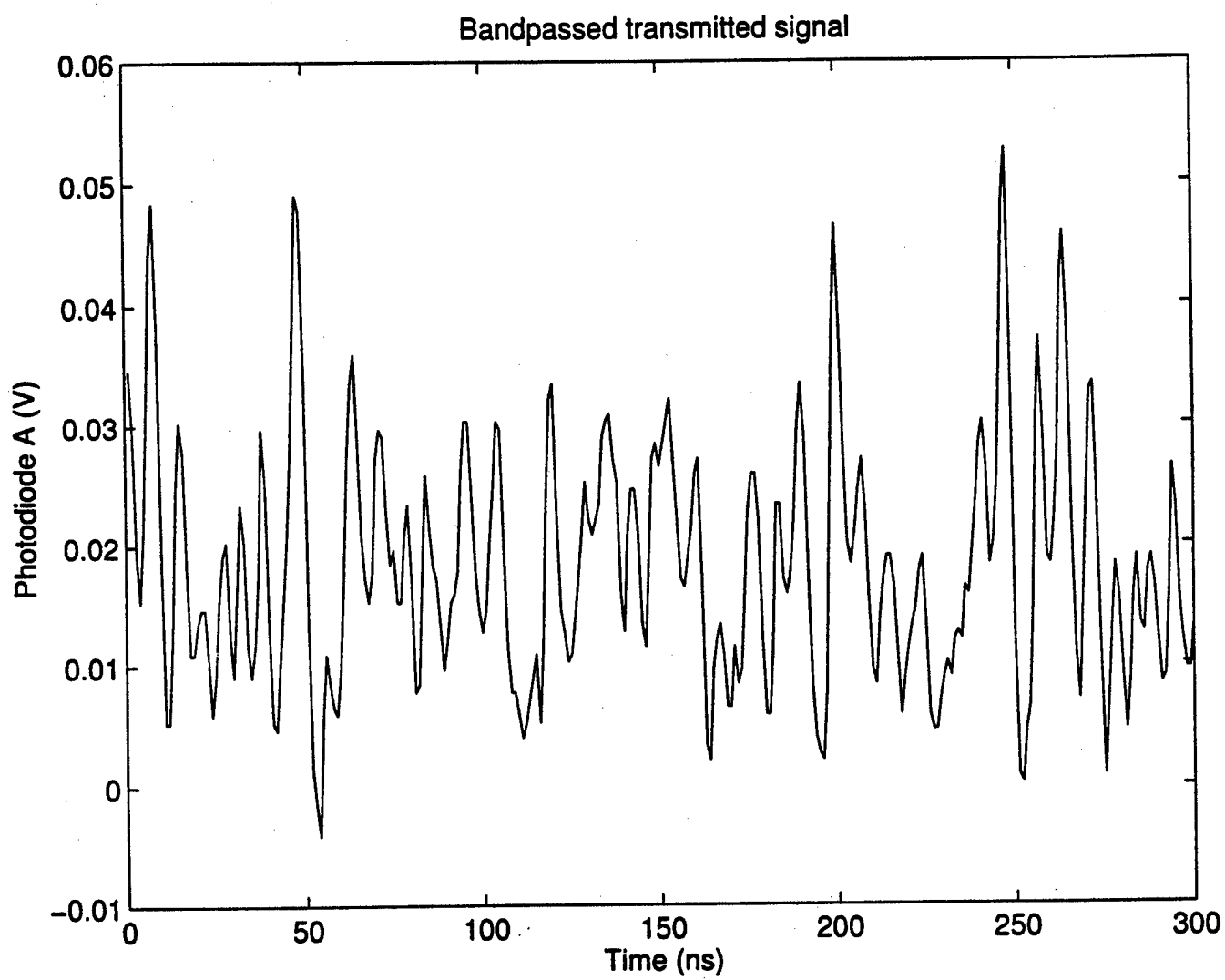


Fig. 10

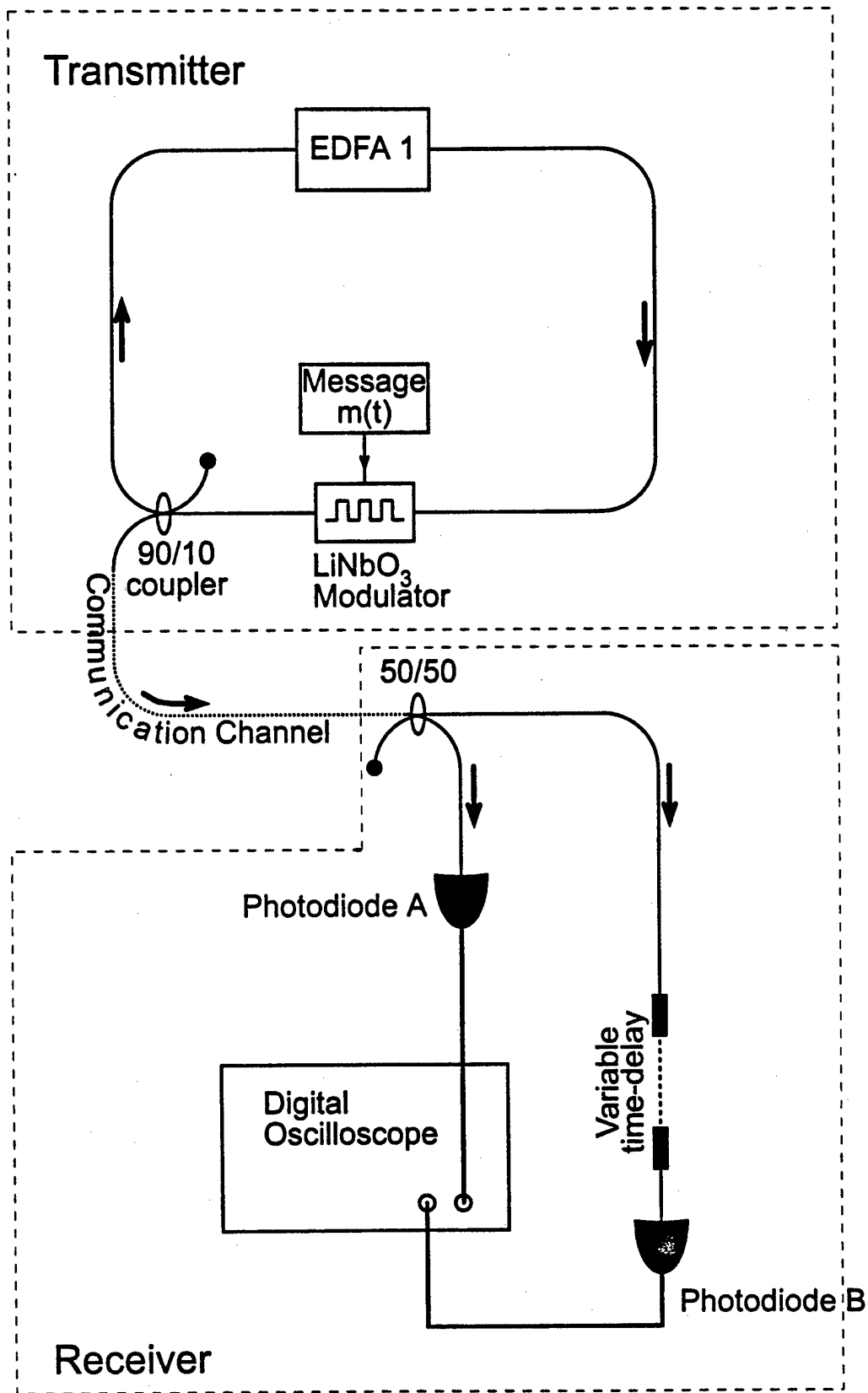


Fig. 11

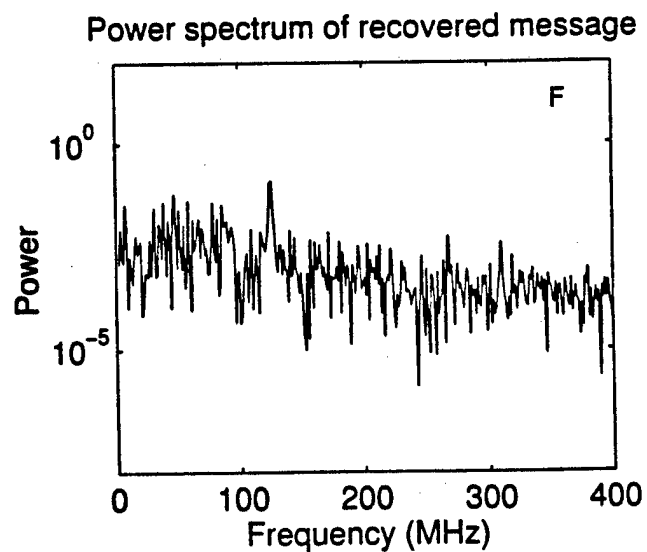
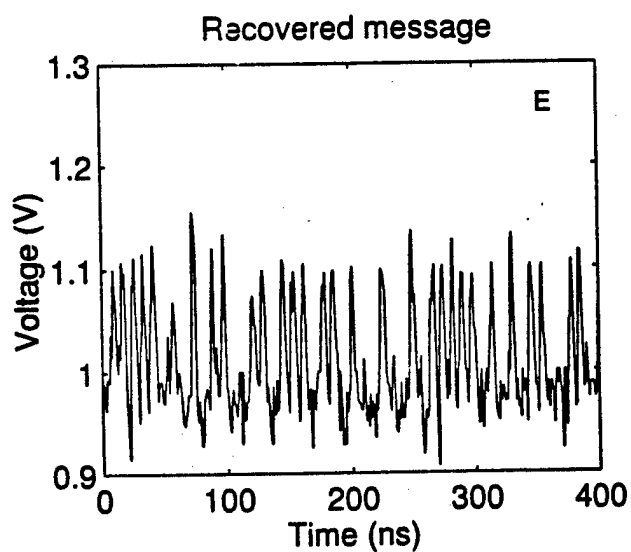
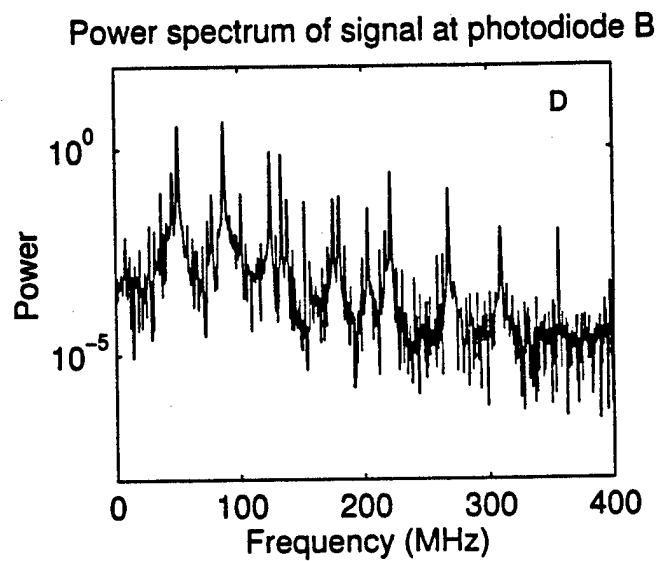
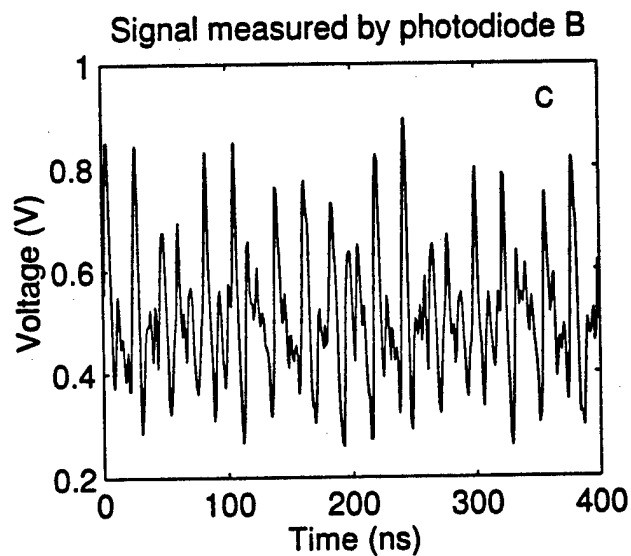
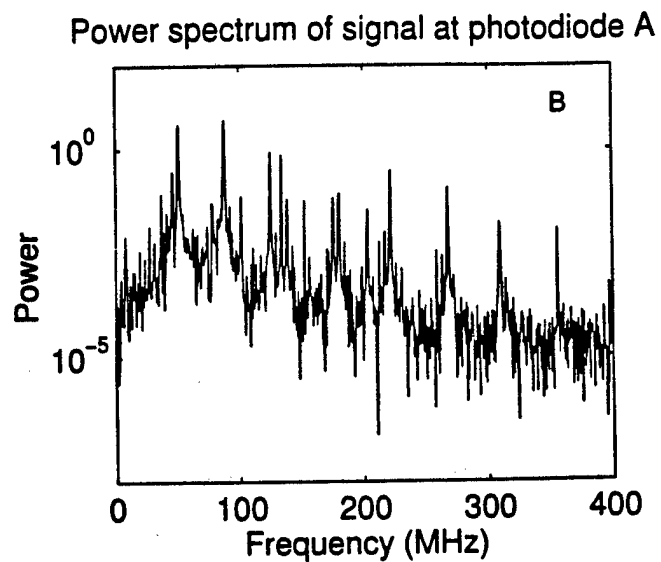
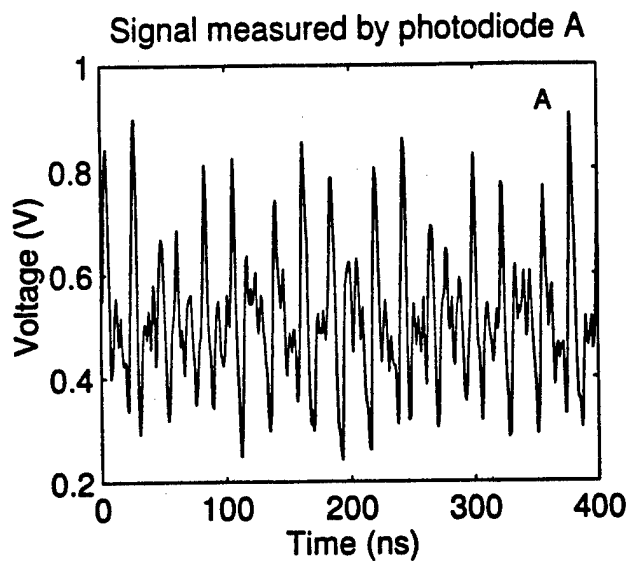


Fig. 12

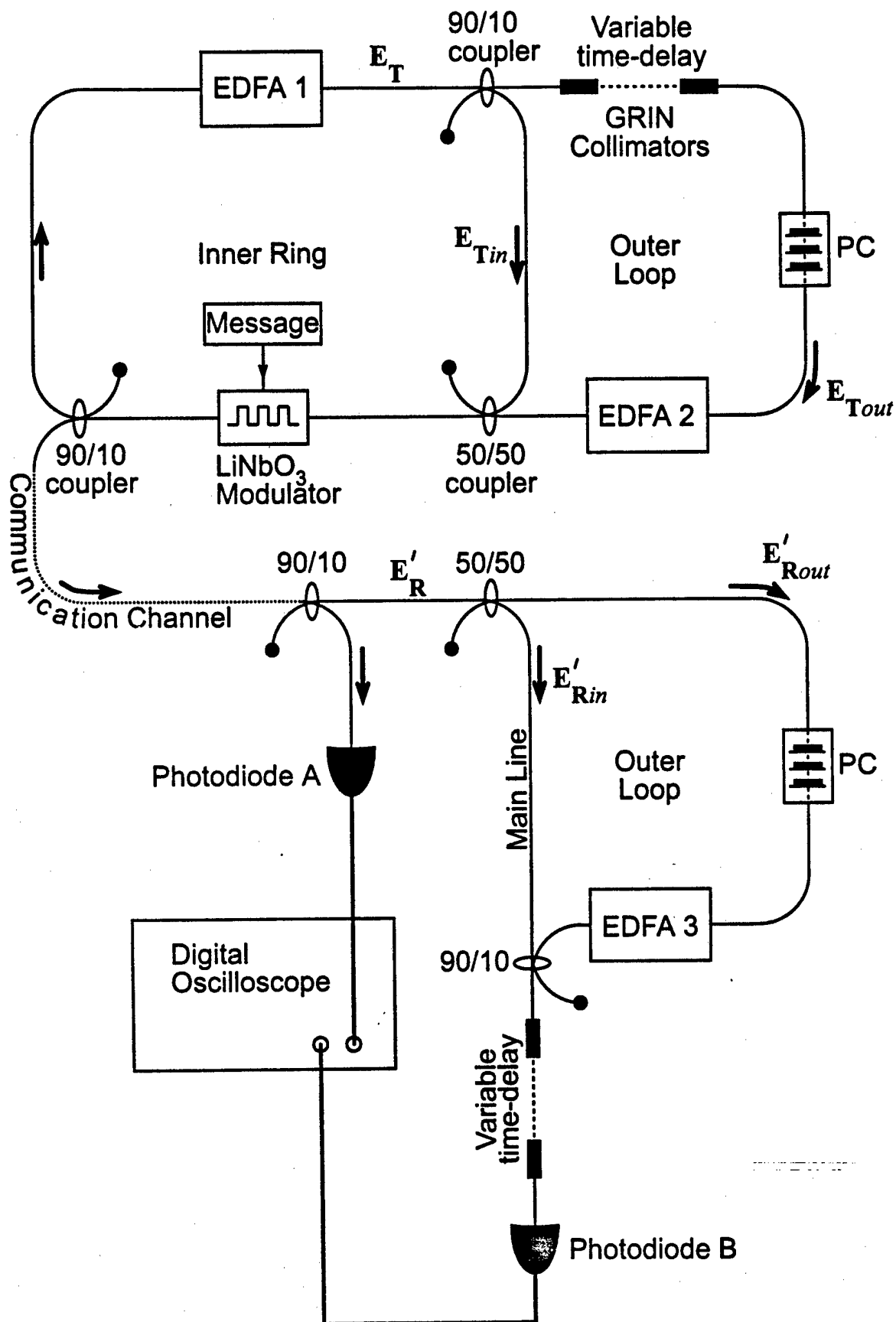


Fig. 13

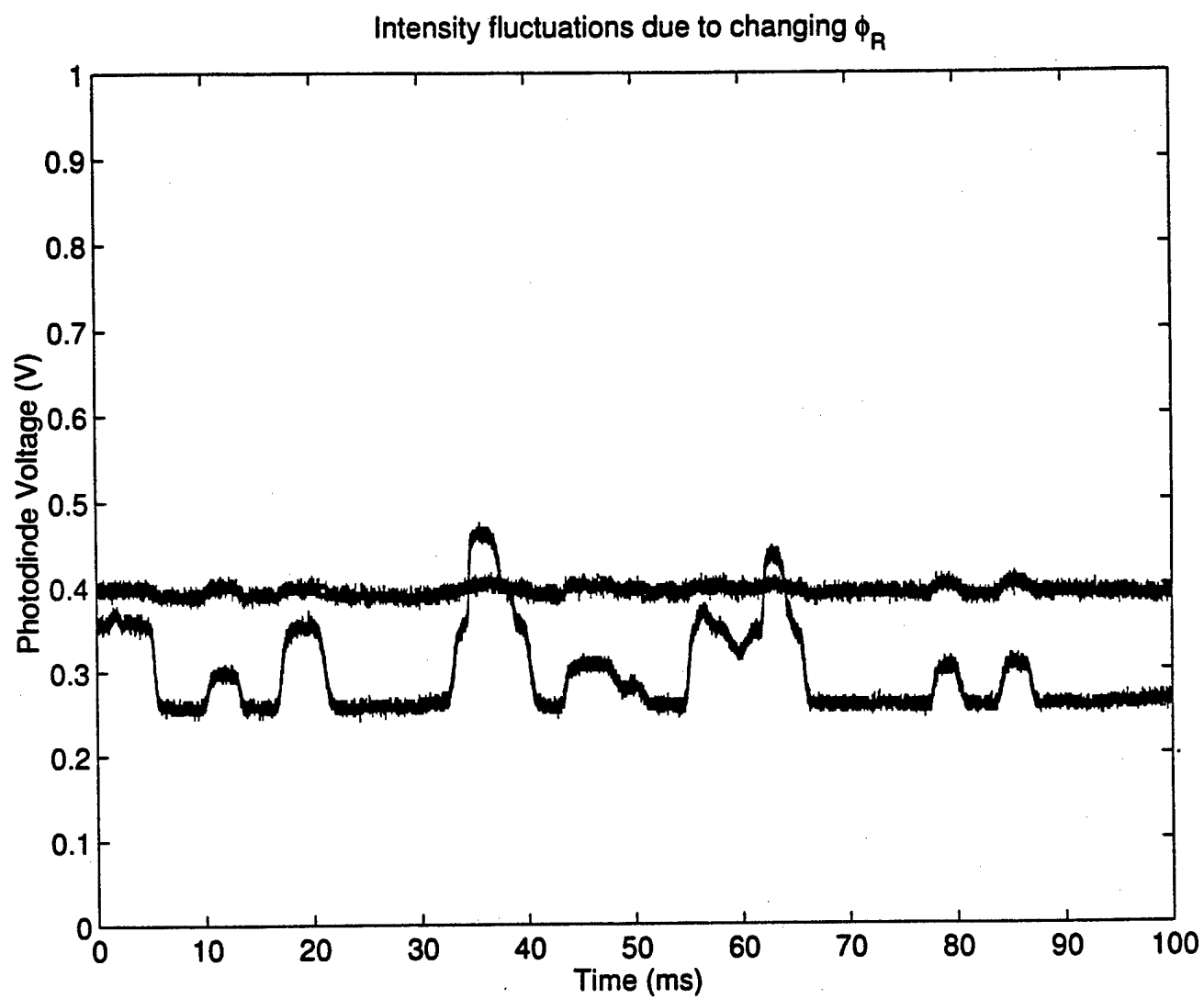


Fig. 14

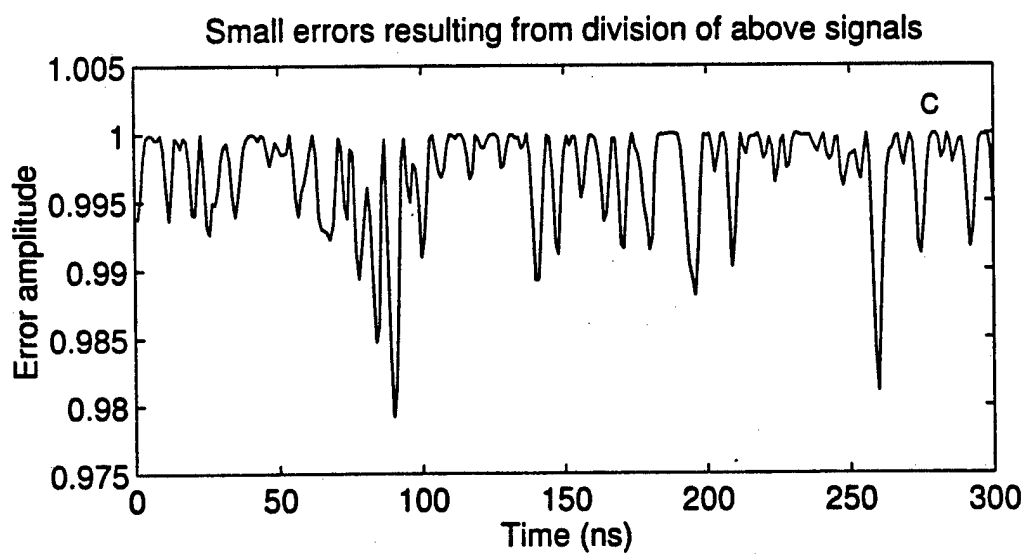
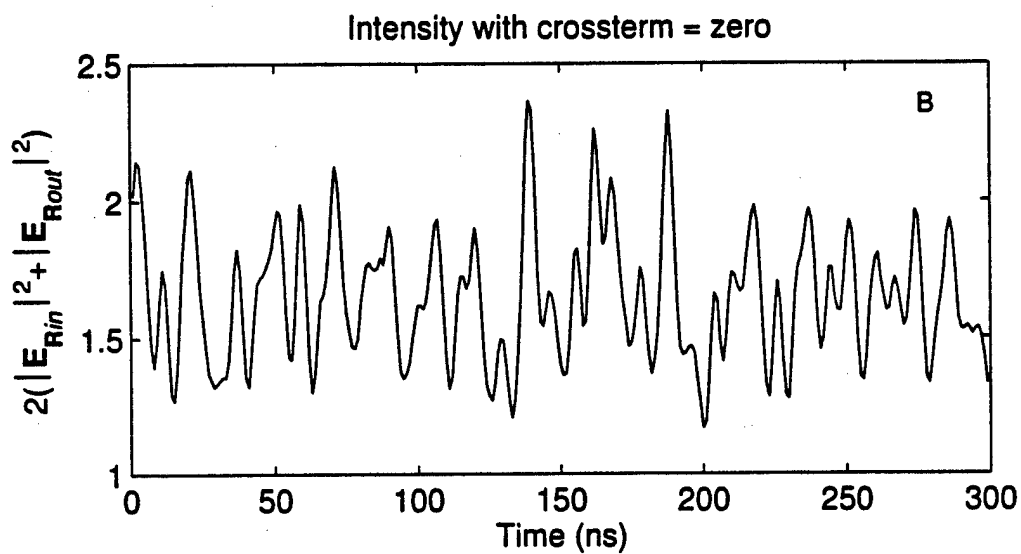
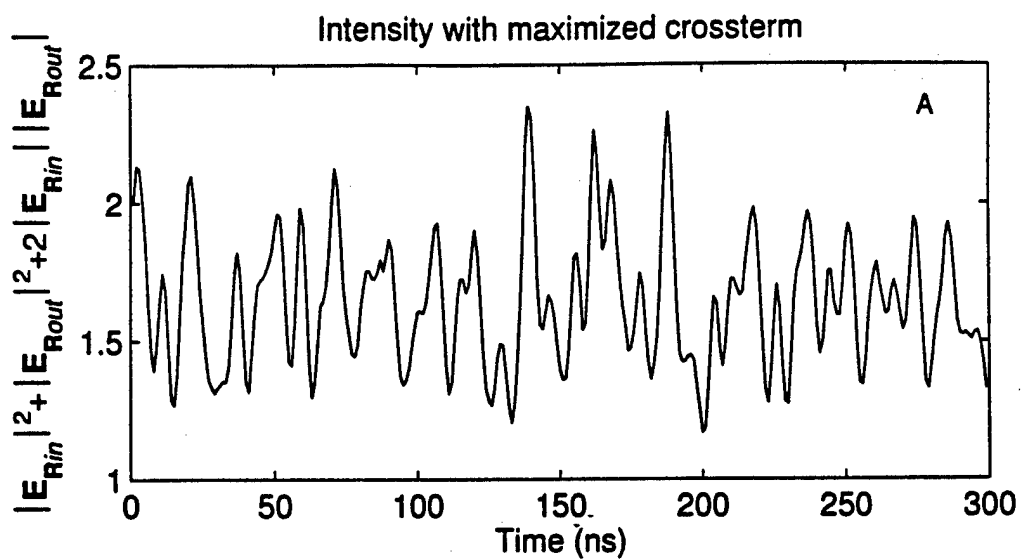


Fig. 15

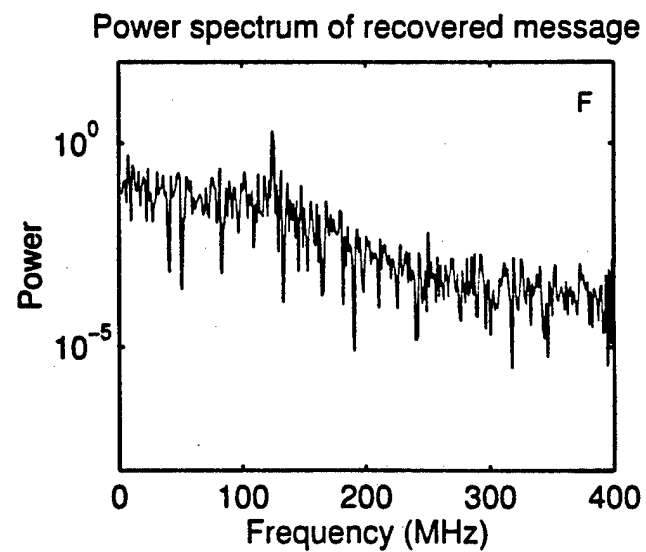
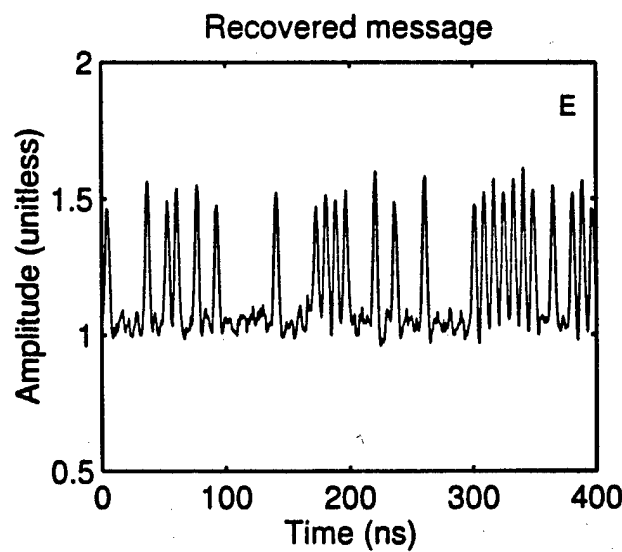
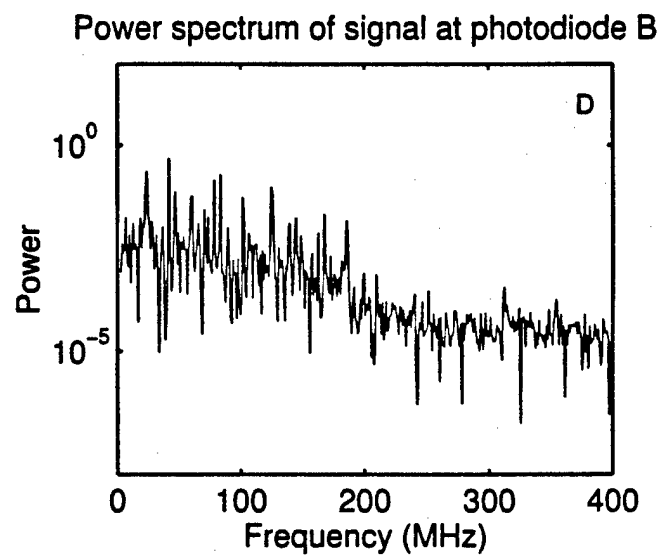
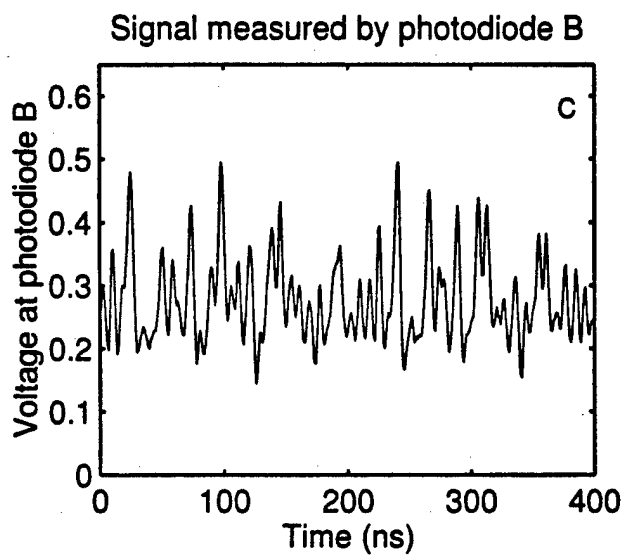
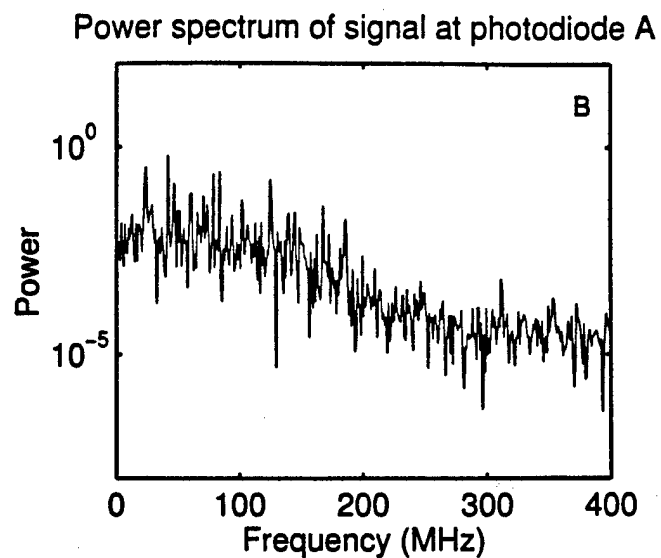
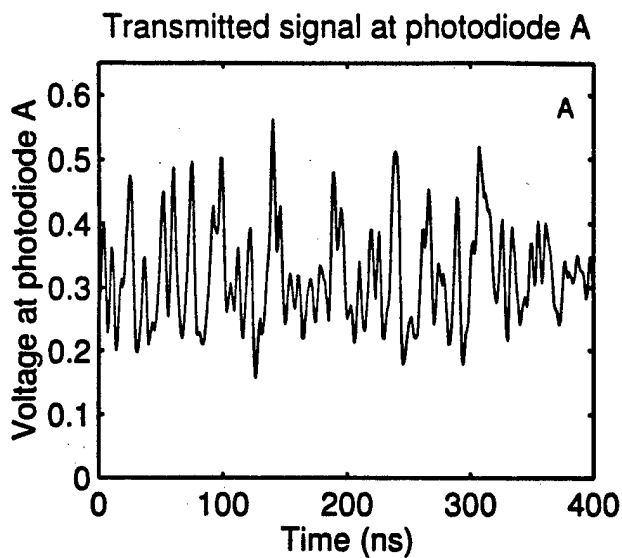


Fig. 16

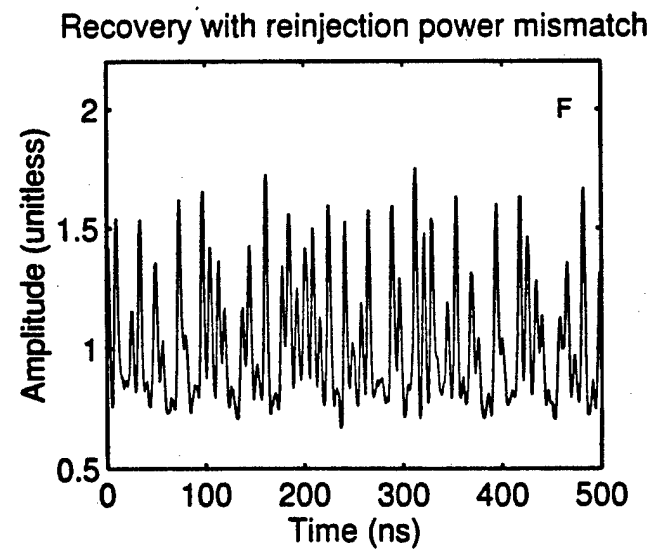
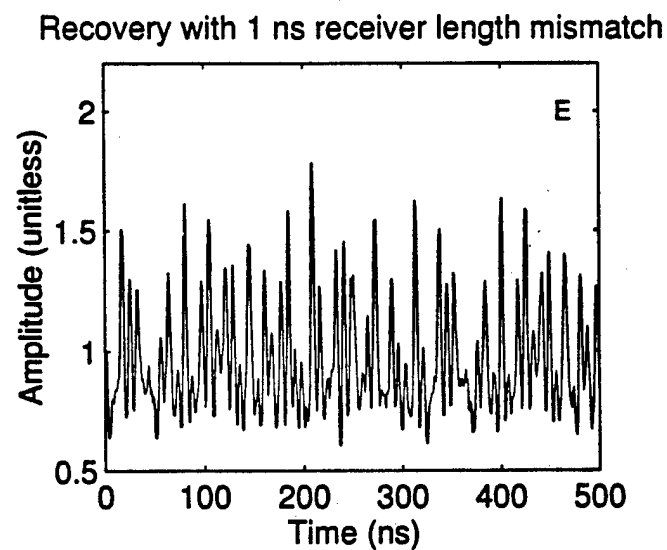
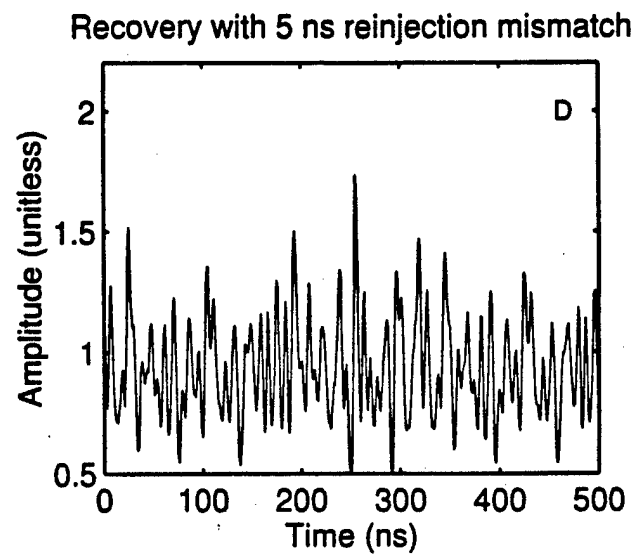
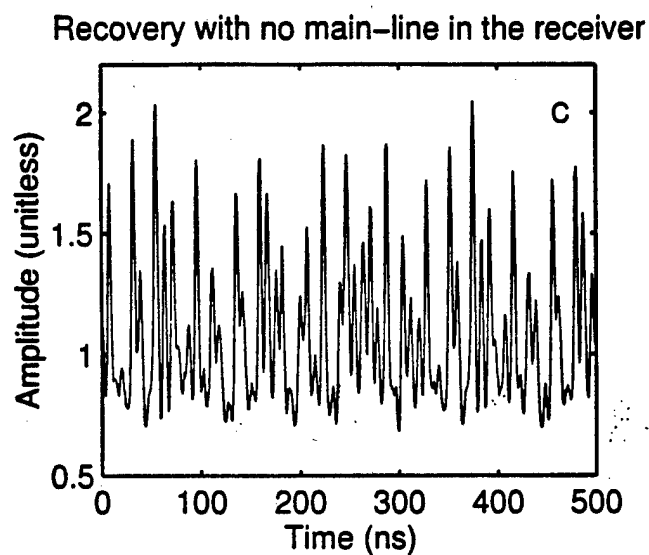
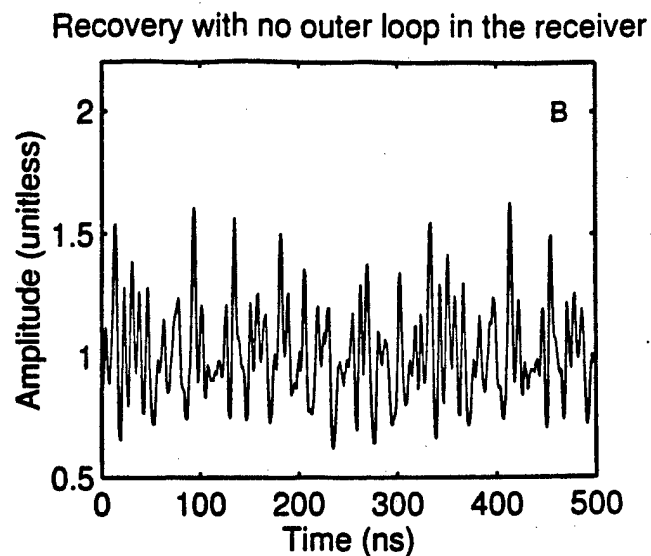
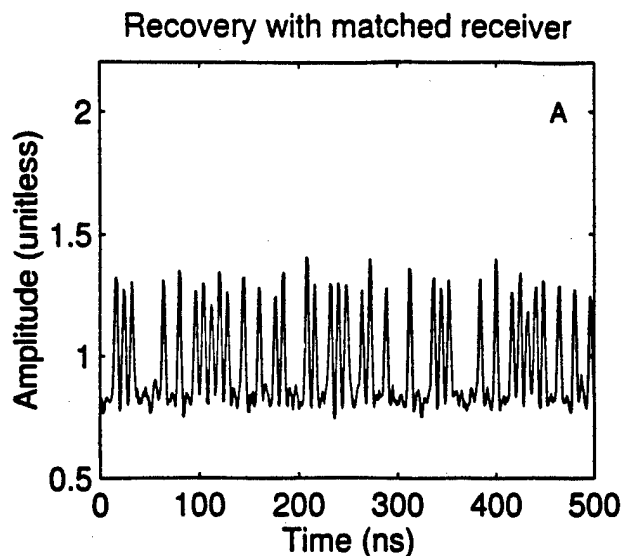


Fig. 17

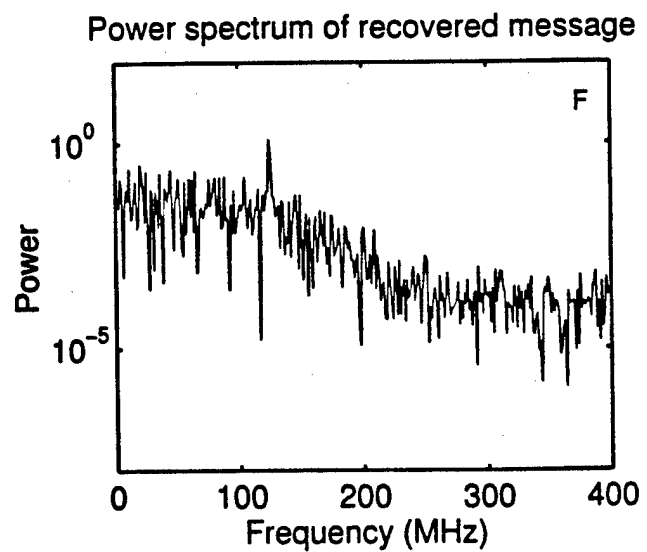
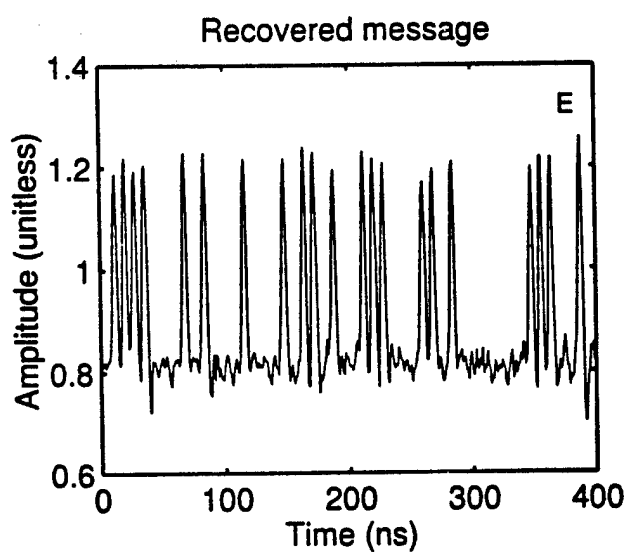
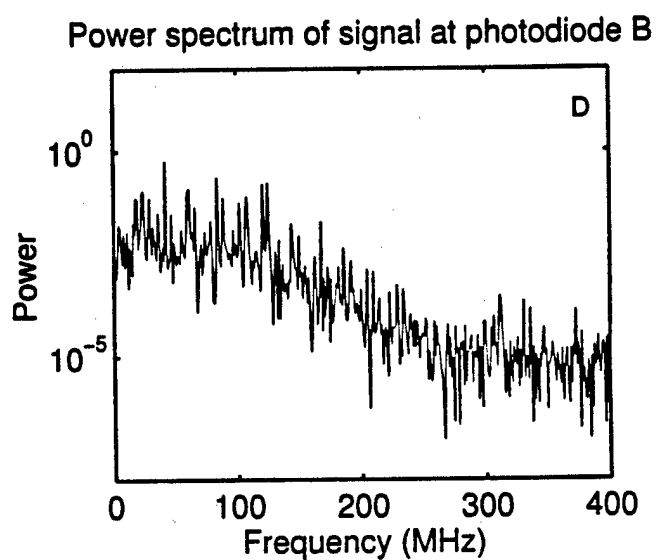
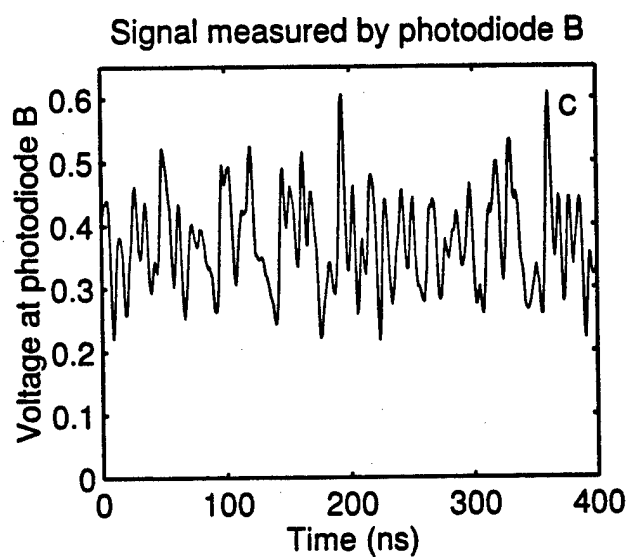
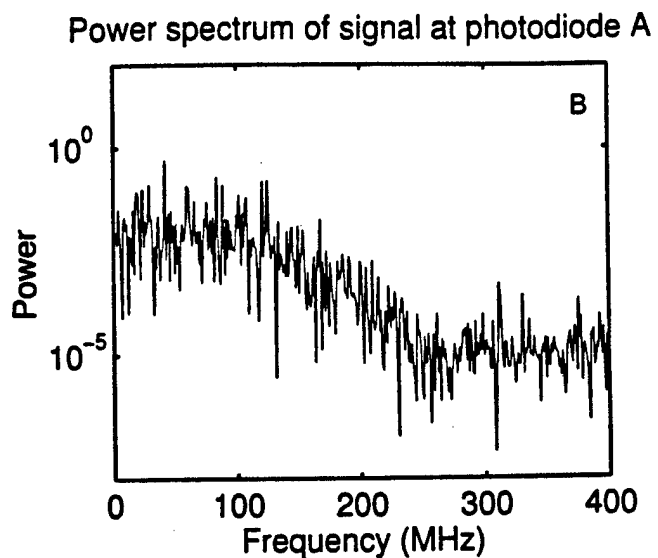
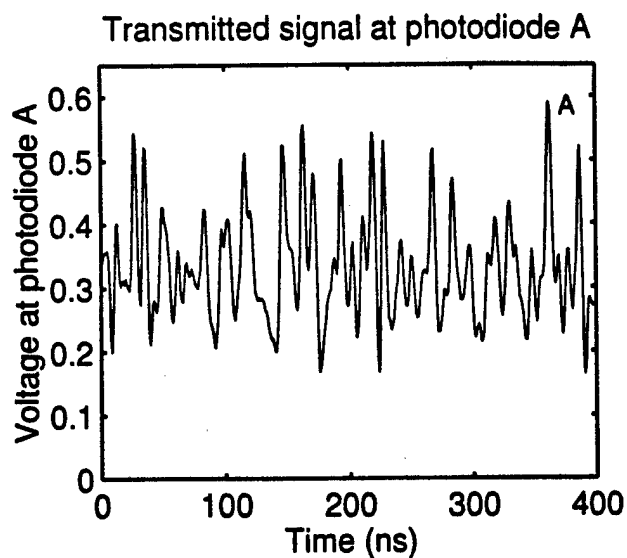


Fig 18

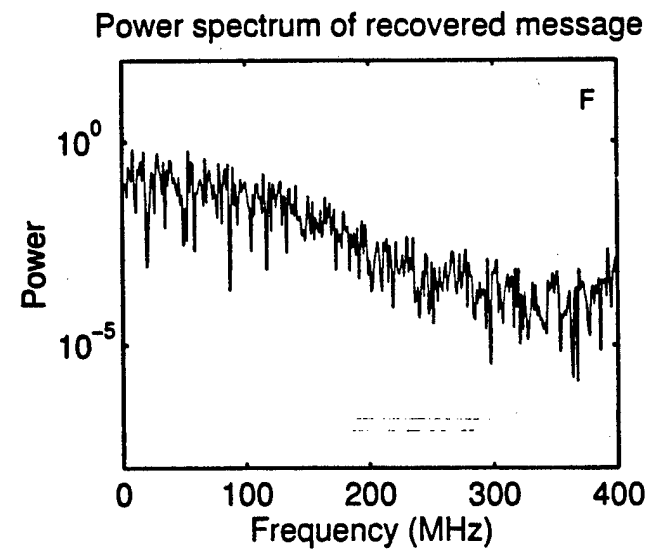
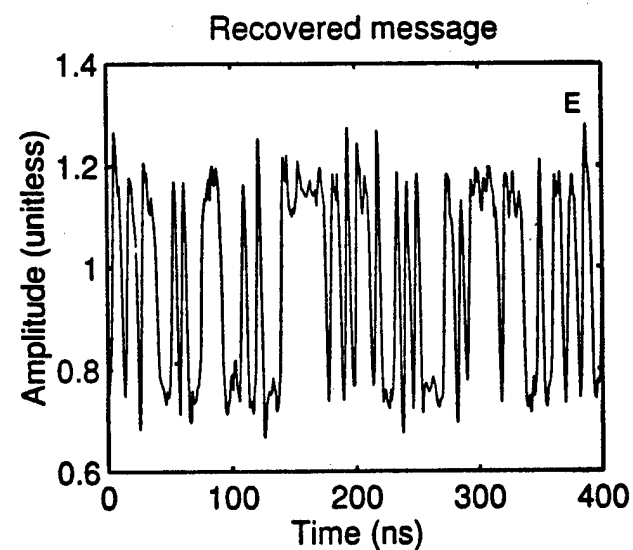
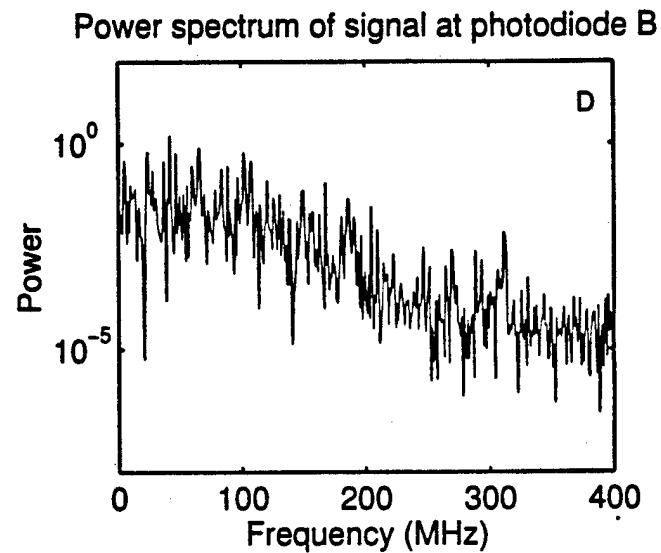
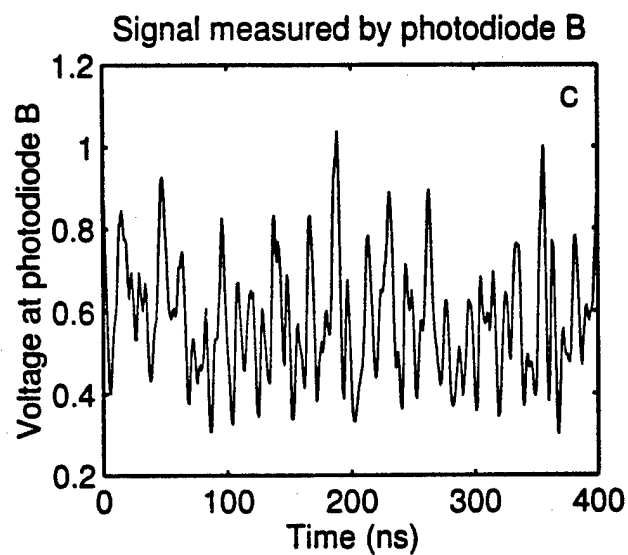
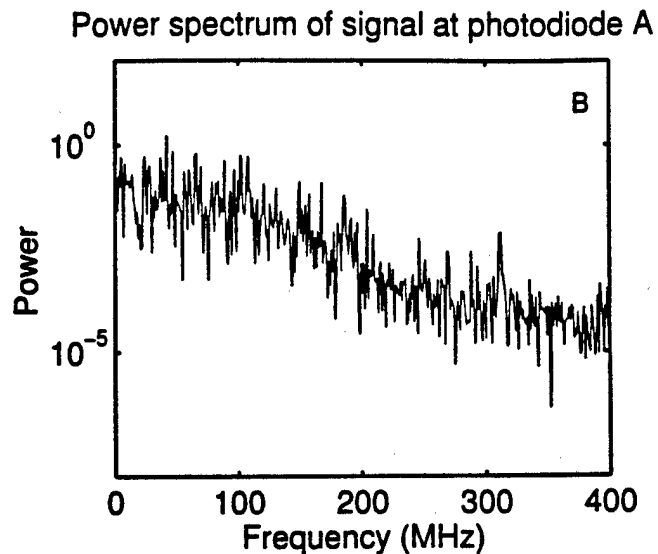
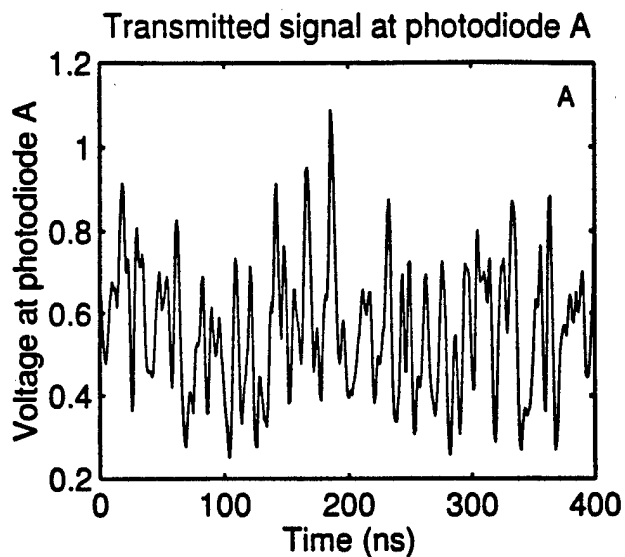


Fig. 19

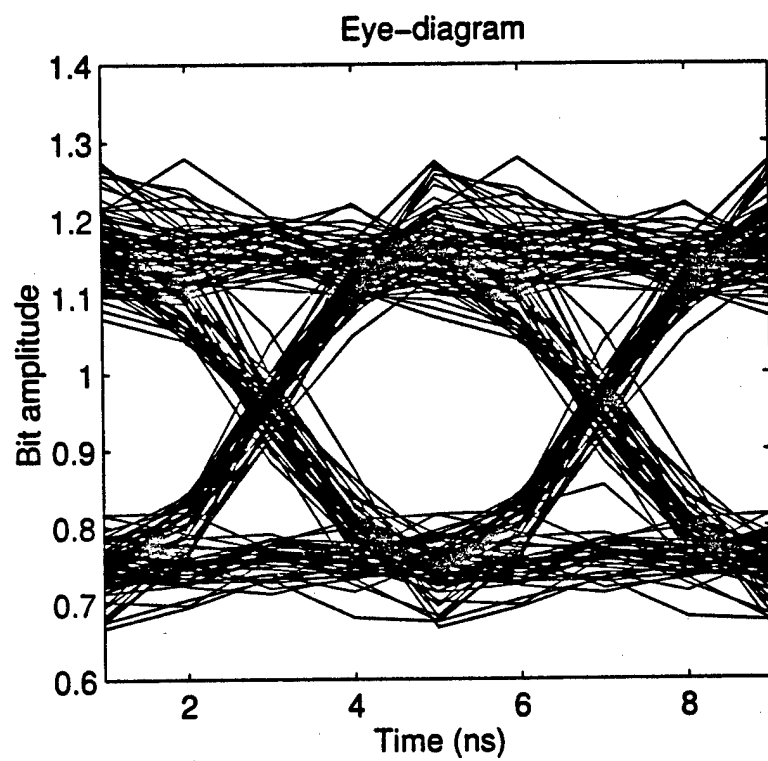


Fig. 20

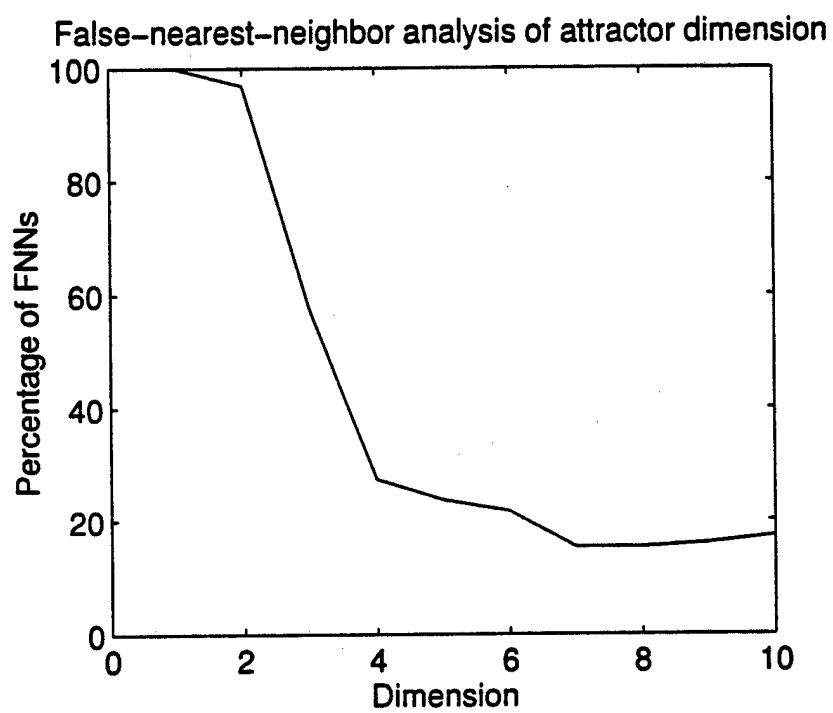


Fig. 21



ELSEVIER

1 June 1999

OPTICS
COMMUNICATIONS

Optics Communications 164 (1999) 107–120

www.elsevier.com/locate/optcom

Full length article

High-speed fiber-optic polarization analyzer: measurements of the polarization dynamics of an erbium-doped fiber ring laser

Gregory D. Van Wiggeren, Rajarshi Roy *

School of Physics, Georgia Institute of Technology, 837 State Street, Atlanta, GA 30332-0430, USA

Received 15 February 1999; accepted 24 March 1999

Abstract

Accurate measurements of fluctuating states of polarization (SOP) require determinations of the Stokes parameters on shorter time-scales than those of the fluctuations. For light sources that generate very rapid polarization and intensity fluctuations, such as erbium-doped fiber ring lasers (EDFRLs), conventional polarization analyzers are not sufficient. We describe a technique for measuring rapidly fluctuating states of polarization using a fiber-optic polarization analyzer. SOP fluctuations at rates up to 125 MHz can be accurately measured, a rate limited by the detection equipment (photodiodes and oscilloscope). Using the polarization analyzer, experimental measurements are made which provide new insights into the rapid polarization dynamics of an EDFRL. © 1999 Published by Elsevier Science B.V. All rights reserved.

PACS: 07.60.Fs; 42.65.Sf; 42.55.Wd; 42.25.Ja

Keywords: Polarimetry; Erbium-doped fiber lasers; Laser polarization dynamics; Optical chaos; Instabilities

1. Introduction

Devices to specify the state of polarization (SOP) of light have been commercially available for many years, but these devices are not designed to measure light with rapid fluctuations of its SOP. Indeed, these devices typically require stable SOPs for time-scales from milliseconds to seconds. Accurate measurements of some optical phenomena, however, require tracking a fluctuating SOP on much faster time-scales. The polarization analyzer described here is

capable of measuring fluctuating SOPs with time-scales as short as several nanoseconds. Even faster measurements are conceptually possible; the bandwidth of the photodiodes (3-dB roll-off at 125 MHz) ultimately limits the speed of the SOP fluctuations that can be accurately measured.

In Section 2, we present an overview of the theory of optical polarization that will assist the reader in understanding the description of the apparatus and the interpretation of the experimental results. Section 3 briefly describes the experimental apparatus and technique while focusing on experimental results and measurements. Specifically, the polarization dynamics of chaotic and self-pulsing light from an erbium-doped fiber ring laser (EDFRL) are mea-

* Corresponding author. Tel.: +1-404-894-6819; Fax: +1-404-894-9958; E-mail: rajarshi.roy@physics.gatech.edu

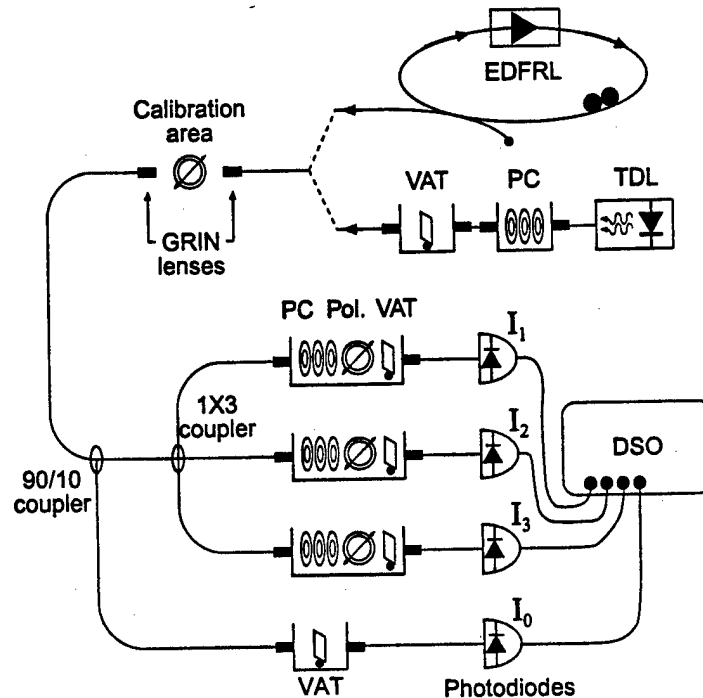


Fig. 1. Diagram of experimental apparatus. During the calibration process, light from the tunable diode laser (TDL) is transmitted to the apparatus. Once calibrated, light from an EDFRL is sent to the apparatus for measurement of the Stokes parameters. The variable attenuators (VATs) placed before the photodiodes are intended to prevent saturation of the photodiodes. The polarization controllers (PCs) consist of a sequence of three waveplates and allow light from any input polarization to be adjusted to any output polarization. The polarizers (Pol.) ensure that the photodiodes measure only one component of the light. All of these free-space optical elements are placed between coupled graded-index (GRIN) lenses, which allow the light to be coupled out of and back into fiber. The digital sampling oscilloscope (DSO) records the intensities measured by the photodiodes.

sured. Section 4, the conclusion, discusses the advantages and features of this technique. A more thorough description of the apparatus and the calibration procedures is provided in Appendix A.

2. Theoretical foundation

For a quasi-monochromatic lightwave, the electric field, E , can be described as the sum of two orthogo-

nal components, $E(t) = E_x(t) + E_y(t)$, where

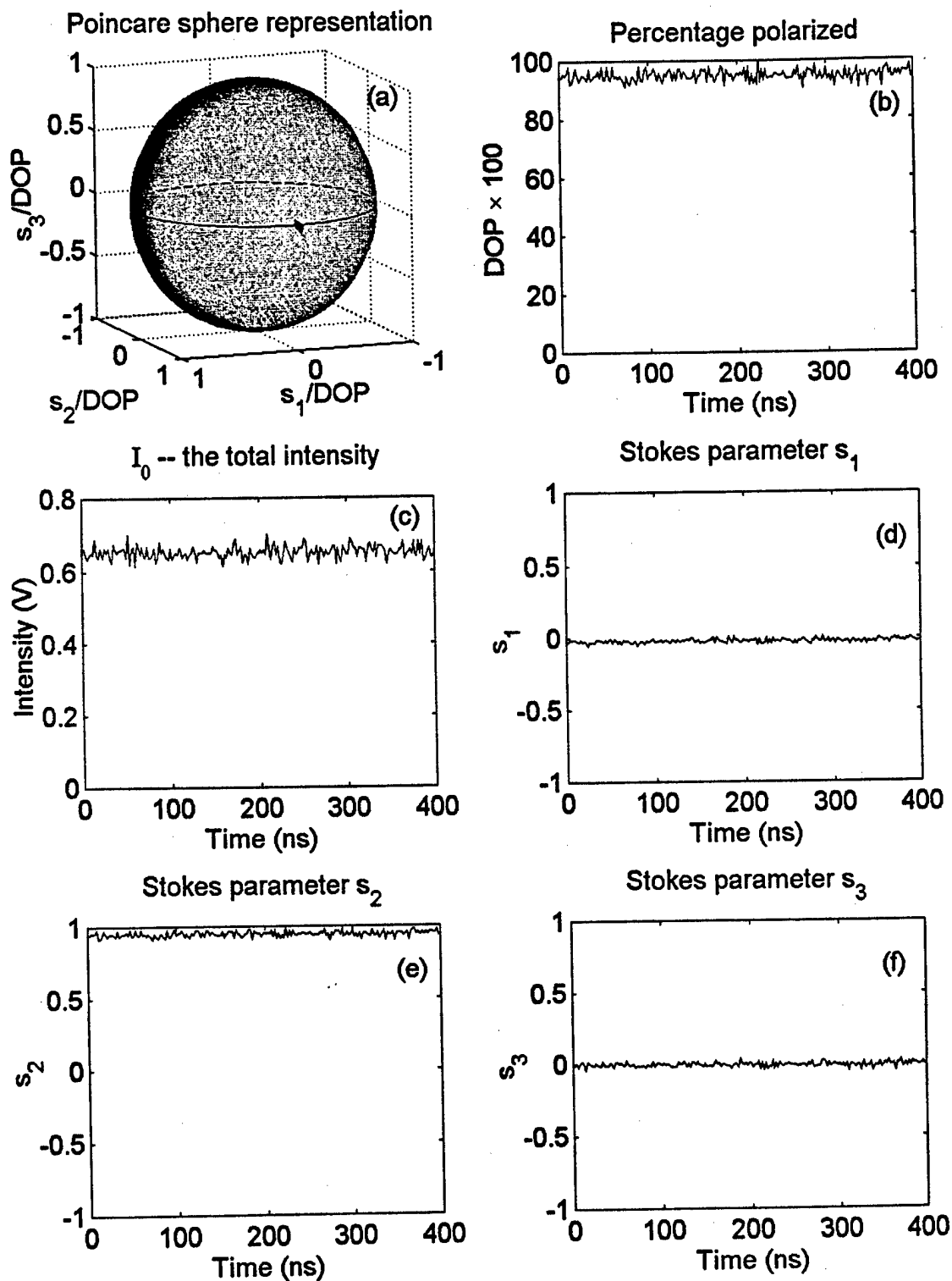
$$E_x(t) = \hat{i}E_{0x}(t)\cos[kz - \omega t + \varepsilon_x(t)] \quad (1)$$

and

$$E_y(t) = \hat{j}E_{0y}(t)\cos[kz - \omega t + \varepsilon_y(t)]. \quad (2)$$

In these equation E_{0x} and E_{0y} are both real numbers. The phase of each component is given by $\varepsilon_{x,y}$.

Fig. 2. This figure is intended to illustrate the accuracy of our measurement of the SOP. The light analyzed is produced by the EDFRL and possesses rapid intensity and polarization fluctuations. A polarizer at 45° has been placed in the calibration area. Thus, the ideal measurement of the SOP should, in spite of the intensity fluctuations evident in (c), give $\vec{s} = (1,0,1,0)$. The experimental measurement, as indicated by (d–f), is very close to this ideal. The DOP shown in (b) is close to 100%, as one would expect for light that passes through a polarizer.



A common way of specifying the SOP of a lightwave is to determine its Stokes parameters. As described in Refs. [1,2], the four Stokes parameters for such a lightwave can be defined as

$$\begin{aligned} S_0 &= \langle E_{0x}^2 \rangle + \langle E_{0y}^2 \rangle \\ S_1 &= \langle E_{0x}^2 \rangle - \langle E_{0y}^2 \rangle \\ S_2 &= \langle 2 E_{0x} E_{0y} \cos(\varepsilon) \rangle \\ S_3 &= \langle 2 E_{0x} E_{0y} \sin(\varepsilon) \rangle, \end{aligned} \quad (3)$$

where ε is just the relative phase, $\varepsilon_y - \varepsilon_x$, between the two electric field components. Clearly, S_0 represents just the total intensity of the light. S_1 reflects a tendency for the light to have its energy concentrated along either the x or y axes. S_2 and S_3 depend on the relative phase between these two components.

The $\langle \rangle$ expectation-value brackets must be included in Eq. (3) because it is possible that the arguments within them can fluctuate on time scales that are shorter than the time during which the measurement is made. To fully measure the time-evolution of a lightwave's SOP, it is necessary to use a polarization analyzer that operates on time-scales as fast or faster than the SOP fluctuations. For example, sunlight is called unpolarized ($S_1 = S_2 = S_3 = 0$) because any real polarization analyzer averages over sunlight's very rapid and statistically random polarization fluctuations. Yet, the electric field of a ray of sunlight at any point in space and time must possess an amplitude, orientation, and phase. While the time-scales for the SOP fluctuation of sunlight are much too fast to be measured with the technique presented here, some optical phenomena which were previously too fast to be fully measured using conventional polarimetry can now be observed. In some modes of operation, the polarization dynamics of an EDFRL occur on time scales of several nanoseconds. Such time scales are long enough to permit full measurement of the EDFRL polarization dynamics using the high-speed polarization analyzer presented here.

Light that is neither completely unpolarized nor completely polarized is called partially polarized. Partially polarized light can be thought of as the superposition of two components: a completely polarized lightwave and a completely unpolarized lightwave [3]. A convenient measure of the relative proportion of polarized to unpolarized light is the Degree of Polarization (DOP). The formula for the DOP is given by

$$\text{DOP} = \frac{(S_1^2 + S_2^2 + S_3^2)^{1/2}}{S_0}, \quad (4)$$

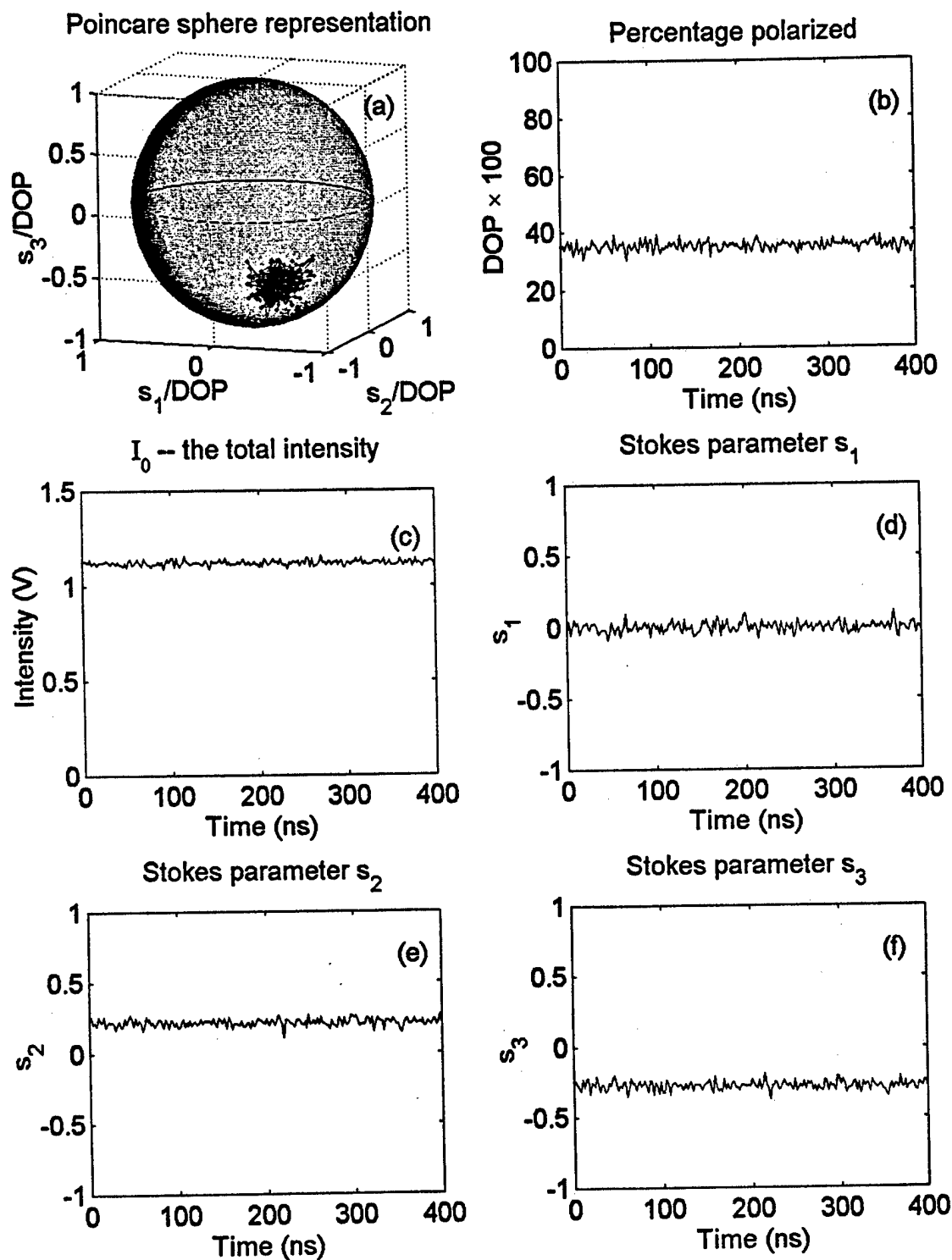
where $0 \leq \text{DOP} \leq 1$. Because of the $\langle \rangle$ brackets in Eq. (3), the calculated DOP (for a lightwave with fluctuating SOP) is affected by the speed with which the Stokes parameters can be measured.

For convenience, all of the Stokes parameters can be normalized by dividing them by S_0 . For the remainder of the paper, these normalized Stokes parameters will be written in lower-case type. With this simplification, a normalized Stokes vector for unpolarized light is simply given by $\vec{s} = (1, 0, 0, 0)$. Linearly polarized light oriented along the \hat{x} -axis becomes $\vec{s} = (1, 1, 0, 0)$, etc. With these normalized Stokes parameters, Eq. (4) can be rewritten as

$$\text{DOP} = (s_1^2 + s_2^2 + s_3^2)^{1/2}. \quad (5)$$

The Poincaré sphere [3], originally introduced by Poincaré in 1892, is a convenient way to visualize the SOP of a lightwave. The sphere is placed at the center of a three-dimensional cartesian coordinate system $s_1 s_2 s_3$, where the horizontal plane is defined by s_1 and s_2 axes, and the vertical direction is defined by the s_3 -axis. For a particular lightwave with $\text{DOP} = 1$, the values for the three Stokes parameters s_1 , s_2 , and s_3 can be plotted on the surface of the sphere with unit radius. Any point falling on the equator is linearly polarized (because $s_3 = 0$), and any point falling on a pole is circularly polarized. Thus, the latitude of a particular point gives an indication of the relative ellipticity of the lightwave's

Fig. 3. Light directly from the EDFRL is analyzed. Unlike the experiment described in Fig. 2, no polarizer was present in the calibration area. This means that all of the polarization and intensity fluctuations produced by the EDFRL are measured directly. (a) Clearly shows that the polarization of the light tends to fluctuate in a somewhat localized area on the Poincaré sphere. The relatively low DOP shown in (b) indicates that these fluctuations are actually faster than can be observed with even the technique used here.



SOP, while the longitude provides information about the orientation of the ellipse.

In this three-dimensional space, the distance from the origin to a point (s_1, s_2, s_3) is, from Eq. (5), equal to the DOP. Thus, the radius of a partially polarized lightwave will be < 1 . In the experimental results described in this paper, the DOP of the measured light may fluctuate in time from much less than one to very nearly one; even so, it is still convenient to use the Poincaré sphere representation to visualize the SOP. To do so, the Stokes parameters of only the completely polarized component of the partially polarized lightwave are plotted on the Poincaré sphere as before. Equivalently (as in Figs. 2–6), the normalized points $(s_1/\text{DOP}, s_2/\text{DOP}, s_3/\text{DOP})$ are plotted instead of (s_1, s_2, s_3) so that all points, regardless of DOP, will lie on the unit sphere.

3. Experiments

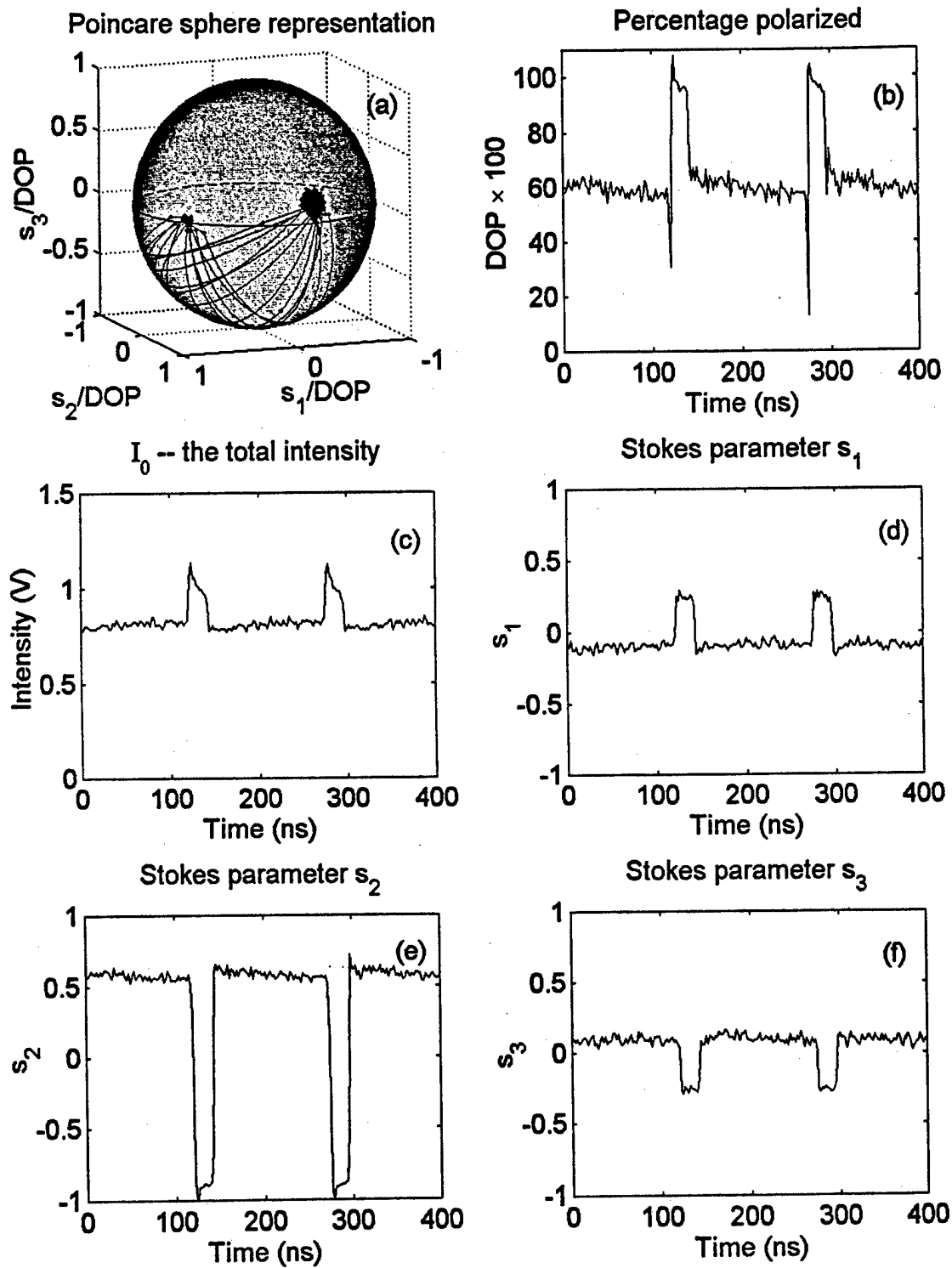
Light to be analyzed propagates from its source to the polarization analyzer in standard single-mode optical fiber. As shown in Fig. 1, a graded-index (GRIN) lens in the calibration area is used to couple the light from the fiber and into a collimated free-space beam. A polarizer or $\lambda/4$ plate is used in this free-space area during calibration, but during SOP measurement, this area is empty. A second GRIN lens is used to couple the collimated beam back into optical fiber. After passing through the calibration area, the light is split by optical couplers into four paths. Each of the four lightwaves passes through some free-space optical elements before they are measured by the photodiodes. Three of the paths include a polarization controller (PC), polarizer (Pol.), and variable attenuator (VAT) to prevent saturation of the photodiode, while the fourth includes just an attenuator. Through a calibration process, described in greater detail in Appendix A, the Stokes parameters of light in the calibration area can

be determined in a unique way from the intensities measured by the photodiodes (I_0, I_1, I_2 and I_3).

The light source for the experiments that follow is an EDFRL, as shown in Fig. 1. This EDFRL consists of 17 m of erbium-doped fiber (the active medium) with its ends connected together by a length of ordinary single-mode fiber. A 90/10 coupler in the ring couples approximately 10% of the light out of the ring to be analyzed. Pump diodes with a 980 nm wavelength are used to create the population inversion. These pump diodes are operated at around 100 mW optical pump power, many times the pump power of the first lasing threshold. Two optical isolators, one on either side of the erbium-doped fiber, ensure unidirectional propagation of light in the ring. A mandrel-type fiber-optic polarization controller is used inside the ring to control the type of dynamics that are observed at the output. The total length of fiber in the ring is about 37 m.

Though all of the fiber in the EDFRL is single-mode fiber, two orthogonal polarizations can propagate simultaneously in an EDFRL. These polarizations can interact nonlinearly through third-order nonlinearities of the fiber medium, and both polarizations are nonlinearly coupled to the population inversion. EDFRLs are well-known to generate light having rapid (many GHz) and chaotic fluctuations in output intensity, and some investigators have reported observations of polarization dependent fluctuations on these fast time scales as well [4]. Additionally, a self-pulsing regime can be observed which is the result of at least partial mode-locking between the thousands of very closely spaced longitudinal modes present in the laser. Several laser instabilities which may contribute to the chaotic intensity dynamics as well as the self-pulsing behavior are described by van Tartwijk and Agrawal in Ref. [5]. Attempts to understand the origin of the self-pulsing behavior and its relation to the Risken–Nummedal–Graham–Haken instability are made in Refs. [6,7]. In the paper presented here, the polarization dynamics of

Fig. 4. Light from an EDFRL in a self-pulsing regime is analyzed. (c) Shows that the pulses rise out of a constant intensity background. (d–f) Show the manner in which the Stokes parameters ‘switch’ between two values in synchrony with the pulses. (a) Clearly shows that the light is switching between two approximately orthogonal polarization states. (b) Shows that the DOP of the light is also switching between two values. During the pulses, the light is almost completely polarized, whereas during the interval between the pulses, the light is much less polarized. The changing values of the DOP could not have been observed without a measurement of all of the Stokes parameters.



the chaotic intensity fluctuations and of the self-pulsing behavior are observed using the high-speed polarization analyzer.

Data illustrating the accuracy of the experimental method is shown in Fig. 2. To obtain this data, light from an EDFRL was passed through a polarizer oriented at 45° from the x -axis in the calibration area. The normalized Stokes parameters for such a situation are $\vec{s} = (1, 0, 1, 0)$. Any deviation from these parameters in the experiment is a measure of experimental error, such as those which may occur during the calibration process. For example, the polarizer in the calibration area may not be aligned at precisely the correct orientation. Additional errors in this experiment may result from the fact that the photodiodes in this experiment are not identical. Their amplifiers may respond differently to the same measured signal. Finally, small changes in temperature or fiber stress can lead to changes in the fiber birefringences. These changes result in a calibration drift that reduces the measurement accuracy over time. From Fig. 2, it is clear that the measurement errors are reasonably small, even when measuring a signal whose intensity fluctuates rapidly and chaotically, as shown in Fig. 2(c). It should be noted that the fluctuations in Fig. 2(c) are much larger than the noise present in the detection equipment and should actually be interpreted as chaotic intensity fluctuations. The SOP measured is very close to the predicted values, $s_2 \approx 1$ while $s_{1,3} \approx 0$. The degree of polarization (DOP), given in Fig. 2(b) is close to its maximum value of 100%, as one would expect for light that has passed through a polarizer.

Fig. 3 shows results of a similar experiment. In this example, the polarizer in the calibration area has been removed. Thus, the actual SOP for the chaotic light from the EDFRL is being displayed in Fig. 3. Fig. 3(b) shows that the DOP is much lower than for the case where the light passed through the polarizer (Fig. 2). This suggests that the light from the EDFRL is making large polarization fluctuations at rates that are faster than the 125 MHz bandwidth of the photo-

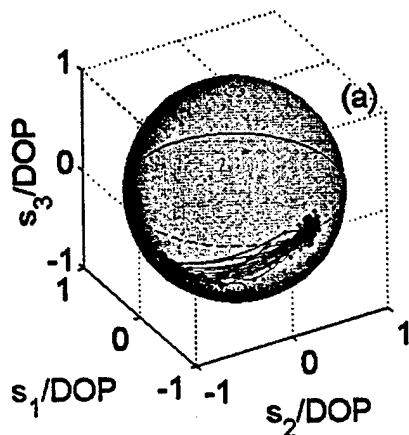
diodes. Fig. 3(a) clearly shows that the polarization output from the EDFRL changes rapidly with time, but is localized around a certain area on the Poincaré sphere. Fig. 3(d–f) show the fluctuations in the normalized Stokes parameters.

For certain settings of the polarization controller in the ring, the EDFRL used in this experiment also possesses a mode of operation in which self-pulsing of the intensity is observed. The SOP measurement technique described in this paper is able to discern features of this self-pulsing behavior that could not otherwise be observed. Fig. 4 shows data from an experiment in which the EDFRL was self-pulsing. The total intensity time series is shown in Fig. 4(c) showing self-pulsing with a repetition rate equal to one round trip in the ring laser. As can be seen in Fig. 4(a), the measured SOP of the light alternates between two areas on the Poincaré sphere. The two areas are located on opposite sides of the Poincaré sphere, indicating that they represent roughly orthogonal SOPs. From Fig. 4(d–f), it is clear that one of these areas corresponds to the SOP of light during a pulse, while the other area corresponds to the SOP of light between the pulses. Fig. 4(b) shows that the light during the pulses has a higher degree of polarization than the light measured during the interval between pulses. Such information could not have been obtained by simply observing the intensity of two orthogonal polarizations of light, as is often done by using a polarizing beam-splitter. The information about the DOP could lead to a new insight about the dynamics that give rise to such self-pulsing in ring lasers.

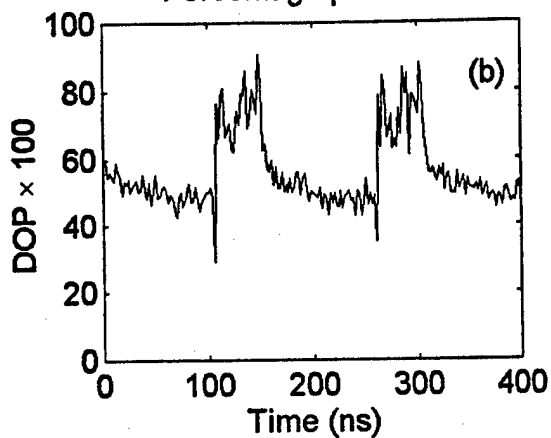
Fig. 5 shows another measurement of light from the EDFRL. The total intensity of the light from the EDFRL, shown in Fig. 5(c), displays an irregular self-pulsing. In Fig. 4, the SOP of the light seemed to be localized around two areas. In Fig. 5(a), the SOP is also evolving between two localized areas, but unlike the data shown in Fig. 4, these areas are not orthogonal to one another. Consequently, the polarization dynamics shown in Fig. 5 could not

Fig. 5. Light produced by an EDFRL is analyzed. (f) Shows the time-evolution of s_3 which is clearly different from the evolution of $s_{1,2}$ shown in (d,e). Again, the DOP shown in (b) seems to increase during the pulses and be lower during the interval between them, though the difference is not so pronounced as in Fig. 4(b). The SOP shown in (a) seems to be evolving between two non-orthogonal states—such an observation could not be made by examining the orthogonal polarizations output from a simple polarizing beam-splitter.

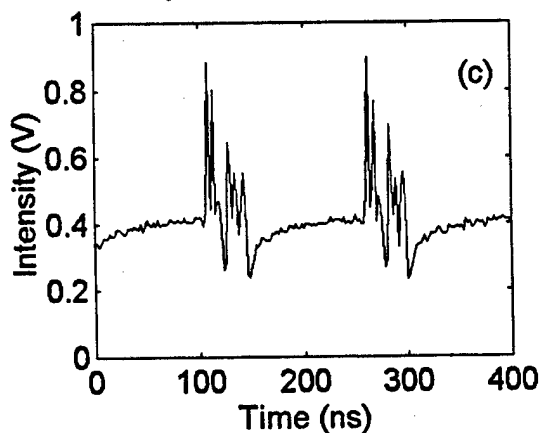
Poincare sphere representation



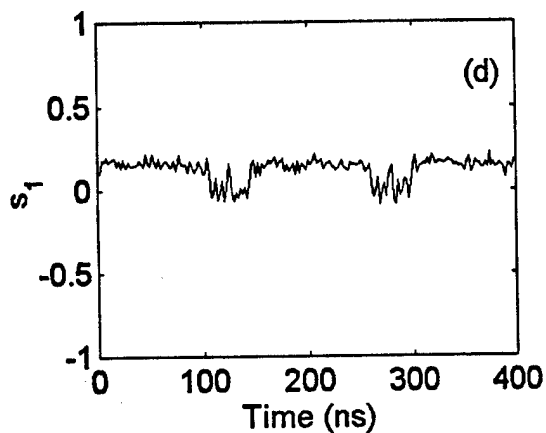
Percentage polarized



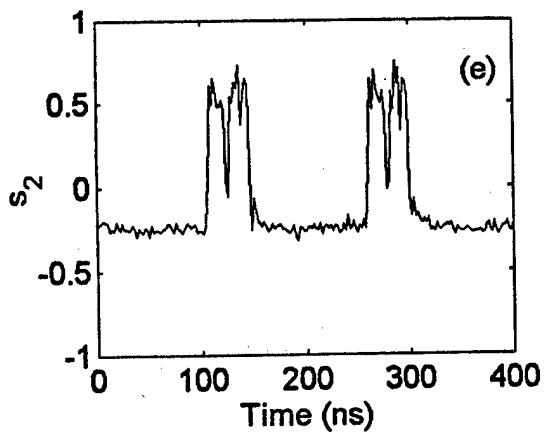
I_0 -- the total intensity



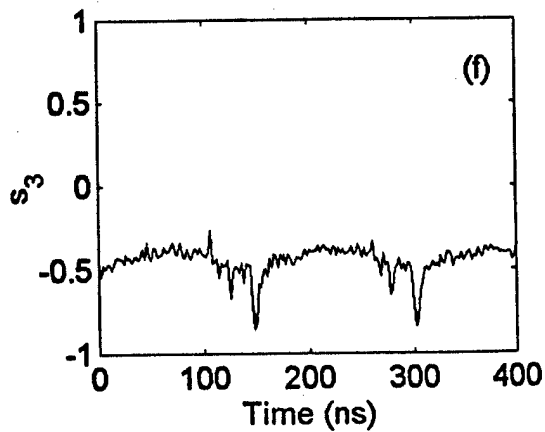
Stokes parameter s_1

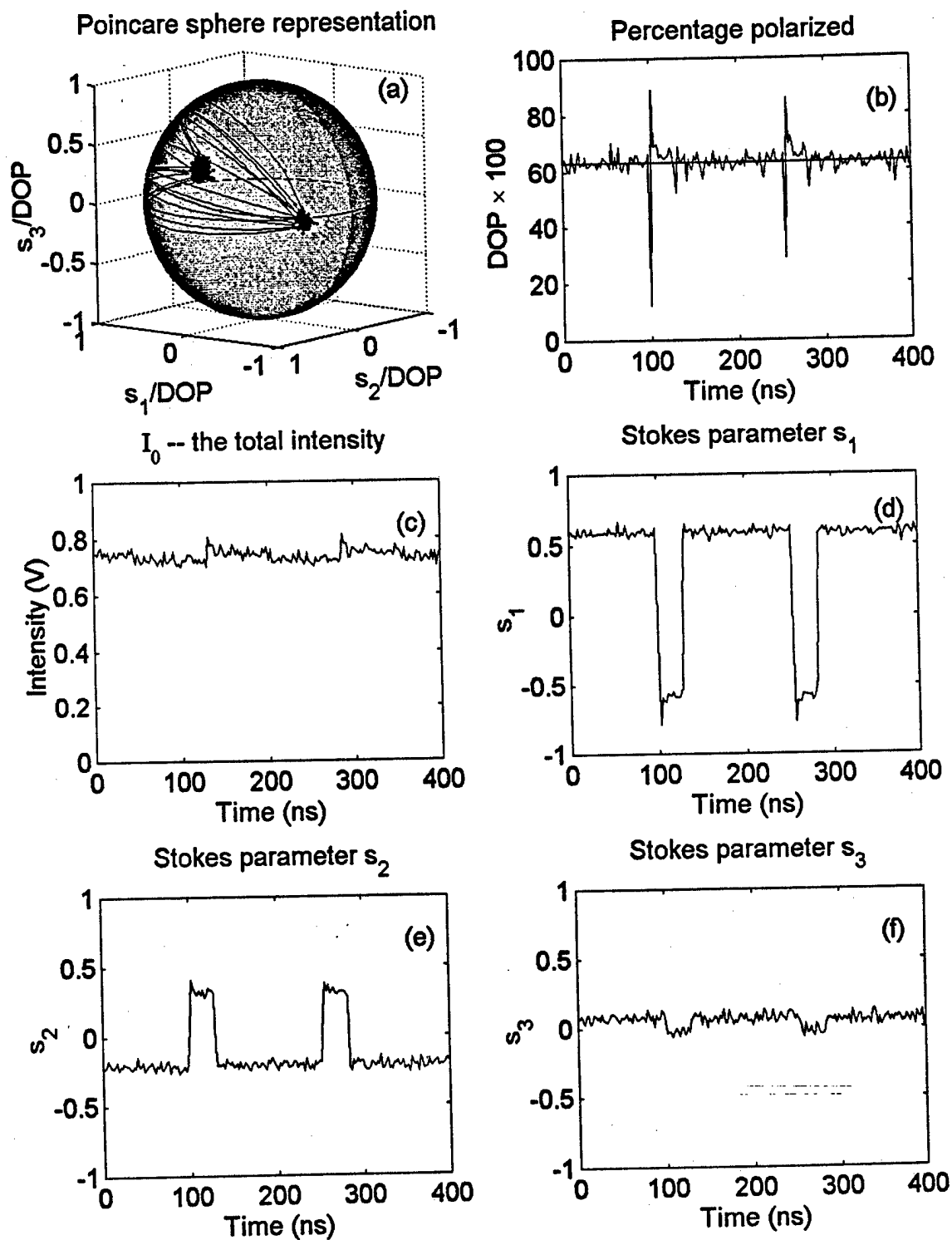


Stokes parameter s_2



Stokes parameter s_3





have been obtained using a polarizing beam-splitter to analyze two orthogonal polarization of the light from the EDFRL. Interestingly, each time series in Fig. 5(d–f) displays behavior that is different than from the others.

Fig. 6 shows a case in which the total intensity of the light, shown in Fig. 6(c), has relatively small intensity fluctuations, but the polarization state of the light is switching rapidly between approximately orthogonal polarization states. In such a case, a simple intensity measurement provides little insight into the laser dynamics; much more insight can be obtained by analyzing the polarization dynamics.

4. Conclusion

A high-speed polarization analyzer was developed to measure rapidly fluctuating polarization states of lightwaves. The high-speed of the measurements was required in order to more accurately measure the full polarization dynamics of lightwaves whose polarization states fluctuate on fast (several nanoseconds) time-scales. The technique was enabled by a four-channel digital sampling oscilloscope recording the intensity information from four photodiodes (125 MHz, 3-dB bandwidth) simultaneously at 500 MS/s for each channel. In some ways, the use of fiber optics simplified the usage of the apparatus. Beam alignment and beam shaping difficulties were eliminated. On the other hand, the birefringence of the optical fibers and its sensitivity to perturbations meant that the system must be calibrated (as described in Appendix A) before each set of experiments.

As indicated by the experiments performed using an EDFRL source, a measurement of the full polarization dynamics can often reveal important and otherwise hidden insight into an optical system. Fig. 3 showed that the polarization of the light from the EDFRL evolved rapidly in time. Fig. 4 showed that the DOP of the self-pulsing light was higher during the pulses than during the interval between the pulses, a phenomenon that had not been observed before.

The non-orthogonal switching of the SOP shown in Fig. 5 could not have been observed by measuring two orthogonal polarizations, as is often done with polarizing beam splitters. Fig. 6, with its relatively constant intensity, is an example of a situation in which high-speed measurements of the SOP can provide much more insight into the dynamics of the system than a simple intensity measurement.

Acknowledgements

We thank Henry Abarbanel, Matt Kennel, Steve Strogatz, N.G. Johnson and all others (at UCSD, Cornell, and Georgia Tech) involved in our collaboration, through National Science Foundation grant NCR961225, for helpful discussions. We gratefully acknowledge support from the Office of Naval Research, and thank C. Verber, P. Juodawlkis, M. Gross, and P. O'Shea for providing essential instrumentation and encouragement.

Appendix A. Calibration and measurement of the stokes parameters

As shown in Fig. 1, light that is to be analyzed propagates from its source to the polarization analyzer via single-mode optical fiber. Light is coupled out of the fiber by a GRIN lens and passes through the calibration area before being coupled back into the fiber by yet another GRIN lens. During the calibration procedure, a polarizer or $\lambda/4$ waveplate are used in the calibration area, but for an actual SOP measurement, this area is empty. After passing through the calibration area, the light is divided at the first coupler, and approximately 10% of the light is directed toward the photodiode that measures the intensity, I_0 . The remaining 90% of the light continues propagating to the 1×3 coupler where it is split into thirds. The light in all of these branches is again coupled out of the fiber to be operated on by the free-space optical elements shown in the figure—a

Fig. 6. Light produced by an EDFRL is shown to have roughly orthogonal polarization switching (a), while at the same time, the intensity of the light (c) gives little indication of the large SOP switching. The DOP in (b) does not exhibit the same large changes as in Figs. 4 and 5.

polarization controller, a polarizer, and a variable attenuator. As in the calibration area, a second GRIN lens couples the free-space light back into the fiber to guide it to a photodiode. An accurate measurement of the SOP of a lightwave requires that the lengths of fiber in each path be properly matched. Experimentally, the precision with which the lengths are matched is ± 2 cm.

VATs are used in the experiment to prevent saturation of the photodiodes. The attenuation is accomplished by placing an anti-reflection coated glass plate between the two GRIN lenses. Refraction in the glass plate for orientations other than perpendicular to the beam results in a lateral translation of the beam. The lateral translation affects the coupling efficiency of the light back into the fiber (through the GRIN lens). Thus, the variable attenuation is controlled by adjusting the orientation of the glass plate.

In addition to this attenuation, the free-space beams propagating toward the photodiodes measuring I_1 , I_2 and I_3 must also pass through a polarization controller and a polarizer. The polarization controller consists of three waveplates, $\lambda/4$, $\lambda/2$ and $\lambda/4$, respectively. With proper adjustment of their orientations, these three waveplates are able to transform light of any SOP to any other SOP that is desired. Immediately after the waveplates, the light passes through a polarizer. The photodiode that follows it is only able to measure the component of the light that passes through the polarizer.

Finally, the detection equipment consists of the four photodiodes and the DSO. The photodiodes used in this experiment have a 3-dB bandwidth of 125 MHz, but higher frequencies can be observed. These photodiodes are the components that limit the speed at which polarization fluctuations can be observed in this experiment. The intensity measured by a photodiode is recorded at a rate of 500 MS/s by one of the four channels of a digital sampling oscilloscope.

In order to find the SOP of a lightwave using this polarization analyzer, a relationship between the four intensities, I_0 , I_1 , I_2 and I_3 , and the four Stokes parameters must be determined. An example of how such a relationship can be obtained is provided in Ref. [1] for a free-space, rather than fiber-optic, system. In the example given in Ref. [1], the follow-

ing equation relates the intensities to Stokes parameters:

$$\begin{pmatrix} S_0 \\ S_1 \\ S_2 \\ S_3 \end{pmatrix} = \begin{bmatrix} 1 & 0 & 0 & 0 \\ -1 & 2 & 0 & 0 \\ -1 & 0 & 2 & 0 \\ -1 & 0 & 0 & 2 \end{bmatrix} \begin{pmatrix} I_0 \\ I_1 \\ I_2 \\ I_3 \end{pmatrix}. \quad (6)$$

Optical fiber, as used in the experiment presented here, possesses random birefringences that causes the polarization of a lightwave to evolve in an unpredictable manner as it propagates. Consequently, the transfer matrix that relates the Stokes parameters to the measured intensities cannot be known prior to calibration. Though the matrix is unknown before calibration, there must exist some transfer matrix for relating the measured values of I_0 , I_1 , I_2 , and I_3 to the Stokes parameters.

The elements of the appropriate transfer matrix can be obtained through a calibration procedure. By placing appropriate optical elements in the calibration area, the Stokes parameters of the light as it is coupled back into the fiber can be completely defined. Measuring the values I_0 , I_1 , I_2 , and I_3 when the SOP is defined enables a determination of the elements of an inverse transfer matrix. The new calibration equation takes the form (using the normalized Stokes parameters),

$$\begin{pmatrix} a_1 & b_1 & c_1 & d_1 \\ a_2 & b_2 & c_2 & d_2 \\ a_3 & b_3 & c_3 & d_3 \\ a_4 & b_4 & c_4 & d_4 \end{pmatrix} \begin{pmatrix} s_0 \\ s_1 \\ s_2 \\ s_3 \end{pmatrix} = \begin{pmatrix} I_0 \\ I_1 \\ I_2 \\ I_3 \end{pmatrix}. \quad (7)$$

where the normalized Stokes vectors have been used.

Sending continuous-wave (CW) unpolarized light, $\vec{s} = (1, 0, 0, 0)$, into the apparatus reduces Eq. (7) to the following equations, which allow the determination of the a elements:

$$\begin{aligned} a_1 &= I_0 \\ a_2 &= I_1 \\ a_3 &= I_2 \\ a_4 &= I_3. \end{aligned} \quad (8)$$

However, no source of completely unpolarized light was conveniently available during the experiments described in this paper. An alternative method

was used to obtain the values of the a elements. Light from the tunable diode laser having the same wavelength as light from the EDFRL is passed through a polarizer in the calibration area and then coupled back into the fiber. The polarization controllers in the paths leading to the photodiodes that measure I_1 , I_2 , and I_3 are oriented to ensure maximum transmission through the polarizers. Values for I_1 , I_2 , and I_3 are measured, as is a value for I_0 . If this light had been completely unpolarized, only half of the measured intensity would have been transmitted through the polarizers in front of I_1 , I_2 , and I_3 , so the a 's are determined by

$$\begin{aligned} a_1 &= I_0, \\ a_2 &= I_1/2, \\ a_3 &= I_2/2, \\ a_4 &= I_3/2. \end{aligned} \quad (9)$$

The next step in the calibration process is to create linearly polarized light along the x -axis in the calibration area and couple it back into the fiber. To do so, a polarizer with an extinction ratio > 45 dB is used. It is placed in an optical mount capable of 0.5° precision. The Stokes vector for such a light source linearly polarized along the x -axis is $\vec{s} = (1, 1, 0, 0)$. Multiplying this by the matrix above allows the determination of the b elements in the following way:

$$\begin{aligned} b_1 &= I_0 - a_1, \\ b_2 &= I_1 - a_2, \\ b_3 &= I_2 - a_3, \\ b_4 &= I_3 - a_4. \end{aligned} \quad (10)$$

Since the a values have already been determined, the determination of the b 's is straightforward. Subsequently, linearly polarized light at 45° , $\vec{s} = (1, 0, 1, 0)$, is sent to the photodiodes to determine the values of the c elements. Determining the d values requires circularly polarized light, $\vec{s} = (1, 0, 0, 1)$ —a somewhat more difficult task to create.

The most direct method in this experiment to create circularly polarized light is to pass linearly polarized light at an orientation that is half-way between the fast and slow axes of a quarter-wave-plate. While the laboratory possessed a quarter-

wave-plate, the orientation of its principal axes had to be empirically determined. First, the polarization controller immediately after the TDL and a polarizer in the calibration area are jointly aligned for maximum extinction of the light from the TDL-light from the TDL is completely polarized, i.e., DOP = 100%. Maximum extinction implies that the light coupled from the fiber and into free space in the calibration area is linearly polarized orthogonal to the polarizer. After maximum extinction is obtained, a quarter-wave plate is placed in front of the polarizer in the calibration area. With this configuration, total extinction will occur if one of the optic axes of the quarter-wave plate is aligned with the polarizer. Maximum transmission (in this configuration) occurs when the axes are oriented at 45° relative to the linearly polarized light incident on the quarter-wave-plate. With this orientation of the axes, circularly polarized light is output from the quarter-wave plate. After the polarizer is removed, circularly polarized light passes to the GRIN lens where it is coupled back into the fiber. Thus, light represented by the Stokes parameters $\vec{s} = (1, 0, 0, 1)$ is generated, thereby permitting the determination of the d elements of the matrix.

With the elements of the matrix now determined, it is possible to determine the Stokes parameters of the lightwave in the calibration area from any set of intensity values, I_0 , I_1 , I_2 , and I_3 . All that is required is to invert the matrix in Eq. (7) and multiply by the intensity vector. To minimize the effect of experimental errors, it is important that the matrix to be inverted not be ill-conditioned. The polarization controllers in front of the photodiodes measuring I_1 , I_2 , and I_3 were therefore adjusted prior to calibration so that the matrix elements obtained are roughly similar to those obtained by inverting the matrix in Eq. (6), but scaled by a factor of S_0 due to the use of the normalized Stokes parameters.

After these procedures have been followed, the optical elements are removed from calibration area. A light source to be analyzed is connected to the apparatus, and the oscilloscope records the values of I_0 , I_1 , I_2 , and I_3 as they fluctuate in time. These vectors are then multiplied by the transfer matrix obtained with the procedure given above to find the Stokes parameters of the light source as a function of time.

References

- [1] E. Hecht, *Optics*, Addison-Wesley, Reading, MA, 1990, p. 322.
- [2] M. Born, E. Wolf, *Principles of Optics*, Pergamon, Oxford, 1975, p. 554.
- [3] R.M.A. Azzam, N.M. Bashara, *Ellipsometry and Polarized Light*, Elsevier, Amsterdam, 1989, pp. 52–60.
- [4] Q.L. Williams, J. Garcia-Ojalvo, R. Roy, *Phys. Rev. A* 55 (1997) 2376.
- [5] G.H.M. van Tartwijk, G.P. Agrawal, *Progr. Quantum Electronics* 22 (1998) 43.
- [6] F. Fontana, M. Begotti, E.M. Pessina, L.A. Lugiato, *Optics Commun.* 114 (1995) 89.
- [7] E.M. Pessina, G. Bonfrate, F. Fontana, L.A. Lugiato, *Phys. Rev. A* 56 (1997) 4086.